3D Printed Neuromorphic Sensing Systems

by

Chao Bao

M.Sc., Harbin Institute of Technology, 2008
B.Eng., Harbin Institute of Technology, 2006

Thesis Submitted in Partial Fulfillment of the
Requirements for the Degree of
Doctor of Philosophy

in the
School of Mechatronic Systems Engineering
Faculty of Applied Sciences

SIMON FRASER UNIVERSITY
Fall 2021

Declaration of Committee

Name:	**Chao Bao**
Degree:	**Doctor of Philosophy**
Title:	**3D printed Neuromorphic Sensing Systems**
Committee:	**Chair: Mohammad Narimani** Lecturer, Mechatronic Systems Engineering
	Woo Soo Kim Supervisor Associate Professor, Mechatronic Systems Engineering
	Byron Gates Committee member Professor, Chemistry
	Carlo Menon Committee member Adjunct Professor, Mechatronic Systems Engineering
	Manpreet Kaur Examiner Lecturer, Sustainable Energy Engineering
	Xihua Wang External Examiner Associate Professor, Electrical and Computer Engineering University of Alberta

Abstract

Thanks to the high energy efficiency, neuromorphic devices are spotlighted recently by mimicking the calculation principle of the human brain through the parallel computation and the memory function. Various bio-inspired 'in-memory computing' (IMC) devices were developed during the past decades, such as synaptic transistors for artificial synapses. By integrating with specific sensors, neuromorphic sensing systems are achievable with the bio-inspired signal perception function. A signal perception process is possible by a combination of stimuli sensing, signal conversion/transmission, and signal processing. However, most neuromorphic sensing systems were demonstrated without signal conversion/transmission functions. Therefore, those cannot fully mimic the function provides by the sensory neuron in the biological system.

This thesis aims to design a neuromorphic sensing system with a complete function as biological sensory neurons. To reach such a target, 3D printed sensors, electrical oscillators, and synaptic transistors were developed as functions of artificial receptors, artificial neurons, and artificial synapses, respectively. Moreover, since the 3D printing technology has demonstrated a facile process due to fast prototyping, the proposed 3D neuromorphic sensing system was designed as a 3D integrated structure and fabricated by 3D printing technologies. A novel multi-axis robot 3D printing system was also utilized to increase the fabrication efficiency with the capability of printing on vertical and tilted surfaces seamlessly. Furthermore, the developed 3D neuromorphic system was easily adapted to the application of tactile sensing. A portable neuromorphic system was integrated with a tactile sensing system for the intelligent tactile sensing application of the humanoid robot. Finally, the bio-inspired reflex arc for the unconscious response was also demonstrated by training the neuromorphic tactile sensing system.

Keywords: neuromorphic; 3D printing; electrochemical sensing; tactile sensing; synaptic transistor

Dedication

Dedicated to my lovely wife, Jingxi Luo

and my parents, parents-in-law

for your support and encouragement

Acknowledgements

I would like to express my sincere gratitude to my senior supervisor, Dr. Woo Soo Kim, who has given me this opportunity to work with him and provided me with continuous support and valuable guidance during my PhD study. His insightful comments and suggestions helped me keep on the right way of researching.

I would like to acknowledge my thesis committee, Dr. Byron Gates and Dr. Carlo Menon, for accepting to be on my advisory committee, giving me constructive advice, and spending time reviewing my work. I would also like to thank the examining committee, Dr. Manpreet Kaur and Dr. Xihua Wang as well as the chair of the session, Dr. Mohammad Narimani, for accepting to be a part of my thesis defense. I would like to thank the staff and students of Mechatronic Systems Engineering of Simon Fraser University for being friendly and supportive. I would also acknowledge the use of shared facilities at Powertech and Simon Fraser University (SFU).

I am deeply grateful to my lab mates at Additive Manufacturing Lab (AML) for spending memorable time together. In particular, my colleagues like Xin Min, Taeil Kim, Manpreet Kaur, Seong Hyeon Park, Tae-Ho Kim, Daina Baker, Amirhossein Hassanpoor Kalhori, Wonchul Lee, Haotian Su, and Hadi Moeinnia, thanks for your assistance, idea, and accompany. I would also thank all co-op students.

Additionally, I am immensely grateful to my wife, parents, parent-in-law, and sister for their support, patience, and encouragement over the years. I am grateful to the friends here for providing me with their support and sharing wonderful times. I would also say thanks to the many unknown people who provided help to me during the past four years.

Table of Contents

List of Figures

List of Acronyms

2-NPOE	2-nitrophenyl octyl ether
2T	Two-terminals
3T	Three terminals
AC	Alternating current
AgCl	Silver chloride
Ca^{2+}	Calcium ions
CMOS	Complementary metal-oxide-semiconductor
CNS	Central nervous system
DC	Direct current
DIW	Direct ink writing
DMF	N, N-dimethylformamide
DOS	Dioctyl sebacate
EDL	Electrical double layer
EMF	Electromotive force
FETs	Field effect transistors
FFF	Fused filament fabrication
FSR	Force-sensitive resistor
FTJs	Ferroelectric tunnel junctions
GPU	Graphics processing unit
H_3O^+	Hydronium
HfZrOx	Zirconium-doped hafnium oxide
HRS	High-resistance
IDEs	Interdigitated electrodes
IGZO	Indium gallium zinc oxide
IMC	In-memory computing
IR	Infrared
ISEs	Ion-selective electrodes
ISFETs	Ion-selective field effect transistors
K^+	Potassium
KCl	Potassium chloride
KTpClPB	Potassium tetrakis (4-chlorophenyl) borate

LC	Inductive/capacitive
$LiClO_4$	Lithium perchloride
LOD	Limit of detection
LRS	Resistance state
MFM	Metal-ferroelectric-metal capacitor
NaTFPB	Sodium tetrakis [3,5-bis (trifluoromethyl) phenyl]borate salt
NeuTap	Neuromorphic tactile processing system
NH_4^+	Ammonium
NPK	Nitrogen/phosphorous/potassium
OCP	Open circuit potential
OECT	Organic electrochemical transistors
OH^-	Hydroxide
P3HT	Poly (3-hexylthiophene)
PEN	Polyethylene naphthalate
PEO	Poly (ethylene oxide)
PI	Polyimide
PNS	Peripheral nervous system
PPF	Paired-pulse facilitation
PVC	Poly (vinyl chloride)
RC	Resistor/capacitor
RE	Reference electrode
SFG	Self-formed floating-gate
SLA	Stereolithography
SLS	Selective laser sintering
THF	Tetrahydrofuran
TiN	Electrode titanium nitride
TPU	Tensor processing unit
UV	Ultraviolet
WE	Working electrode
ZTO	Zinc tin oxide

Glossary

α, β	Angle of 3D origami
ε_r	Relative static permittivity
η	Ratio of l/r
μ	Permeability
A	Overlap area of the two plates
C_E	Outer capacitance
C_I	Internal electrode
d	Separation between the plate
$D_{in(max)}$	Maximum strain deviation
E	Electromotive force
F	Faraday constant
$IN_{f.s.}$	Strain at full scale
K	Selectivity coefficient
l	Length
N_C	Number of IDEs
N_L	Number of turns
r	Radius
R	Gas constant
ΔR_{max}	Resistance difference between the original and compressed state of 3D origami
S	Sensitivity slop
ΔS_{max}	Maximum compressed length of the origami
T	Absolute temperature
Z	Charges numbers

Chapter 1.

Introduction

1.1. Background and motivation

Human body makes decisions based on different environmental stimuli, such as temperature, pressure, light, sound, taste, smell, etc. This process refers to a complicated information processing procedure, including detection, signal conversion/ transmission, signal processing, and motion controlling. The detected information is transmitted to the brain and processed, followed by a decision made by the brain to control the human body, as shown in Figure 1.1. The whole process is accomplished by nerve systems, including the peripheral nervous system (PNS) and the central nervous system (CNS). Although complicated conditions refer to spatial and temporal information, the biological system responds with ultra-low energy and fast speed (10^{16} complex operations per second while only costs few watts).[1] The reason is due to the unique parallel processing and memory by the synapses distributed inside the brain. It is reported that there are around 10^{11} neurons, each neuron with more than 1000 synapses in the brain.[2,3] As shown in Figure 1.2, synapses are typically used to connect different neurons, including the neurons inside of PNS and CNS.[4] Therefore, researchers are trying to replicate such a high efficient function through neuromorphic systems. Few steps have been experienced during the past decades.

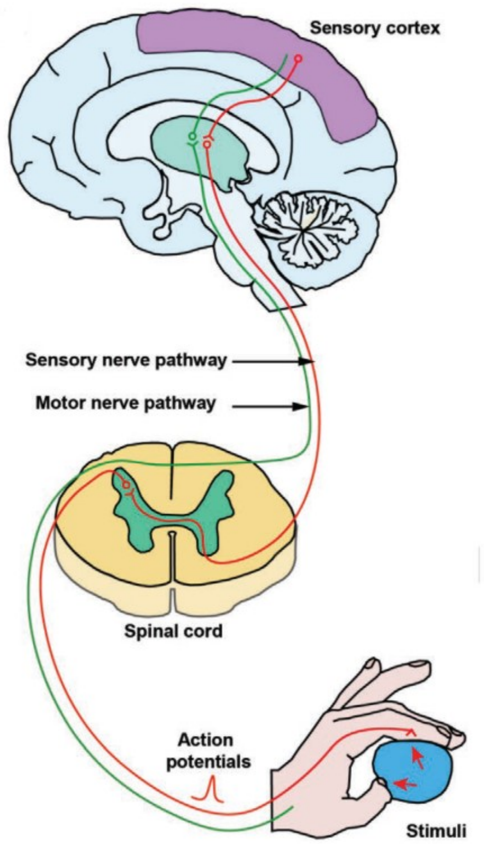

Figure 1.1. The pathway of stimulus-response in biological systems. Reprinted with permission[5]

Figure 1.2. Neurons are connected by synapses. Reprinted with permission[4]

Firstly, researchers tried to mimic the parallel calculation by novel algorithms as simulation neuromorphic systems.[6] For example, machine learning (ML) technology has already been widely studied and utilized by developing various neuro-networks during the past decades. Although software/neural network development has already achieved enormous progress, it still faces the limitation of relatively enormous energy consumption.

The reason is that the processors carrying out these algorithms are still based on the conventional von Neumann paradigm, where operation and memory are separated physically. This separation results in significant energy consumption for data exchanging between these two units. For example, for a 32-bit DRAM with 45 nm complementary metal-oxide-semiconductor (CMOS) technology, 0.9pJ energy is used for an add operation while 640 pJ for memory accessing due to traditional von Neumann architecture and digital framework.[7] It has also been found that continuously accessing data takes the majority part of the whole energy consumption. Furthermore, the physical separation also restraints the increment of calculation speed due to extra time speeding on data switching.

Then, to increase energy efficiency and calculation speed, various novel technologies have been innovated and optimized to reduce the size of the single CMOS device. As a result, energy consumption and data exchange speed have significantly improved during the past decades, which nearly satisfies Moore's law.[8] However, the situation became more difficult because the transistor channel's size almost reached the physical limit with cutting-edge technologies, increasing the current leak risk.[9] Therefore, CMOS-based bio-inspired neuromorphic systems have been designed to carry out parallel calculations, such as graphics processing unit (GPU), central processing unit, and tensor processing unit (TPU).[10] Since all these state-of-the-art hardware are still based on CMOS transistors, they still face the drawbacks of conventional von Neumann architecture.

Finally, bio-inspired neuromorphic systems with novel architecture that realize bio-inspired 'in-memory computing' (IMC) devices are urgent to emerge, such as artificial synapses.[9,10] The IMC is accomplished by the non-volatile effect of artificial synapses for parallel calculation and memory/learning. Therefore, artificial synapses constructed neuromorphic systems execute computation and memory in the same area.[11] Thus, several advantages are accomplished due to the IMCS. Firstly, neuromorphic systems have high energy efficiency since the individual energy consumption for artificial synapses has already reduced to the level of femtojoule, which is identical to that of a real synapse.[12] Secondly, artificial synapse-formed neuromorphic systems significantly reduce the number of components for replicating biological functions. For instance, one memristor-based artificial synapse-formed nociceptor accomplished six CMOS-based formed nociceptors.[4] Thirdly, the parallel paradigm save the energy and time for data transmission between these two units in conventional von Neumann architecture.[10] Finally, additional energy is saved by unnecessary signal conversations between analog and digital information due to neuromorphic systems' intrinsically analogical computing feature.[9,10] Neuromorphic systems were also utilized to detect environmental stimuli by integrating with a sensory function as neuromorphic sensing systems. Bio-inspired artificial sensory neurons were utilized to detect pressure and light by integrating tactile sensors and light sensors, respectively.[13–15]

Therefore, the motivation of this study is to understand the mechanism of neuromorphic sensing systems and to construct a novel neuromorphic sensing system that is adapted to different sensing functions. For this objective, the key components for a neuromorphic sensing system were studied through experiments, including artificial receptors, artificial neurons, and artificial synapses for signal detection, transmission, and processing, respectively. Furthermore, another motivation is to realize the unconscious response function by the neuromorphic sensing system.

Regarding fabrication of neuromorphic devices, the most advanced nanomanufacturing technology can easily create neuromorphic devices, such as lithography,[12] sputtering,[16] spin coating,[17] RF magnetron sputtering,[4] electron beam evaporation,[18] photolithography,[19] to name a few. However, these mentioned technologies usually involve ultra-high precise instruments. Furthermore, the planar structure is a common characteristic of the neuromorphic devices fabricated by those high technics, hinting at the **diversity** of designs. Thus, thanks to the fast and facile fabrication, 3D printing technology has been applied in many research and industry fields. Therefore, various 3D printing approaches are carried out in this study. Moreover, a novel 3D printing system is also constructed to expand the application of 3D printing technology.

1.2. Objective and Scope of Thesis

The overall objective of this thesis is to study and demonstrate a bio-inspired neuromorphic sensing system by facile 3D printing methods. A complete perception function as biological sensory neurons needs to be realized by the demonstrated system, including sensing, signal transmission, and signal processing. To accomplish this, an essential understanding of signal processing procedures in neuromorphic sensing systems is required. Therefore, the **first objective** is to study and demonstrate artificial receptors for capturing environmental stimuli, especially electro-chemical sensing for ion concentration detection. The **second objective** is to design and fabricate a neuromorphic sensing system as a sensory neuron containing the signal conversion/transmission and processing functions. The mechanism of signal conversion/transmission and processing also needs to be confirmed by experiments. The **third objective** is to optimize the 3D printing method, especially the paste-based conductive direct ink writing (DIW). The **final objective** is to adapt the demonstrated neuromorphic sensing system to tactile sensing. A 3D printed humanoid robot hand integrated with the neuromorphic sensing system demonstrates an unconscious response.

The scope of this study is to demonstrate a 3D printed neuromorphic sensing system with entire biological functions that is utilized for controlling humanoid hands in the artificially intelligent robot field.

1. The 3D printed ISEs are prepared as **artificial receptors** and integrated with field effect transistors (TFTs) as hybrid ion-selective field effect transistors (ISFETs). Solutions with a series of different ion concentrations are prepared to study the sensitivity and selectivity of ISFETs.

2. For signal transmission, Inductor-capacitor (LC) oscillators are designed and studied as **artificial neurons** to obtain spike signals for biological learning and memory functions. LC oscillators are tuned by the simulated method to figure out the values for individual components. Electrical simulation is carried out for the design of electric components with desired values. The structure of LC oscillators is also compared to obtain an optimal design.

3. The 3D printed inorganic zinc tin oxide (ZTO)-based synaptic transistors are utilized as **artificial synapses**. The fabricated synaptic transistors are characterized to explain the mechanism of the non-volatile effect.

4. Electrochemical sensors, oscillators, and synaptic transistors are integrated to form a neuromorphic electrochemical sensing system. Signals transmitted inside of each component are studied to confirm the integration of the **neuromorphic electrochemical sensing system**. The performance of the neuromorphic electrochemical sensing system is studied and explored to detect ion concentrations in artificial soil.

5. A **multi-axis robot** arm integrated with a conventional DIW printer is explored to increase fabrication efficiency with in-situ laser sintering system.

6. The **portable neuromorphic system** is proposed to help the replacement and integration with humanoid hands. An origami tactile sensor is designed and 3D printed. The origami tactile sensor is integrated with the neuromorphic system to provide a touching sensing function for the humanoid hand.

7. With the **neuromorphic tactile sensing system**, the humanoid hand is trained to show the bio-inspired unconscious response as the bio-reflex arc. However, the precise control of the gripping force through training is not the scope of this study.

1.3. Thesis Organization

This thesis is organized as a series of six chapters, including four chapters of research works, plus one introduction chapter and one conclusion chapter. Chapter 3 and Chapter 4 are written based on the published papers, while chapter 5 is based on a submitted manuscript. Chapters 3, 4, and 5 begin with a summary of the study objectives and an explanation of the method involved. Chapters are organized as below:

Chapter 1 is dedicated to the background and motivation of this thesis, introduction of neuromorphic systems, and discussion of the necessary for 3D printed neuromorphic systems. The objective and scope of this thesis are also clarified.

Chapter 2 provides a comprehensive literature review on two major aspects of this thesis: (i) *neuromorphic sensing systems*, (ii) *3D printing approach*. A survey of (i) *two-terminals artificial synapse*, (ii) *three-terminal artificial synapse*, and (iii) *application of neuromorphic system* is discussed. A review of the 3D printing method classified based on materials is conducted, including (i) *filament-based fused filament fabrication (FFF)*, (ii) r*esin-based digital projection lithography (DLP) / stereolithography (SLA)*, (iii) *paste-based direct ink writing (DIW)*, and (iv) *powder-based selective laser sintering (SLS)*.

Chapter 3 is titled '3D Printed Electrochemical Sensor', equivalent to the published journal paper, *C. Bao, M. Kaur, and W. S. Kim. Toward a highly selective artificial saliva sensor using printed hybrid field effect transistors. Sensors and Actuators B: Chemical*

285 (2019)186-192, with minor modifications. This chapter presents 3D printed ion-selective electrodes (ISEs) for electrochemical detection. Two shapes of electrodes on field effect transistors (FETs) are designed to figure out an optimized structure. Then, the ISEs and FETs are integrated as hybrid ion-selective field effect transistors (ISFETs). Experiments are designed to investigate the sensitivity and selectivity of ISFETs. This chapter demonstrates the potential application of the ISFETs as an artificial tongue to detect concentration in artificial saliva.

Chapter 4 is titled '3D Neuromorphic Electrochemical Sensing System', equivalent to the published journal paper, *C. Bao, S. K. Seol, and W. S. Kim. A 3D integrated neuromorphic chemical sensing system. Sensors and Actuators B: Chemical 332 (2021) 129527*, with minor modifications. This chapter discusses the process of realizing a 3D-shaped neuromorphic electrochemical sensing system, which contains the full signal perception process as sensory neurons, including signal detection, transmission, and processing. Therefore, different functional components, including electrochemical sensor, 3D oscillator, and synaptic transistor, are designed in this chapter to achieve the bio-mimicked functions. Certification of signal perception process by the neuromorphic sensing systems is carried out through characterization step by step. Experiments are designed in this chapter to achieve the non-volatile performance for synaptic transistors. This chapter discusses the learning and memory of the neuromorphic electrochemical sensing system and the application of detecting low ion concentrations in artificial soil.

Chapter 5, titled as '3D Structural Neuromorphic Tactile Sensing System', discussed a neuromorphic system for tactile sensing. This work is written into a manuscript, *C. Bao, T. -H. Kim, A. H-Kalhori, and W. S. Kim. 3D Integrated Neuromorphic Humanoid Hand by Multi-axis Robot 3D Printing*, with minor modifications. The chapter presents a novel multi-axis robotic 3D printing approach with a laser assistant to fabricate 3D structural components. The neuromorphic system is designed as a portable device and integrated with a tactile sensor as a neuromorphic tactile sensing system. Chapter 5 also presents the unconscious performance of a 3D printed humanoid hand with the neuromorphic tactile sensing system after training, based on the learning and memory functions.

Finally, **Chapter 6** concludes the thesis by identifying this research work's achievements, contributions, and novelties. Furthermore, this chapter provides possible improvements and future work that can be explored further.

Chapter 2.

Literature Review

2.1. Neuromorphic Sensing System

2.1.1. Two-Terminals Artificial Synapse

The first scheme of 'in-memory computing' was proposed in the 1960s.[20] In this paradigm, computing and memory are accomplished in the same unit, which solves the energy and speed issue caused by the separation of computing and memory in traditional von Neumann architecture. Therefore, devices with such memory functions are desired to appear.

Although cutting-edge von Neumann architecture is a mature technology, neuromorphic systems with non-volatile memory and logic are the next generation of processors due to their high energy and space efficiency.[21] Memristor-formed artificial neurons and synapses are a promised candidate for constructing neuromorphic systems.[21] Memristors were firstly proposed by Leon Chua in 1971.[22] It has a sandwich structure that two electrodes surrounded an active layer in the middle. Since the resistive state of the active layer is preserved even after retrieving the bias on the top and bottom electrodes, memristors still exhibit non-volatile behaviors.[23] The non-volatile feature for memristors reflects on two reversible states: resistive and conductive.[21] In addition, the conductance of devices is maintained without voltage and modulated. Thanks to the non-volatile feature, memristors manifest high space efficiency, low power, and analog computing.[24] In addition, memristors are easily scaled up as crossbars by cutting-edge silicon fabrication technologies. Therefore, memristors formed crossbars have already been widely demonstrated in neuromorphic systems as neuromorphic multicore processors,[25] neuromorphic computing (pattern recognition),[26] and face classification.[27,28]

Diverse mechanisms for non-volatile effect have already been established to earn those functions, including phase-change, ferroelectric devices, valence change memory, electrochemical metallization cells, conductive filament formation, conductive filament formation, redox reaction, ferroelectric tunnel junction, to name a few.[10,24,29]

Phase Change

Phase changeable materials have two reversible states, high resistive amorphous state and high conductive crystalline state that was discovered in the 1950s.[30] As illustrated in Figure 2.1, these two states are controlled by applying different current pulses that produce Joule heat to induce phase switching. Unlike conventional devices that only have on and off states, phase change-induced memory was modulated continuously.[30] Moreover, by utilizing the non-volatile effect, phase change materials were widely applied as two-terminal memristors and neuromorphic computing.[31–33] Another application based on phase change is for memory.[30] A phase change material-based commercial non-volatile memory was also launched in 2018.

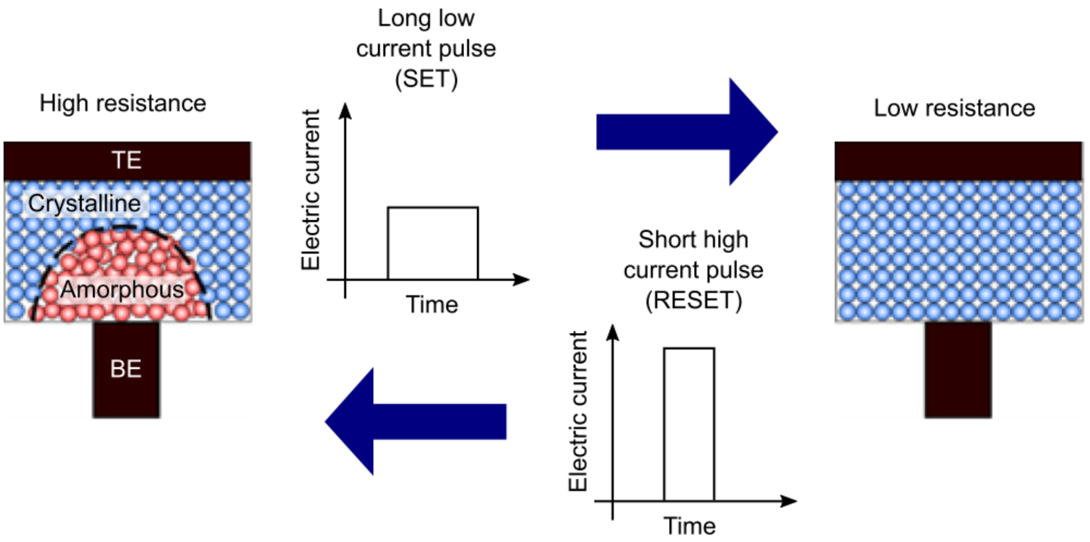

Figure 2.1. **Mechanism of switching states by phase change material. Reprinted with permission**[30]

Conductive Filament

For a sandwich structure device, non-volatile memory has also been obtained by forming conductive filament inside of the middle layer.[29] Metal oxides (such as SiOx: Ag[34]) are typically carried out as the intermedia layer, while active metal as two electrodes.[35] Due to the flexibility and low switching energy, organic material (such as chitosan) [36] and polymer materials (PMMA,[37,38] carboxymethyl κ-car,[39]) are deeply studied for two-terminal artificial synapses.[21,29] When a bias is applied to the electrodes, the active metal on the anode will be oxidated, followed by diffusing into the intermedial material under the electric force, as shown in Figure 2.2.[40] The conductive filament is formed when the oxidated metal ions reach the cathode and being reducted. Then, the device switches from a high-resistance (HRS) state to a low-resistance state (LRS). However, due to the limitation of the Ag^+ number, the formed filament is not strong enough to maintain after retrieving the applied bias that works as a volatile device. To achieve a non-volatile memory effect, Ag was doped inside carboxymethyl κ-car that a thicker filament was formed as compared in Figure 2.2. Based on the non-volatile performance, conductive firmament-based devices were also implemented as the next generation of memory and artificial nociceptors.[33,34,39]

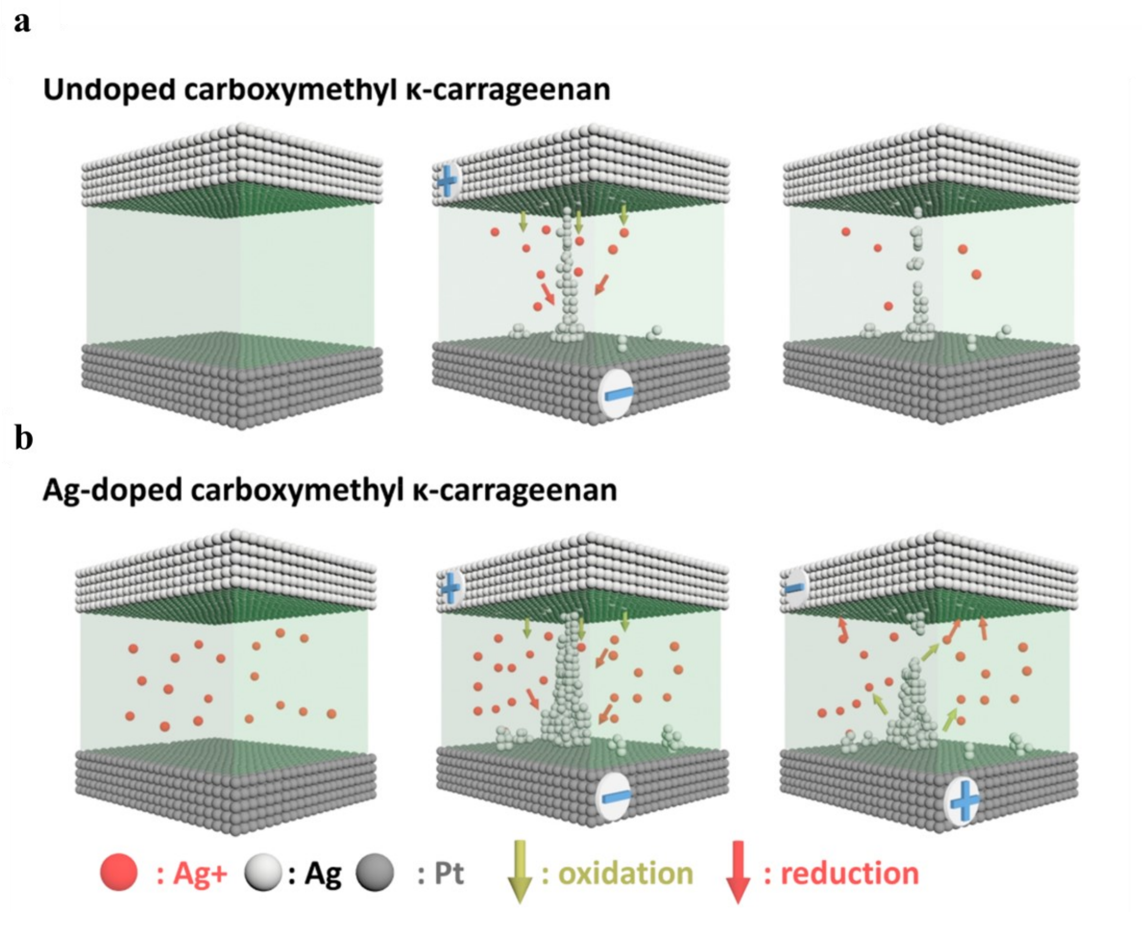

Figure 2.2. Mechanism of conductive filament formation-based resistance switching. (a) Undoped carboxymethyl κ-car. (b) Ag-doped carboxymethyl κ-car. Reprinted with permission[40]

Ferroelectric tunnel junction

The conductance of two-terminal artificial synapses is achieved by controlling the resistance of ferroelectric tunnel junctions (FTJs). FTJs are constructed by ferroelectric materials that are with asymmetric structures. Thus, by applying an electric field, the ferroelectric materials will be polarized.[21,41] The direction of polarization is rotated to change the conductance state of the tunnel. Figure 2.3 depicts a typical ferroelectric tunnel junction where a thin film of ferroelectric material plays the prole of a barrier between two electrodes.[42] Under an electric field, the ferroelectric material will be polarized to reduce potential profile changing at the barrier/electrodes interface, resulting in resistance changing. Moreover, the resistance was modulated continuously.[43]

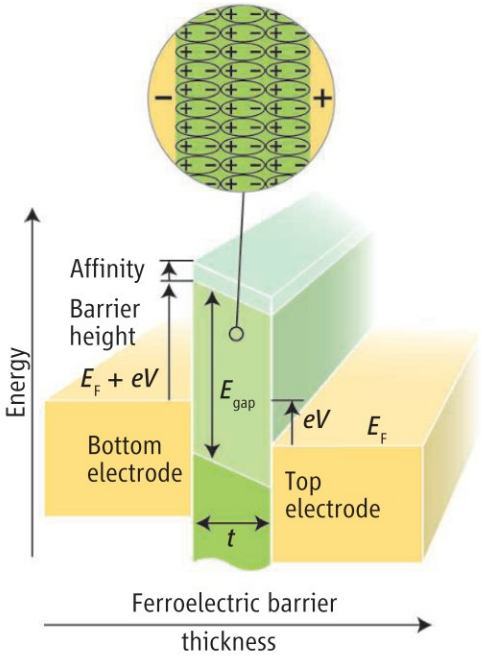

Figure 2.3. Schematics of ferroelectric tunnel junctions. Reprinted with permission[42]

2.1.2. Three-Terminals Artificial Synapse

Although two-terminal memristors have proved the non-volatile effect as neurons and synapses, memristors still face the shortage of high write noise, nonlinear switching property, and light energy consumption.[44] Therefore, another artificial synapse form emerges as synaptic transistors with an additional gate electrode. Compared with two-terminal memristors, these three-terminals (3T) devices offer the advantages of simultaneously writing and reading at different terminals without conflict.[6] Therefore, 3T artificial synaptic transistors deal with spatiotemporal information efficiently as neurons. Moreover, linear switching conductance is another feature that synaptic transistors was achieved through an electrochemical-based organic synaptic transistor.[44]

Due to the urgent desire of this new structure artificial synapse, multiple mechanisms have been proved during the past decades based on the interaction with the semiconductive layer, including charge trapping, ferroelectricity, ion migration, and electrochemical reactions.[41]

Charge trapping

Conductance modulation by charging trapping is realized by injected charge into the semiconductor layer. When a voltage is applied to the gate of synaptic transistors, charged carriers (hole or electron) are forced to inject or tract into the semiconductor layer, resulting in the threshold voltage variation. The changed state is maintained until an opposite voltage applies to the gate as the non-volatile effect.[45] As depicted in Figure 2.4, holes are injected into the C_{60}-PMMA channel under a positive bias while electrons are trapped in the channel with a negative voltage. As a result, the threshold voltage is shifted as the conductance modulation. Furthermore, an additional self-formed floating-gate (SFG) is also performed as a trapping layer for charge carriers.[46]

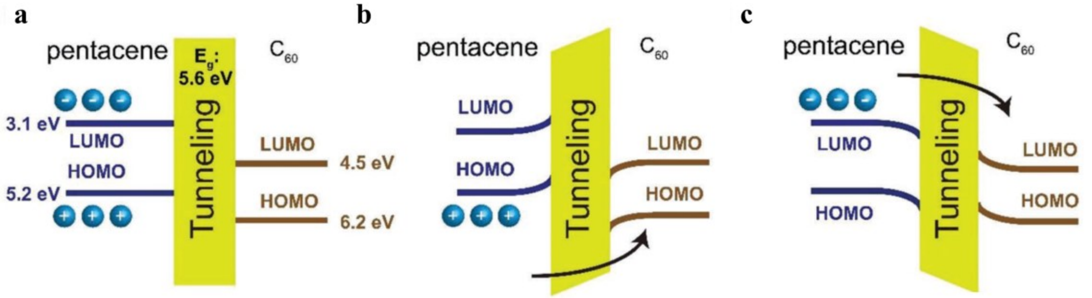

Figure 2.4. Mechanism of charge-trapping synaptic transistors. (a) Steady-state. (b) Hole trapping state. (c) Electron trapping state. Reprinted with permission[45]

Electrochemical reactions:

For electrochemical organic transistors (OECT), ions of the electrolyte gate are dopped inside the ion-gel-based semiconductor layer.[3] After introducing additional ions into the semiconductor layer, the conductance of the transistor is changed. Moreover, since this doping is irreversible that OECT is a promising candidate for non-volatile devices.[47] As depicted in Figure 2.5, anions in ion gel were electrochemically injected into poly(3-hexylthiophene) (P3HT) when a negative bias was applied on the gate, resulting in a hysteresis that was maintained for five weeks. By switching the direction of applied voltage, potentiation and depression are also controlled.[3]

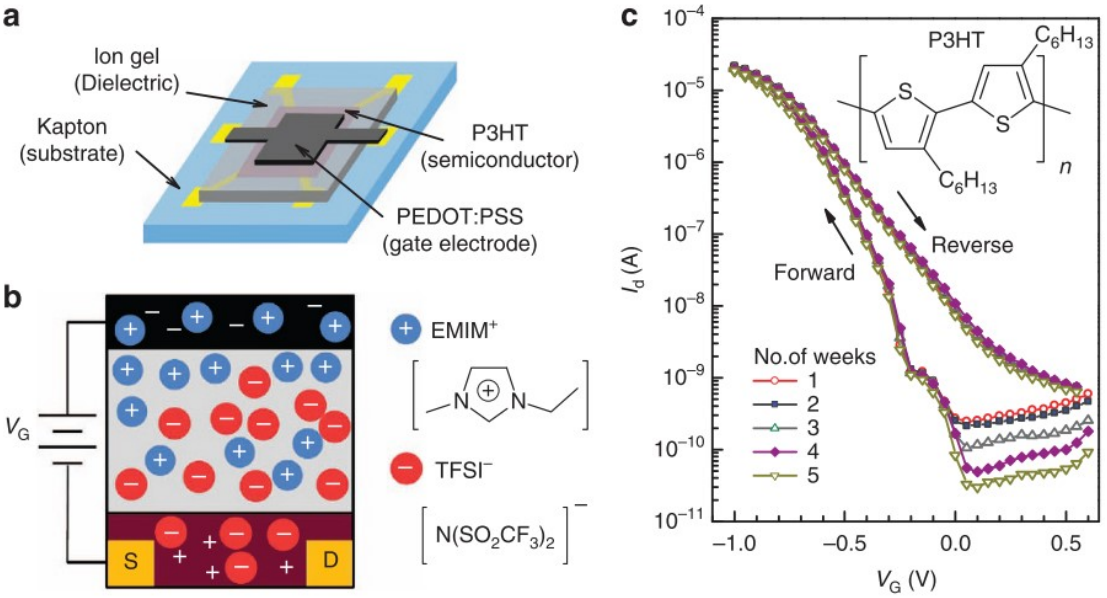

Figure 2.5. Mechanism of electrochemical reaction synaptic transistors. Reprinted with permission[47]

Ion migration:

A similar mechanism to modulate the source-drain conductance is based on ion migration by controlling the bias on the electrolyte gate. Although both electrochemical reaction and ion migration involve ions inside the electrolyte gate materials, the movable ions do not dope inside the semiconductive layer for the ion migration mechanism. Instead, ions only accumulate on the electrolyte and channel layer interface, resulting in an electrical double layer (EDL). The capacitive coupling by EDL will influence the channel's conductance, resulting in modulating the channel conductance and realizing synaptic functions. Since there is no electrochemical doping involved in the ion accumulation, the modified state only lasts for a short time.[48] Figure 2.6 depicts a liquid-gated EDL IGZO-transistor. A mixer of ethyl alcohol with potassium chloride (KCl) works as the gate electrolyte. Under a gate bias, self-ionized hydronium (H_3O^+) ions or hydroxide

(OH⁻) ions are facilitated by KCl to the interface to form an EDL. As a result, the performance of paired-pulse facilitation (PPF) was monitored as short-term synaptic plasticity.[49]

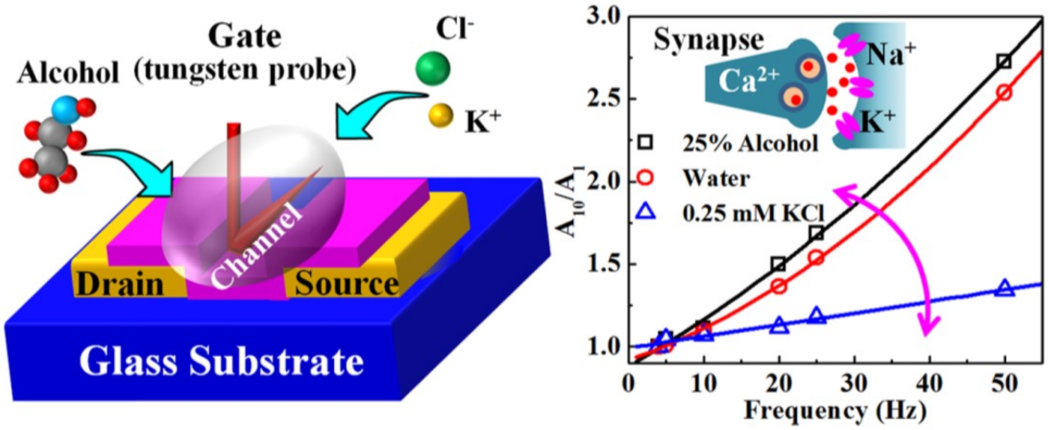

Figure 2.6. Schematics of ion migration synaptic transistors. Reprinted with permission[49]

Ferroelectricity:

For ferroelectric transistors, the conductance was also modulated by controlling the dipole alignment of the gate material.[50] As illustrated in Figure 2.7, ferroelectric layer zirconium-doped hafnium oxide (HfZrOx) fabricated between the semiconductive layer indium gallium zinc oxide (IGZO) and the gate electrode titanium nitride (TiN), resulting in a metal-ferroelectric-metal capacitor (MFM). Depending on the bias applying on the gate electrode, it induces an electron accumulation or depletion at the interface between HfZrOx and IGZO, which will influence the conductance of ferroelectric transistors. The capacitance of formed MFM reduces when there is a negative bias on the gate while increasing under positive bias.[51] Moreover, this modulation was maintained when the bias voltage was retrieved.

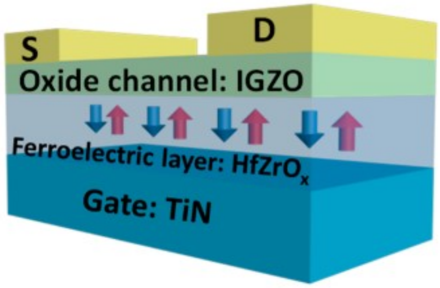

Figure 2.7. **Mechanism of ferroelectricity synaptic transistors. Reprinted with permission**[51]

2.1.3. Application of Neuromorphic System

Neuromorphic Systems with Sensory Functions

Pressure Sensing

The touching sensation in biological systems was emulated by a tactile-perception system. This biomimetic is constructed by integrating a pressure sensor with an organic synaptic transistor, as shown in Figure 2.8 (a).[13] The inputted pulse touching induced signal was applied on the gate, which influenced the conductivity of synaptic transistors. As a result, the detected signal was processed by the artificial synapse in the form of a synaptic current. Moreover, a complete signal perception procedure was also replicated by a sensory neuron, as shown in Figure 2.8 (b).[14] A biological sensory neuron is constructed by a receptor, axon, and synapse with the functions of stimulus sensing, signal transmitting, and signal processing, respectively. Thus, to entirely mimic the whole procedure, researchers demonstrated a neuromorphic tactile processing system (NeuTap) with a tactile sensor, ionic cable, and synaptic transistor.

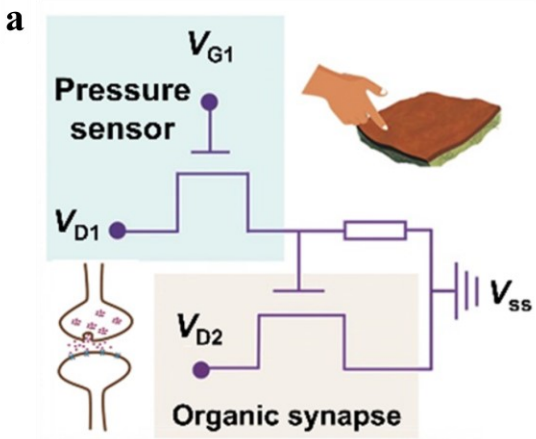

Figure 2.8. **Application for tactile sensation. (a) Organic transistor-based tactile perception system. Reprinted with permission**[13] **(b) artificial sensory neuron. Reprinted with permission**[14]

Light Sensing

In the biological system, calcium ions (Ca^{2+}) play an essential role, such as signal transmission between synapses.[52] Moreover, light illumination also controls the flux of Ca^{2+}.[53] Therefore, various studies have been carried out to mimic this process. For example, the resistance of $CH_3NH_3PbI_3$ ($MAPbI_3$) was switched under an electric field by forming iodine vacancies. Moreover, the formation process was modulated under light illumination. Thus, $MAPbI_3$-memristors-based neural networks were utilized to detect light (500 nm and 635 nm) intensity as nociceptors, as shown in Figure 2.9.[15]

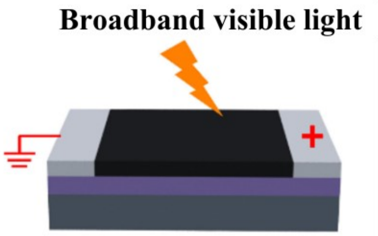

Figure 2.9. **Memristors-based optogenetics-inspired neural networks for light density detection. Reprinted with permission**[15]

Neuromorphic Systems with Motor Effector

As biological neuromorphic systems, despite sensing, neuromorphic systems also control artificial effectors.[6] Several neuromorphic systems were utilized to actuate artificial effectors.

Tactile Sensorimotor Synapse

Figure 2.10 illustrates an artificial afferent nerve with a pressure sensor was connected with a cockroach leg as bio reflex arc.[54] The artificial afferent was constructed by a resistive-based pressure sensor, a ring oscillator, and a synaptic transistor which converted and transmitted the pressure information. Eventually, the output current was amplified as a voltage that was utilized to control the movement of a cockroach leg.

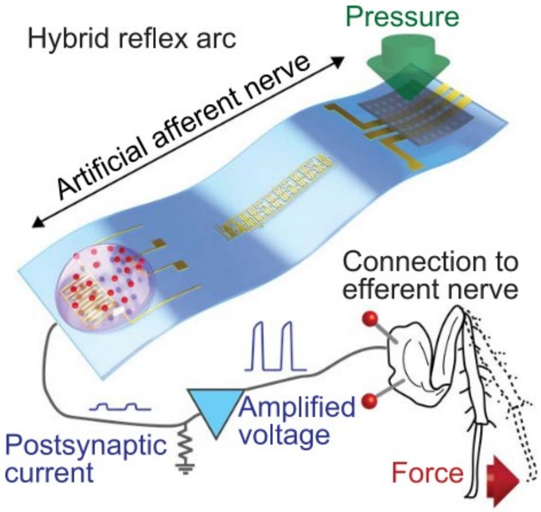

Figure 2.10. Artificial afferent nerve controls the motion of a cockroach leg. Reprinted with permission[54]

Optoelectronics Sensorimotor Synapse

The vision-based response to the environment has also been studied. For example, light cognition and muscle manipulation were united through an optoelectronic sensorimotor system.[55] As depicted in Figure 2.11, a polymer-based artificial muscle was actuated by the optical stimulation through an artificial synapse. Thus, human-inspired light cognition and light-driven actuation were successfully emulated, which enlarged the possibility for bio-inspired controlling for prosthetics and robotics.

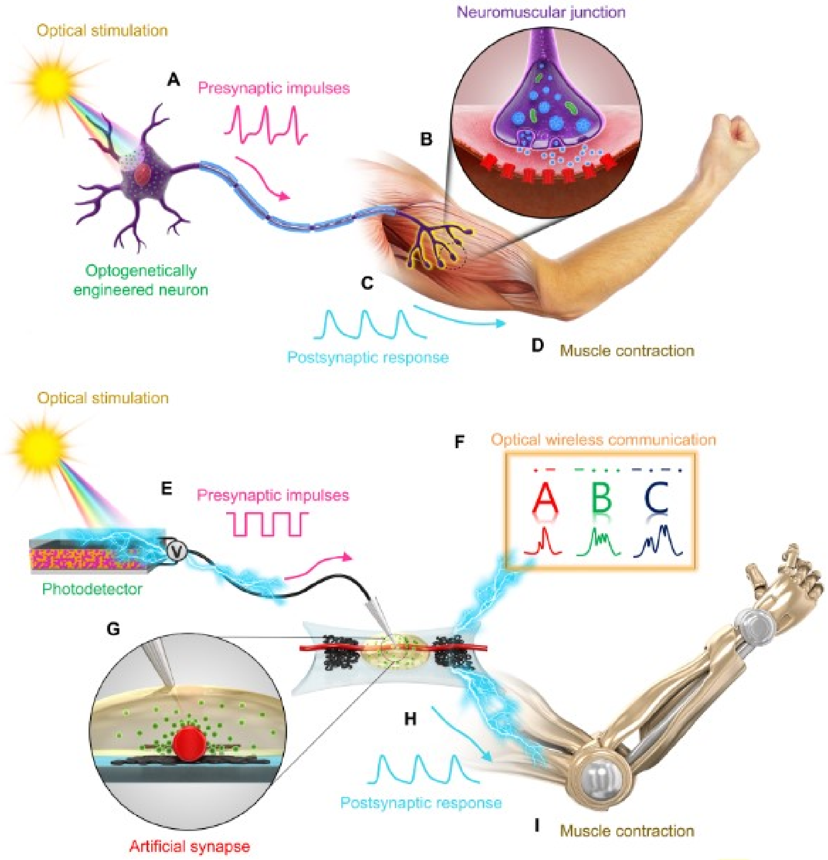

Figure 2.11. Bio-inspired light-controlled muscle manipulation by an optoelectronic sensorimotor neuromorphic system. Reprinted with permission[55]

Nociceptors Sensorimotor Synapse

The human sense of pain was mimicked by a memtransistor-based neuromorphic nociceptor, as shown in Figure 2.12.[4] The sign detected by a pain detector was transmitted through an afferent pathway to the artificial spinal cord or the artificial brain, where an efferent stimulus was produced to control the artificial muscle. Moreover, this control strategy was successfully implemented to control the motion of robotics.

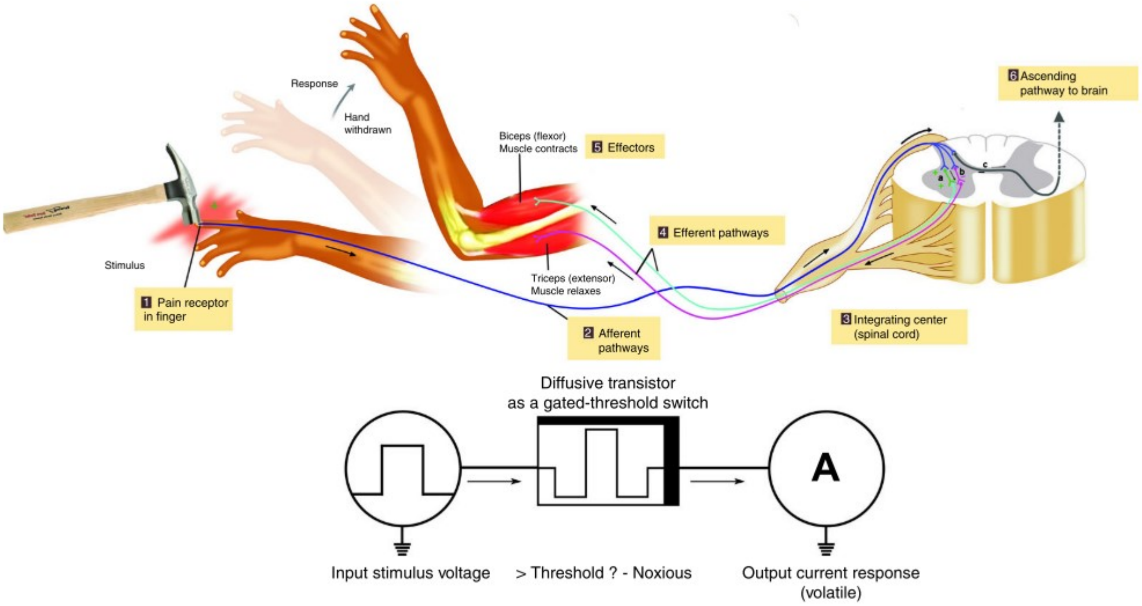

Figure 2.12. Memtransistor formed neuromorphic systems as nociceptors. Reprinted with permission[4]

2.2. 3D Printing Technologies

3D printing, so called additive manufacturing, origins from the rapid prototyping method for three-dimensional components in the 1980s.[56] It is developed for the fabrication of prototypes and complex structures cost-efficiently. In addition, current 3D printing technologies provide another feature of design-free. With the development of design software, fabrication, and controlling technic, various 3D printing approaches have already been innovated.[56] Regarding the state of materials, 3D printing technologies are classified as filament-based based fused filament fabrication (FFF), resin-based stereolithography (SLA), paste-based direct ink writing (DIW), and powder-based selective laser sintering (SLS).

2.2.1. Filament-based Fused Filament Fabrication (FFF)

Fused deposition modeling is carried by heating filament when it passes through the printer head. Then, the melted filament coming out from the nozzle is deposited on the substrate or already printed structure layer by layer. By controlling the pattern of each layer through the nozzle's motion, a three-dimensional part is achieved layer by layer. This method is typically carried out for the fabrication of mechanical parts. Meanwhile, polymer-based filaments are the most common material used by FFF due to the low melt temperature for low energy source requirements. In addition, PLA-based functional materials, such as conductive PLA filaments, magnetic PLA filaments, even wood PLA firmaments, are also available in the market. Furthermore, metal components were obtained by FFF, which requires high-energy power sources, such as plasma, and electron/laser beam.[57]

2.2.2. Resin-based Stereolithography (SLA)

3D Systems, Inc. firstly demonstrated the resin-based stereolithography (SLA) technology in 1986.[58] Same as FFF, the model is virtually sliced to different layers by computer-aided software.[58] Then, the slice document will control the scanning beam shape for each layer and project to the liquid resin, as depicted in Figure 2.13. The material for SLA usually refers to a photocurable resin that is crosslinked under an ultraviolet (UV) laser. After complete one layer, the platform lowers a distance as the virtual layer thickness. It is possible to be lifted up if the position of the scanner beam comes from the bottom. After printing, the prefabricated sample needs to be washed with solvent, followed by a further UV curing treatment to confirm the solid-state of the printed samples. Since the resolution of fabricated parts is dependent on the resolution of projected UV lights, the cutting projecting technologies advanced the resolution up to the micrometer range.[58] With the projection micro stereolithography technique, an ultra-light and -stiff microarchitecture with nano feature was demonstrated.[59]

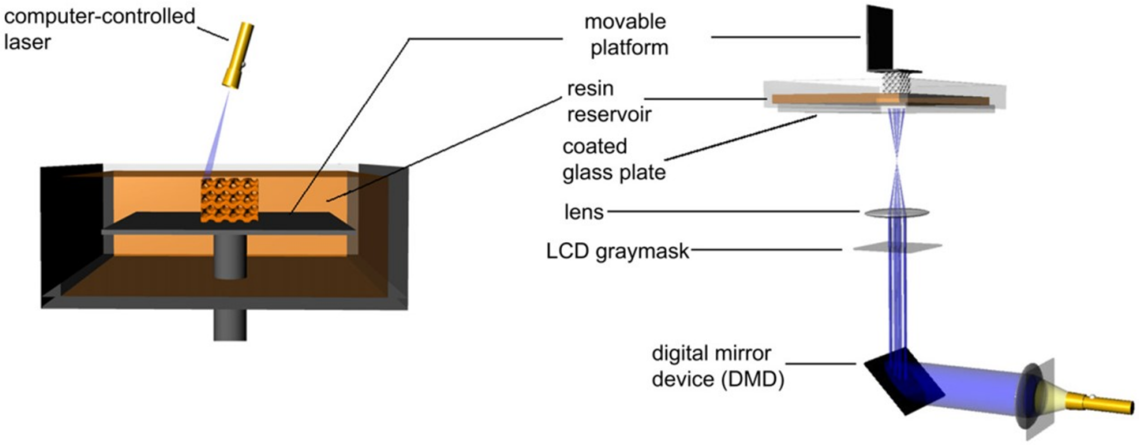

Figure 2.13. Schematics of stereolithography device. Reprinted with permission[58]

2.2.3. Powder-based Selective Laser Sintering (SLS)

Two powder-based additive manufacturing systems, powder feed system and powder feed system, have been applied as metal forming, as shown in Figure 2.14.[57] A high-energy beam (electron or laser) is necessary for metal fabrication by melting the powder and forming 3D structure components point by point.

The process of printing by SLS is similar to FFF that the designed 3D components are firstly sliced into different layers under the defined layer thickness and filled with chosen patterns for each layer. Then, a laser is scanning on the bed surface for powder bed systems, following the route of the filling pattern on each layer. After complete one layer, the powder bed goes down, and a fresh powder layer will be laminated by a powder supply system. The system will continuously print layer by layer until a 3D component is achieved. A power supply system is more similar to FFF since the only variation is alternating filaments with powder.

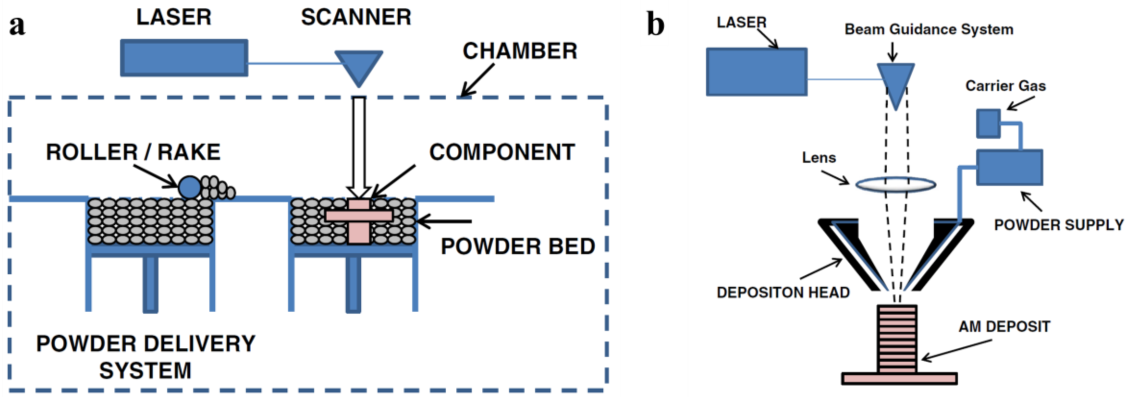

Figure 2.14. Two types of powder-based SLS systems. (a) Powder bed systems, and (b) Powder feed systems. Reprinted with permission[57]

2.2.4. Paste-based Direct Ink Writing (DIW)

Unlike filament, resin, and powder-based 3D printing methods for 3D structural components, the paste-based direct ink writing (DIW) method is typically applied to fabricate planar patterns on surfaces with functional materials. For DIW, pastes are stored in a contained and extruded through a nozzle under the force of compressed air or screw with a set speed, as shown in Figure 2.15.[60,61] 3D structural electronics and sensors were also printed layer-by-layer.[60] Moreover, with laser or UV light assistant, 3D structural objects were sintered after printed.[62,63]

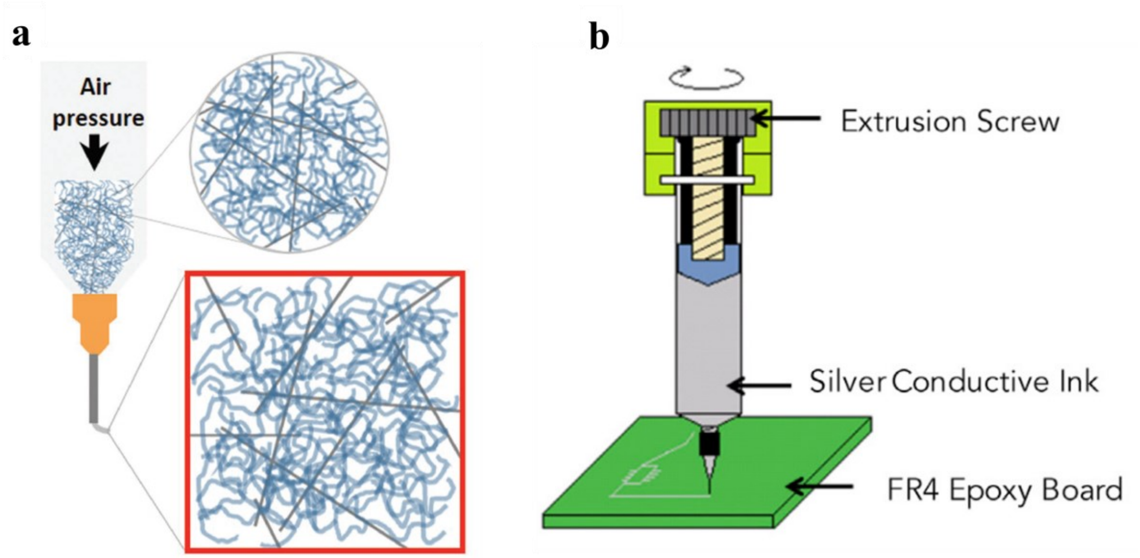

Figure 2.15. Paste-based direct ink writing (DIW). (a) Extrusion force from compressed air. Reprinted with permission[60] **(b) Force from screw extrusion. Reprinted with permission**[61]

Chapter 3.

3D Printed Electrochemical Sensor

This chapter discusses a 3D printed electrochemical sensor for detecting environmental signals as a bio-sensory afferent. A Poly (vinyl chloride) (PVC) based-ion selective electrode sensor (ISEs) was fabricated by the DIW method for ion concentration monitoring. The performance of the fabricated ISEs was optimized by increasing the stability of reference electrodes. Inorganic transistors were also fabricated by the 3D printed method. Two types of electrodes design were studied by comparing their electrical performance. Then, a 3D printed ISEs was connected to the backside of a 3D printed inorganic transistor as hybrid ion-selective field effect transistors (ISFETs). As a result, the ions produced potential was working as the gate bias of the transistor. Thus, the ion concentration-related potential was used to influence the conductance of the inorganic transistors. The sensitivity and selectivity of the hybrid ISFET were also studied through an interference experiment. After approving the selectivity, the 3D printed hybrid ISFET was finally utilized to detect the ammonium ion concentration in artificial saliva.

The chapter includes sections derived from the journal paper: **C. Bao, M. Kaur, and W. S. Kim. *Toward a highly selective artificial saliva sensor using printed hybrid field effect transistors*. Sensors and Actuators B: Chemical 285 (2019)186-192. Note: Used with permission from Elsevier.**

3.1. Abstract

Ion-selective field effect transistors (ISFETs) have been widely used in biological and environmental sensing applications. However, the rigid feature of common ISFETs blocked the real-time monitoring applications. Here, we report a feasible 3D printing method to fabricate flexible ISFETs by hybridizing printed organic ion-selective electrodes and inorganic transistors. The fabricated ISFETs demonstrated high sensitivity, ranged about 100 mV/decade, towards ions such as ammonium (NH_4^+), potassium (K^+), and calcium (Ca^{2+}). Furthermore, the fabricated hybrid ISFETs showed their distinct selectivity from the mixture of various interference ions as artificial saliva. This capability provides an

integrated platform for a comprehensive ion analysis by closely monitoring interrelated saliva parameters as wearable healthcare solutions manufactured by 3D printing methods.

3.2. Introduction

Ion-selective field-effect transistors (ISFETs) are integrated devices consisted of ion-selective membrane electrodes and field-effect transistors. ISFETs have been developed for decades demonstrated high sensitivity.[64,65] ISFETs are reported to detect the pH value,[66–68] followed by the measurement of other ions.[69] Recently, major applications are focused on biomedical,[70–76] and environmental monitoring fields.[77] Based on the type of ion-selective membranes, ISFETs are categorized into polymer-membrane ISFET, glass-membrane ISFET,[78,79] nanotube-membrane ISFET,[80,81] and enzyme-membrane ISFET.[82,83] Among these, lots of applications have been developed with polymer-membrane ISFETs, because of their substrate adaptability and feasible formability. Poly (vinyl chloride) (PVC) is the most widely used among other polymer membranes.[84,85]

Despite the wide usage of PVC membranes, the direct contact of membrane on the FET’s gate causes significant issues, such as the degradation of polymeric semiconducting layers or polymeric gate insulators by drop-casted membrane solutions.[84] One effective way to overcome this problem is using a hybridizing method, by connecting the ion-selective membrane electrode directly with an extended gate. Compared with conventional ISFETs, the hybrid ISFETs have the advantage of high stability and selectivity by overcoming the disadvantage of chemical or biological instability for the monitoring of the environment.[68,86–92] A double-gate method has also been introduced to improve the pH detecting sensitivity,[93] while back-gate type ISFETs are usually utilized for the nanowire type ISFETs.[94–96]

Recently, the demand for real-time health monitoring requires the appearance of wearable devices. There has been a lot of attention among several research groups on the possibility of using flexible ISFETs.[65,97–99] Flexible ISFET-based biosensors have been fabricated on polyethylene naphthalate (PEN) substrate for pH detection.[100] In order to control FETs’ pattern dimensions precisely, lithography processes have been introduced to fabricate FETs with channel length in the scale of micrometers using vacuum-based sophisticated instruments.[73,101] Also, the printing method, such as screen printing, has been utilized to fabricate ion-selective electrodes.[72,102–104] However, lithography methods need sophisticated equipment, and the screen printing lacks local registration of multi-layers. These drawbacks are solved wisely with the 3D printing method because it offers a flexible manufacturing process available for hybrid integration of smart 3D designs with cost-efficient equipment. The 3D printing method, especially direct writing, we utilized here, is a deposition method used for any kinds of surface properties with precise position arrangement. This technique utilizes solid paste compared to conventional inkjet printing, which relies much on the substrate's surface properties. Different 3D printing processes, such as the aerosol jet printing method introduced to fabricate flexible pH sensors,[105] and an e-tongue application for soil analysis[106] were also reported recently.[107–110]

The reliable tracking of important ions such as K^+, NH_4^+, and Ca^{2+} is one of the key indicators for the human body's metabolism monitoring.[80,111,112] Real-time health monitoring is available by detecting these ions' changes in blood, urine, sweat, or saliva, et al. Among them, saliva has the advantage of being conveniently extracted by a non-invasive way. 'Passive drool' has been widely used to detect objects.[113] Artificial saliva is usually prepared for the detection of salivary uric acid,[113] and heavy metal ions such as Hg, Cu, and Zn for tracing dental metal erosion.[114] The selectivity of K^+ and Na^+ ions by the nanotube-based sensor has also studied using synthetic saliva.[115]

In this thesis, we firstly report a feasible 3D printing method to fabricate flexible ISFETs via a direct connection between the oxide FETs and ISEs to form hybrid ISFETs. 3D printed FETs and ISEs are separately verified for confirmation. Then, the sensitivity and selectivity of the hybrid ISFETs were further investigated. Finally, the possibility of the hybrid ISFETs for NH_4^+ detection in artificial saliva from the mixture of interference ions was demonstrated. This expands the application of the 3D printed hybrid ISFETs in the field of non-invasive real-time health monitoring as one of the next-generation electronic tongues.

3.3. Fabrication and Characterization

3.3.1. Fabrication

Printed Field Effect Transistor (FET) Fabrication

In order to secure semiconductor material's chemical stability, zinc tin oxide (ZTO) was fabricated on a silicon wafer.[116] The ZTO solution was prepared by mixing 20 grams of 2-methoxyethanol, 0.3 mol of zinc acetate dehydrate, 0.3 mol of tin (II) chloride, and 0.3 mol of acetylacetone following by magnetic stirring for 12 h at room temperature. Then, the ZTO semiconductor layer was fabricated by spin-coating of the ZTO solution on UV ozone treated, single-side polished silicon wafer <100>, followed by 30 min-150 ℃ pre-baking and 60 min-500 ℃ hard baking. Finally, source and drain FET electrodes were 3D printed on the semiconductor coated silicon wafer by a direct writing printer (V-One, Voltera, Canada) with a slow feed rate of 100 mm/s, followed by curing at 150 ℃ for 10 min. Interdigitated electrodes were 2.5 mm in width, and the serpentine-shaped electrodes had 2mm in radius.

Ion-Selective Electrode Fabrication

Working and reference electrodes were 1mm in width and printed on polyimide (PI) substrate by the same 3D printer with the same curing parameters for FET. The silver paste was formulated with 0.4 g of polyurethane, 0.2 g of custom prepared silver nanoparticles,[117] and 2g of silver flake (Inframat Advanced Materials, US), mixed with 1 ml of N, N-dimethylformamide (DMF), and 4 ml of tetrahydrofuran (THF). The detecting area on the working electrode was 6 mm in diameter, fully covered by an ion-selective membrane to avoid shorting loop between the working and reference electrode.

ISFET Fabrication

The integration of ISEs and FETs was carried out by scratching the backside of printed FETs with a diamond glass knife, followed by connecting to the working electrode of the printed ISEs directly before baking.

Ion-Selective Membrane Fabrication

After integrating hybrid ISFETs, 60 µl ISE solution was drop-casted on the detecting area of working electrodes followed by a 24 h evaporation in a fume hood. The basics material for polymeric membrane was PVC-THF solution made by dissolving Poly (vinyl chloride) (PVC) into Tetrahydrofuran (THF). For ammonium ion membrane, additional 1 mg sodium tetrakis [3,5-bis (trifluoromethyl) phenyl]borate salt (NaTFPB), and 80.6 mg bis(2-ethylhexyl) sebacate with 2.4 mg nonactin as ionophore were added into PVC-THF solution while calcium membrane used 1.43 mg N,N-dicyclohexyl-N0,N0-dioctad ecyl-3-oxa- pentanediamide (ETH-5234, selectophore purity grade) as ionophore with 92 µL plasticizer 2-nitrophenyl octyl ether (2-NPOE). For potassium ion membrane, 1 mg potassium tetrakis (4-chlorophenyl) borate (KTpClPB) with ionophore 4 mg valinomycin, and 129.4 mg plasticizer dioctyl sebacate (DOS) were dissolved in PVC-THF solution.[84,118] All membranes were conditioned in 1 M corresponding solution before use.

Silver Chloride Coating

The silver chloride layer on the reference electrode was coated by placing a droplet of Clorox ® bleach (8.25%) on the end of the reference electrode for 10 min, followed by DI water washing to avoid the residual solution interference for later testing.[119]

Preparation of Artificial Saliva

Basic artificial saliva for ammonium interference study was made by mixing sodium chloride (13.2 mg), potassium chloride (96.4 mg), calcium chloride (17.2 mg), potassium phosphate monobasic (65.0 mg), urea (20.4 mg), and lactic acid (17.4 mg) together in 100ml DI water.[120] Then, different concentration of ammonium ion solution was prepared with the basic artificial solution.

3.3.2. Characterization

The electrical performance of FETs and ISFETs was carried out on semiconductor probe station 4200-SCS (Keithley, USA). Each concentration solution was transferred from the vial to the sensor area by micropipette, followed 1 min data recording. The open circuit potential of ISEs was collected by potentiostat CHI1205B (CH Instruments, Inc., USA) with a 0.1s sample interval for 1min. The images of printed FET electrode were performed by microscope NJF-120A with 4X objective lens (HINOTEK, China) and captured by software ScopeImage 9.0.

3.4. Results and Discussion

Interdigitated electrodes (IDEs) have been widely used in biosensor and chemical sensing due to their simplicity, high contact area, and multi-physical reactions.[121–123] Serpentine-shaped source and drain electrodes are alternative choices for securing uniform channel in FETs.[116] Both channel types have been fabricated by the direct-writing-based 3D printing method demonstrated in Figure 3.1a and Figure 3.1b. It is clearly indicated that a uniform channel was obtained easily with a serpentine-shaped structure compared with IDE design because the serpentine-shaped design reduces pauses and anti-stringing during the writing process that leads to a larger and irregular channel width at the end of each line, as shown in Figure 3.1a and Figure 3.1b. Although the channel length is changed by design, the variation of printed channel length in IDE is much larger than that of serpentine structure, as shown in Figure A1. Moreover, the change of channel length was investigated before and after baking of silver paste. Variation with 9 μm was observed because of volume shrinkage during thermal baking, as shown in Figure A2. As a result, this shrinkage is reverse-engineered for obtaining an aimed channel length during the design stage.

The electrical performance between those two-channel designs is also compared in Figure 3.1c ~ d. Although both FETs have similar electrical performance, the reproductivity of FET fabrication with a uniform channel guarantees a stable performance with a serpentine shape structure. Therefore, serpentine-shaped source and drain electrodes for FETs were selected to demonstrate 3D printed ISFETs.

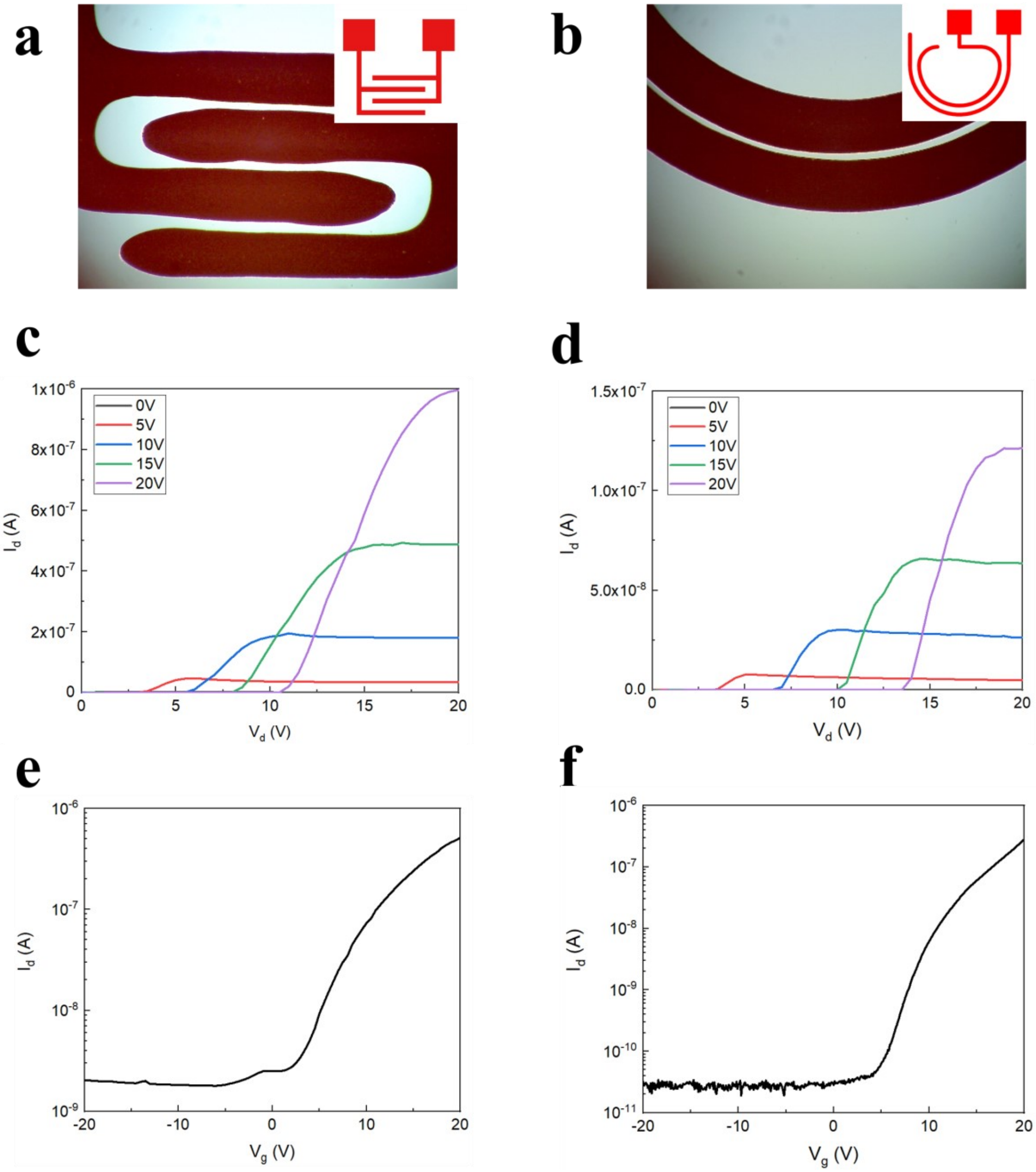

Figure 3.1. **Preparation of two different hybrid FET designs. (a) and (b) Top view of printed FETs with IDE and serpentine-shaped channel (Inert images are the schematic of IDE and serpentine shapes, respectively). (c) and (d), and (e) and (f) Output and transfer curves of printed IDE and serpentine structure, respectively.**

After the verification of the printed FETs, printed ISEs were also characterized before being combined with printed FETs. Three types of PVC membrane were fabricated for NH_4^+, $K^{+,}$ and Ca^{2+} ions after being saturated in the corresponding 1 M solution. As shown in Figure 3.2a, the NH_4^+ membrane showed a linear response in the range of 10^{-6}

~ 1 M that was matching with the Nernst equation. Similar trends are observed for K^+ and Ca^{2+} ion membranes with a detection range of 10^{-6} ~ 1 M and 10^{-4} ~ 1 M, respectively, as shown in Figure 3.2b and Figure 3.2c.

In order to make the reference electrode (RE) to be stable enough to improve the stability of ISEs for repeated usage, a silver chloride (AgCl) layer was coated on the RE. The performance comparison of different ISEs is shown with and without AgCl in Figure 3.2d. It is clear that the AgCl improved the linear relation between open circuit potential and ion concentration significantly. And this enhanced the detecting stability of the fabricated ISE. Moreover, the change of potential during the detection range with AgCl coating was much larger than that without the AgCl layer.[119] For NH_4^+ ISE, the variation of potential increased from 0.28 V to 0.40 V after AgCl coating. Especially, the average of each level of NH_4^+ concentration grew from 70 mV to 100 mV, enhanced with 43 %. Therefore, the apparent RE performance improvement with AgCl coating enhanced the selectivity of ion-selective membranes. The improvement for K^+ was 47 % from 73 mV to 107 mV, and that of Ca^{2+} membrane was 10 % from 60mV to 66mV, respectively. Based on this improved result, AgCl was applied for the fabrication of hybrid ISFET, as shown in Figure 3.3a.

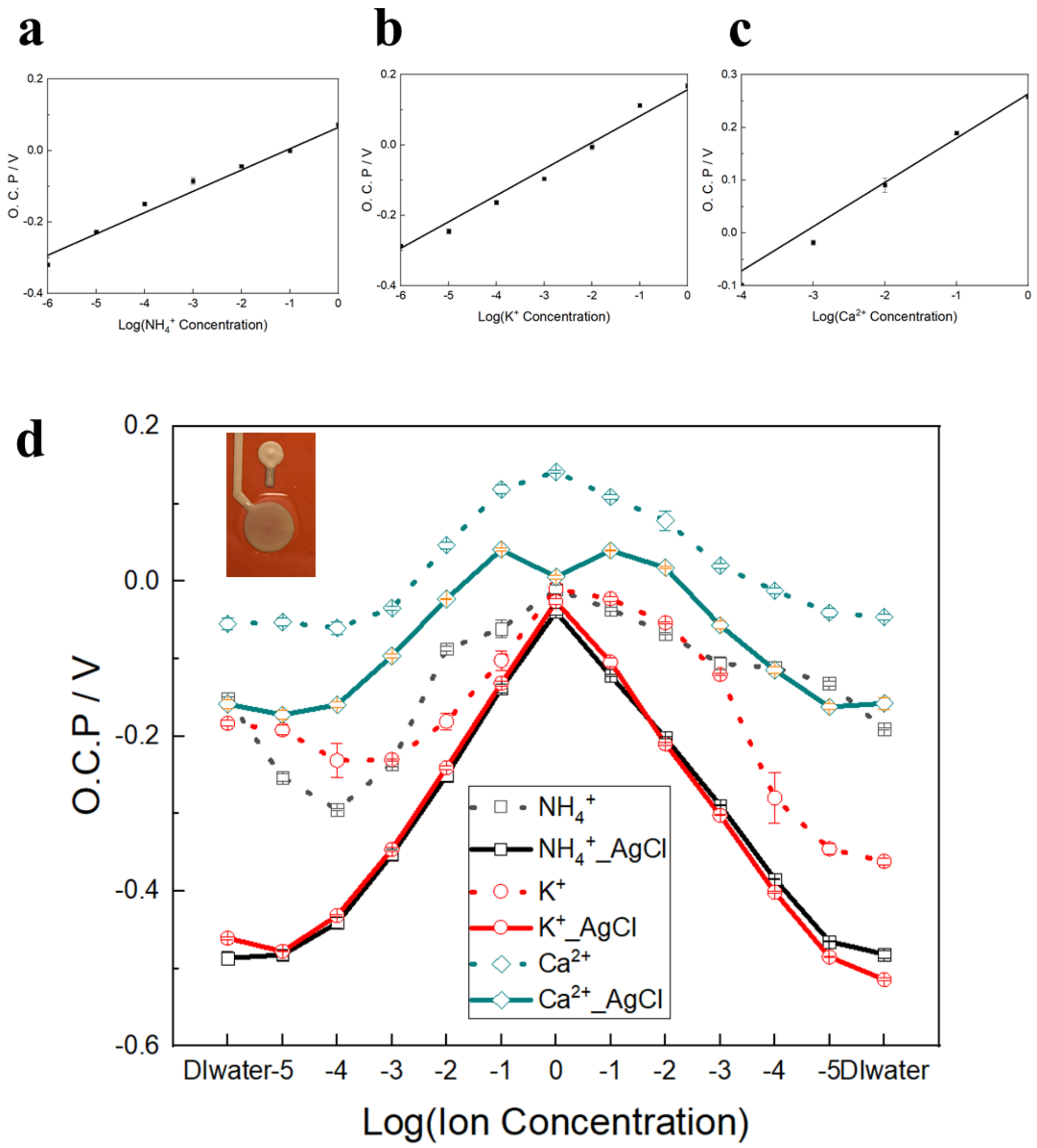

Figure 3.2. **Open circuit potential characterization (O. C. P.). (a), (b) and (c), results of O. C. P for NH_4^+, K^+ and Ca^{2+} ion-selective membrane respectively. (d) Improved results of sensing stability for three ion-selective membranes with AgCl coated RE (the inset shows the actual membrane-coated electrodes).**

Figure 3.3b and Figure 3.3c show the design and actual images of fabricated hybrid ISFET arrays with ion-membrane coated gates. The performance of ISFETs was measured by a three-probes semiconductor characterizing system. The stability of printed hybrid ISFET was evaluated by recording the output voltage drift over a long period before being carried out for ion concentration detection, as Figure 3.3d shown. It's only 10 seconds before the drain voltage reaching to a relatively stable value which could be kept for 600s.

The hybrid ISFETs are designed as shown in the schematic, Figure 3.3a. It illustrates how the separately printed ISEs and FETs are integrated together into a single device. When a positive voltage is applied to the gate, negative electrons in the semiconductor are pulled to the bottom of the gate. After enough electrons get accumulated, the channel between the source and drain opens, causing a current to flow inside the channel, with applied gate voltage to drain. Additional voltage is produced on the gate when an ion-selective membrane is integrated with FET through the extended gate. Therefore, the sum of the applied voltage and the voltage produced by ion-selective membrane influences the electrical performance of FET, namely the conductivity of the semiconductor channel. As a result, the current between drain and source will vary with ion concentration since the potential produced by ion-selective membrane changes when the ion concentration fluctuates. Based on this mechanism of ISFET, the drain voltage was recorded after applying a constant gate voltage (V_g = 1 V) and drain current (I_d = 100 x 10^{-12} A) by semiconductor probe station, as shown in Figure 3.3e. Ion concentration was increased from 10^{-5} M to 1 M before down to 10^{-5} M again with a decade step.

From Figure 3.3e, it is found that the drain voltage varies with the concentration of NH_4^+ ions. It is assumed that the potential change induced by ion concentration variation is compensated by the fluctuation in drain voltage to maintain a constant drain current. The linear relation between drain voltage and concentration is shown in the calibration curve, as Figure 3.3f showing, which is similar to Figure 3.2d. The sensitivity slope for NH_4^+ - ISFET is 98mV/decade while it was 100 mV/decade for NH_4^+ - ISE. These similar results between ISFETs and ISEs confirmed the aforementioned ISFET mechanism that the applied gate voltage plus the potential produced by ISEs influence the performance of transistors. Regarding K^+ -ISFET and Ca^{2+} -ISFET as shown in Figure 3.3g and Figure 3.3h, the sensitivity slope is 104 mV/decade and 42 mV/decade, respectively. This result is similar to the slope of their corresponding ISEs, 107 mV/decade and 66 mV/decade, respectively. The short circuit of the PVC membrane was excluded by extra experiments, as shown in Figure A3.

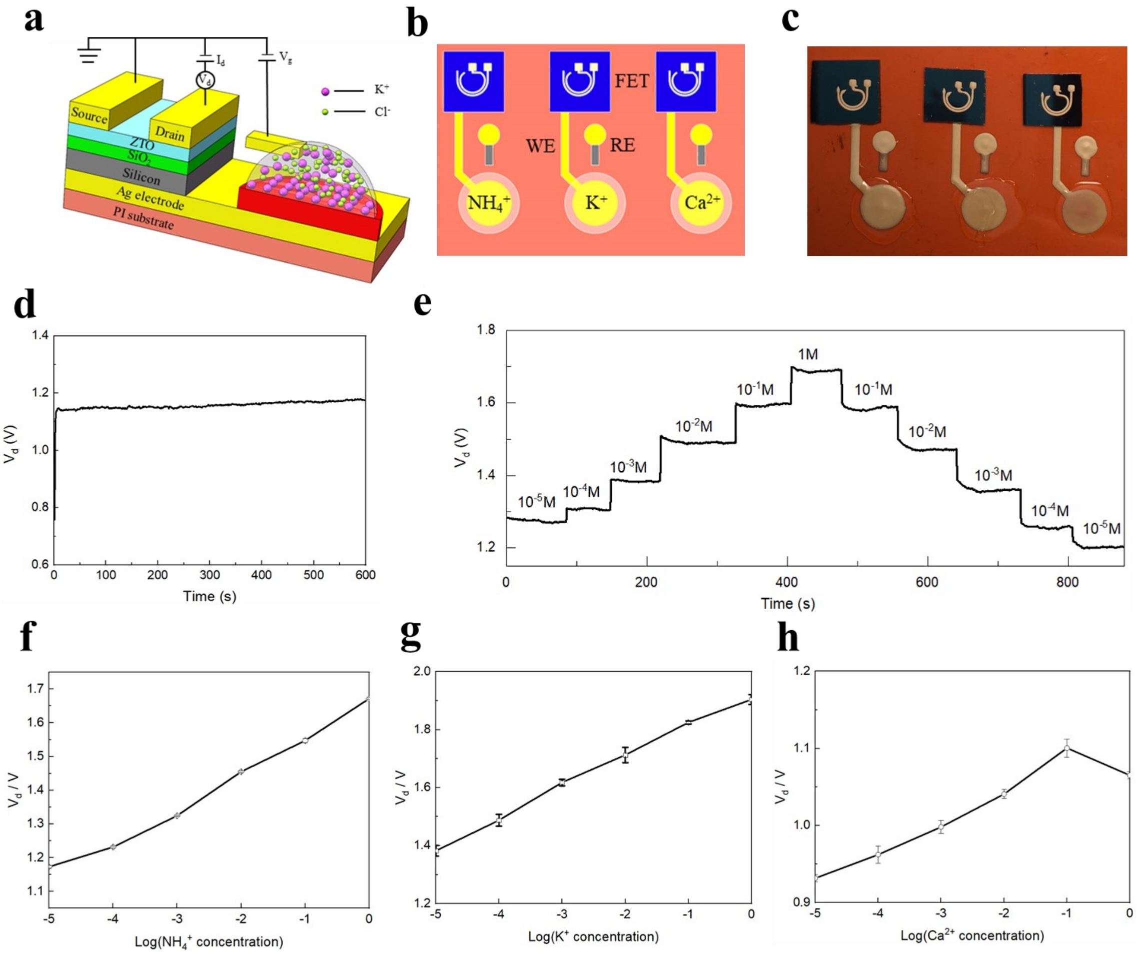

Figure 3.3. **Characterization of ISFET arrays. (a) Schematic of ISFET. (b) Schematic of ISFET array design. (c) Top view of the fabricated ISFET array. (d) Drain voltage drift vs. time. (e) Drain voltage drift depending on NH_4^+ ion concentration. (f), (g) and (h) Change of the drain voltage for NH_4^+, $K^{+,}$ and Ca^{2+} sensors depending on ion concentrations respectively with a constant drain current and applied gate voltage.**

The interference study was performed to confirm the selectivity of the fabricated ISFET arrays. The separated method determines the selectivity for different ISFETs. The selectivity of NH_4^+-ISFET was conducted by detecting pure primary NH_4^+ ion solution followed by pure interfering ions, including K^+ and Ca^{2+} solution. The electromotive force (EMF) between the working and reference electrodes in ISEs is defined by the Nikolsky equation, as shown in Equation 3.1[124]:

$$E = \mathrm{E}^0 + S \log \alpha \qquad \text{(Eq. 3.1)}$$

For interfering ions, the Nikolsky equation is modified as Equation 3.2:

$$E = \mathrm{E}^0 + S\log(K\alpha) \tag{Eq. 3.2}$$

where K is the selectivity coefficient, and S is the sensitivity slop of calibration curve for ISEs, as shown in Equation 3.3:

$$S = 2.3026\frac{RT}{ZF} \tag{Eq. 3.3}$$

where R, T, Z, F are gas constant, absolute temperature, charges numbers, and Faraday constant, respectively. Based on Equation 3.2, the absolute EMF value of ISEs for the primary ion is larger than that produced by interference ions due to the main transfer function of the membrane for the primary ion. From Equation 3.3, the sensitivity slope of the primary ion is the same as that for interference ions with the same charge while it is half with doubled charges. Regarding the results in Figure 3.4a for ISFETs, the sensitivity slope for the primary NH_4^+ is 95.77 mV/decade, which is nearly the same as that for the K^+ ion solution, which is 101.08 mV/decade. While it is twice that for Ca^{2+} solution as 63.95 mV/decade, due to the double charges of Ca^{2+} ion. Moreover, the absolute value for the primary NH_4^+ ion at each concentration is also higher than that for the interference K^+ and Ca^{2+} ions. The same method is used for K^+ -ISFET and Ca^{2+} -ISFET, as shown in Figure 3.4b and 3.4c. The primary sensitivity slope for K^+ -ISFET was 114.32 mV/decade with interference ion slopes of 91.88 mV/decade for NH_4^+, and 53.52 mV/decade for Ca^{2+}. For Ca^{2+} -ISFET, the primary sensitivity slope was 58.58 mV/decade, while the interference slope for NH_4^+ was 72.22 mV/decade and for K^+ was 71.88 mV/decade. This demonstrated that the EMF theory governing ISEs matches well with the fabricated ISFET arrays. Moreover, the average minimum voltage differences at each concentration between the primary and interference ions were 40 mV, 118 mV, and 75 mV for NH_4^+, $K^{+,}$ and Ca^{2+} membrane, respectively obtained by a separated interference study method. The voltage difference was benefited to distinguish the signal produced by primary ions when interference ions were existing.

Nevertheless, the actual solution in field usually contains multiple interference ions. Therefore, a fixed interference method was introduced to mimic real online ion concentration change monitoring. Since artificial saliva was widely used in the quantitative study,[120,125–128] an artificial saliva solution with a mixture of several ions (including K^+, $NH_4^{+,}$ and Ca^{2+} ions together) and distinct NH_4^+ ion was designed and prepared to verify whether the fabricated hybrid ISFETs selectively detect the distinct ion from interference ions using NH_4^+ -ISFET under a constant interference ion concentration shown as Figure 3.4d. The calibration curve for V_d-Log for NH_4^+ concentration was obtained, as shown in Figure 3.4e. A clear linear relationship between the drain voltage and NH_4^+ concentration was observed in the range of 10^{-4} ~ 1 M for NH_4^+ -ISFET. It demonstrated distinct selectivity of the fabricated ISFETs even with interference of multiple ions.

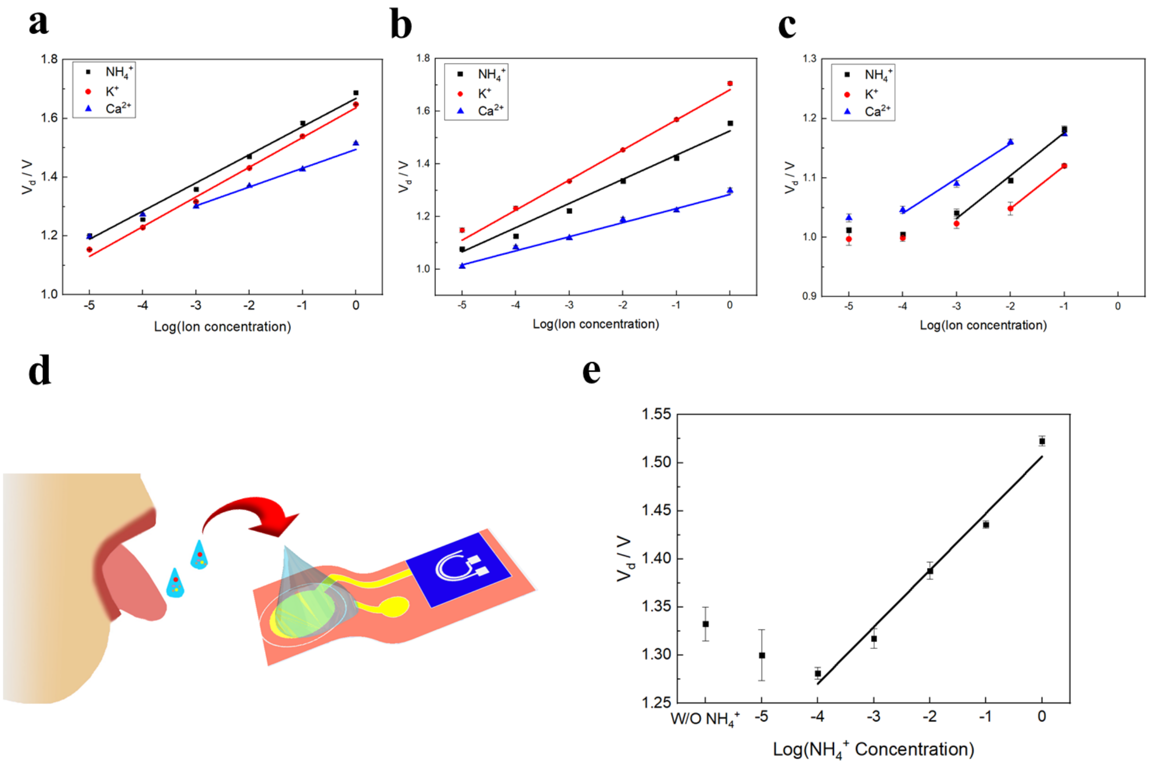

Figure 3.4. **Interference study of ISFETs with different ion-selective membranes. (a), (b) and (c) Selectivity of NH_4^+, K^+, and Ca^{2+} type ISFET respectively (solid black square, solid red circle, and solid blue triangle represent NH_4^+, K^+, and Ca^{2+} ions, respectively). (d) Schematic of the application for selective ion detection in artificial saliva. (e) Drain current change depending on NH_4^+ concentration in artificial saliva.**

3.5. Conclusion

In this chapter, we report the ion-selective sensors fabricated with 3D printed hybrid transistors. The proposed serpentine-shaped channel design demonstrated the improved reproductivity of uniform channels. The fabricated ISFETs showed reliability with a negligible variation of slope value for potential vs. ion concentration curves as ISEs. In order to confirm the selectivity of ISFETs, an interference study was performed. Moreover, the high selectivity of ISFETs with a mixture of interference ion concentration in artificial saliva was demonstrated. This expands the possibility of wearable ISFETs for real-time monitoring in bio-medical applications.

Chapter 4.

3D Neuromorphic Sensory System-Electrochemical Sensing

This chapter presents a 3D neuromorphic system with bio-inspired signal perception. Electrochemical detection was selected as a demonstration here. The 3D neuromorphic sensing system was constructed by an electrochemical sensor, a 3D oscillator, and a synaptic transistor to replicate the whole signal processing procedure in the biological system, including sensing, signal transmission, and signal processing.

The 3D oscillator was utilized for signal transmission, which was designed based on simulation results and fabricated by different 3D printed methods. The individual components of the 3D oscillator were parametrically studied by comparing the simulated and experimental results. The inorganic synaptic transistor was fabricated by the DIW approach. The mechanism of the synaptic transistor was explored by realizing the nonvolatile effect. Then, a 3D neuromorphic electrochemical sensing system was integrated gradually through certificating the fabricated electrochemical sensor, 3D oscillator, and synaptic transistor step by step. The learning and memory of the 3D neuromorphic system was also discussed and finally utilized to detect low ion concentration in artificial soil.

The chapter includes sections derived from the journal paper: **C. Bao, S. K. Seol, and W. S. Kim. *A 3D integrated neuromorphic chemical sensing system*. Sensors and Actuators B: Chemical 332 (2021) 129527. Note: Used with permission from Elsevier.**

4.1. Abstract

Neuromorphic systems are essential for next-generation neuro-robotics and neuro-prosthetics with biological signal processing and memory functions. In this work, we propose a 3D integrated neuromorphic system for chemical sensing with 3D printed components, including a sensor, an electrical oscillator, and a synaptic transistor, which mimic sensory receptors, neurons, and synapses in biological systems, respectively. The 3D neuromorphic system was fabricated by 3D printing of multiple materials, resulting in

significant improvements in the volumetric efficiency of the system. Through this system, different ion concentrations are detected, self-activated, and transmitted. Finally, the electrochemical neuromorphic sensing function is demonstrated by the integrated 3D neuromorphic system with artificial sensory receptors, artificial neurons, and artificial synapses for application in the detection of low concentrations of soil nutrients in smart farms.

4.2. Introduction

Current wearable systems with flexible electronics have attracted significant attention for real-time monitoring applications in the past decades.[129–131] The demonstrated systems are usually composed of two-dimensional or planar components. To adapt to uneven surfaces, individual components of 2D electronics and connecting traces usually require adaptability and flexibility, which is a challenge for the implementation of advanced wearable systems.[132,133] Therefore, emerging systems with 3D integrated electronics have been considered owing to fewer requirements for flexibility in their individual components and conductive traces.[134,135] Likewise, 3D structural designs ease the interconnection of planar flexible circuits. As the next generation of humanoid robots or prosthetics requires mimicking multiple sensing abilities, 3D neuromorphic systems with such functions are demonstrated as artificial sensory systems. The 3D integration of sensor, processor, and actuator parts by in situ embedding was realized without considering the deformation of devices and achieved with high volumetric efficiency.[135] Thus, integrated 3D neuromorphic systems have a great potential to be applied as neuro-robotics and neuro-prosthetics to emulate the functions of human body organs.

3D printing is a promising fabrication method to implement 3D integrated neuromorphic systems because of its adaptive customization and specific tailoring capability. This method has been significantly innovated in the electronics field, particularly for 3D shaped components, including 3D sensors[60] and passive and active 3D electronic components.[136,137] Furthermore, 3D integrated circuits composed of commercial electronics have also been provided by this fabrication method.[134,135] For instance, by pre-fabricating channels or embedding conductive traces, an integrated circuit is realized on a 3D cube with improved volumetric efficiency by NASA’s Johnson Space Center.[134,135,138,139] However, although 3D shaped structural electronics have been studied by the 3D printing method, a fully additive manufactured 3D integrated circuit has not been achieved yet, including 3D artificial neuromorphic systems.

The emergence of bio-inspired neuromorphic systems is primarily attributed to the development of the Internet of things and powerful computational capabilities, such as deep learning. However, current von Neumann-based processors face the limitation of low speed and high energy consumption because data are separately stored and processed in sequence.[140,141] Furthermore, Moore's law also restricts the minimization of transistors on chips to satisfy the energy and area efficiency. Thus, bio-inspired neuromorphic algorithms and systems have been developed based on intrinsic features of parallel and analog processing and memory, mainly the learning function.[24]

To obtain the bio-inspired memory and learning function, artificial synapses have been invented to surmount the restraints of the von Neumann bottleneck and Moor's law.[13,41] In addition, biological functions have been achieved by regulating the conductivity of artificial synapses.[41] By scaling up artificial synapse technologies, neuromorphic systems framed with multi-artificial synapses have been successfully implemented for pattern perception by 2T memristor arrays[142] and 3T synaptic transistor arrays.[18,143] A more complicated memristive neuromorphic circuit has been utilized to navigate a Braitenberg vehicle.[144]

Furthermore, to emulate the sensing capabilities of the human body, spiking neuromorphic systems integrated with sensory receptors provide bio-inspired sensing functions to emulate visual[145,146] and tactile perception sensing.[147] For instance, a neuromorphic system with a photodetector and an artificial synapse transistor has been demonstrated to activate the movement of an artificial muscle under light pulses as biological spikes.[55] However, the reported neuromorphic systems is self-activated without artificial spikes because sensory signals from receptors are usually in electrical direct current (DC) format. In contrast, in spike-based biological systems, sensory information is converted into spikes, which enable the information processing and learning function in synapses. Therefore, an auxiliary spike generator that converts detected DC signals to pulse-type alternating current (AC) signals should be integrated between the sensory receptor and the synapse to form a self-activating bio-inspired neuromorphic system. Thus, few studies have been performed on such neuromorphic systems that completely emulate biological functions, including sensing, signal conversion, and signal transmission. For instance, a biomimetic somatosensory system established with a tactile receptor, a neuron, and an artificial synapse has been utilized to identify target movement and braille letters.[54] Owing to the low energy consumption and high response speed, neuromorphic systems with full bio-inspired functions are implemented to emulate biological organs, such as skin, nose, tongue, ear, and eyes, which respond to environmental stimuli, providing the basic human senses of touch, smell, taste, audit, and vision, respectively. Specifically, the emulation of the physical nose and tongue by neuromorphic chemical systems is applied to monitor external chemical information in the environment, such as pH value or heavy ion concentration in water or soil, which is crucial for food safety and the agricultural industry.[148] However, very few self-activating neuromorphic chemical systems have been reported to date.

In this work, a 3D integrated neuromorphic chemical system is proposed, as depicted in Figure 4.1. Three crucial components, including an ion-selective electrode (ISE), an electrical oscillator, and a synaptic transistor, were built together as a system for an artificial receptor, an artificial neuron, and an artificial synapse for sensing, signal conversion/transmission, and signal processing, respectively. The artificial receptor is activated by environmental stimuli, followed by converting the detected signal to an oscillated signal through the artificial neuron and then transmitted to a potentiated signal by the artificial synapse. Finally, through such three steps, the biological sensing function, including signal conversion and transmission between neurons, is fully emulated by the demonstrated neuromorphic chemical system. The proposed 3D neuromorphic system was built as an integrated 3D structural electronics by the 3D printing method in an embedded set-up, allowing ease of design flexibility and customized functions. In the demonstration, a low concentration of potassium ions from soil was monitored by the training method of the proposed 3D neuromorphic system.

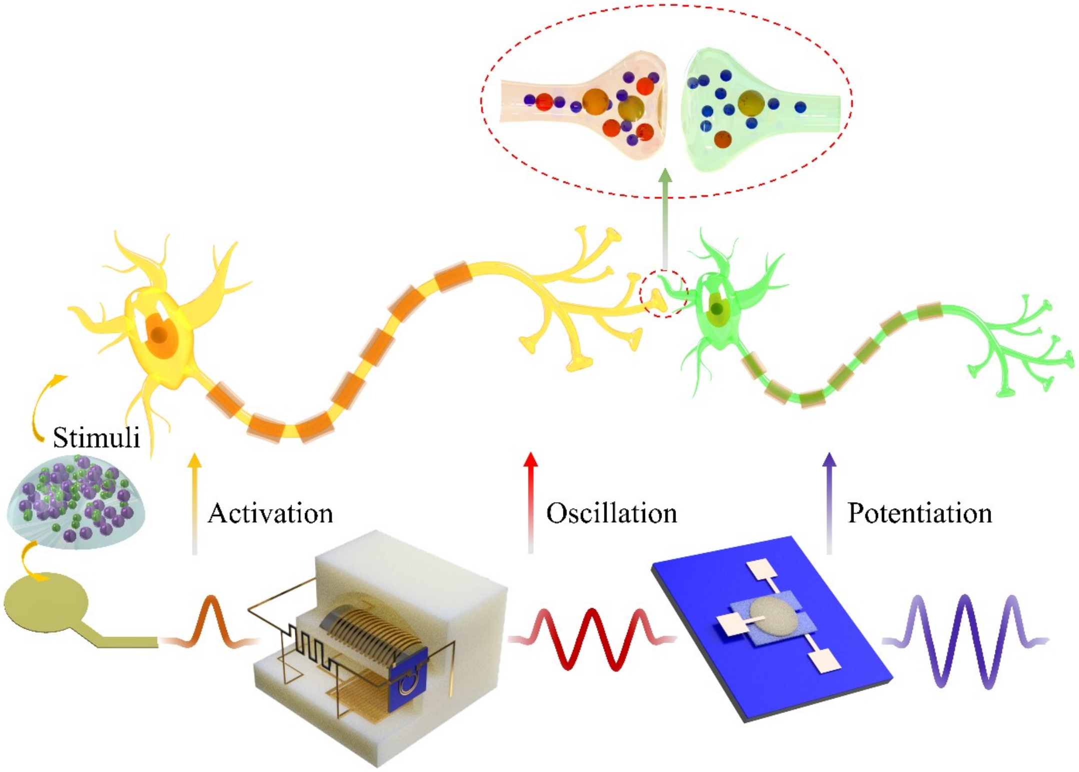

Figure 4.1. Schematics of the 3D integrated neuromorphic system for chemical sensing. The neuromorphic systems contain an ion-selective electrode, electrical oscillator, and synaptic transistor for mimicking biological receptors, neurons, and synapses, respectively.

4.3. Fabrication and Characterization

4.3.1. Fabrication

3D Printable materials

The printable magnetic material for the inductor core was prepared by mixing 2 g urethane triacrylate (oligomer), 0.5 methacrylic acid (monomer), 0.08 g 2,2'- azobis (2-methylpropionitrile) (AIBN) (radical initiator), and 0.08 g Luperox® A75 Benzoyl peroxide (thermal initiator) from Sigma-Aldrich as a matrix material by a SpeedMixer (DAC 150.1 FVZ-K, FlackTek, Inc.). In sequence, it was mixed with magnetic Mn-ferrite powder with a diameter of 1-10 μm (Powdertech International Corp.). The silver paste was prepared by mixing 40 wt% silver flakes (Inframat® Advanced Materials LLC, USA) with the mentioned matrix material. The electrolyte on the synaptic transistor gate was prepared by mixing 0.16 g of Poly (ethylene oxide) (PEO) and 0.02 g of $LiClO_4$ in 1.8 mL acetonitrile. The ISE membrane solution was prepared by dissolving 65.6 mg Poly (vinyl chloride) (PVC), 129.4 mg dioctyl sebacate (DOS), 4 mg valinomycin, and 1 mg potassium tetrakis (4-chlorophenyl) borate (KTpClPB) (KTpC1PB) into 2 ml Tetrahydrofuran (THF). Two types of K^+ analytes were prepared. For the system evaluation, KCl was dissolved in DI water to obtain a series of solutions with different concentrations, while commercial fertilizer with a nitrogen/phosphorous/potassium (NPK) ratio of 6-20-20 was prepared for neuromorphic system applications.

3D Integrated device

3D shaped substrates were printed by an Ultimaker-3 Extended (Ultimaker, Netherlands) with transparent nylon. Then, 3D inductors, capacitors, and resistors were prepared through a nozzle with 300 μm in diameter, embedded, and printed on the surface of a 3D nylon cuboid using a 3D DIW system (SHOT mini 100Sx and ML-808GX, Musashi Engineering, Inc.) to form electrical oscillators. After printing on nylon substrates, the printed inductors, capacitors, and resistors were built together. The curing temperature was 120 °C for the conductive traces and 150 °C for magnetic cores and resistors. ISE electrodes and synaptic transistors were also fabricated by 3D DIW systems (V-One printer, Voltera, Canada) and SHOT mini 100Sx and ML-808GX (Musashi Engineering, Inc.), respectively. After curing, 60 μl K^+-ISE solution was used to cover the WE of ISE by the drop-casting method, while 10 μl electrolyte solution was dropped on the channel area between the source and drain electrode of synaptic transistors. Then, the coated samples were placed in a fume hood overnight. Finally, the fabricated oscillators, ISEs, and synaptic transistors were connected by 3D printed conductors for the completion of 3D integrated neuromorphic systems.

4.3.2. Characterization of devices

The fabricated inductors and capacitors were characterized with a 4980A precision LCR meter (Agilent Technologies, USA), while resistors were tested by a source meter Keithley 2400 (Keithley Instruments, USA). The resonant frequency of the integrated LC was evaluated with a ZND vector network analyzer (Rohde & Schwarz, Germany). The oscillation properties of the fabricated Colpitts oscillators were confirmed by an oscilloscope SDS1000DL (SIGLENT Technologies America, Inc., Ohio, America). The OCP of ISE was recorded using a potentiostat (CHI1205B, CH Instruments, Inc., USA) with a 0.1 s interval. The electrical performance of synaptic transistors and neuromorphic systems was evaluated using a probe station with a semiconductor parameter analyzer (4200-SCS, Keithley, USA).

4.4. Results and Discussion

4.4.1. Fabrication of Embedded Electrical Oscillators by 3D Printing Method

As a chemical sensing platform, ISE was chosen and printed as an artificial receptor based on the electrochemical sensing mechanism described in previous work.[149] Two electrodes, a working electrode (WE) and a reference electrode (RE), were built on the ZTO semiconductor layer above a silicon wafer by the direct writing printing method for a 3D printed ISE. Owing to the selective character of the ion-selective membrane on the WE, the potential created between WE and RE was influenced by the ion concentration in the analytes, which could be supplied as a triggered signal from environmental chemical stimuli for the neuromorphic system, namely activation. Usually, the signals in a biological system are transmitted in the form of spikes, which are critical for signal processing and memory/learning functions. However, the ion concentration detected by the ISE is a DC signal. Thus, to emulate the signal transmission process in the artificial neuromorphic system, the DC signals (open circuit potential (OCP)) from the ion concentration should be converted to AC form as artificial spikes for the learning and memory functions by spike plasticity.[3,150,151] Therefore, an electrical oscillator was prepared to connect with the ISE, as shown in Figure 4.1. The activation produced by environmental stimuli through the ISE is converted to an AC signal by the 3D shaped oscillator, namely oscillation.

The electrical oscillator in this study is composed of 3D printed electronic components, including interdigitated capacitors, inductors, and resistors, as shown in Figure 4.2a. Although components with planar structures can be massively fabricated by printing methods on flexible substrates for wearable devices, planar electronics face the limitation of tuning their properties to obtain desirable performance. Thus, 3D printed electronics overcome such a shortage by expanding property-tuning opportunities. 3D inductors have already been demonstrated with self-sustained 3D conductive structures by the 3D printing method.[136] However, the dimensions of the inductors cannot be expanded because the 3D structure is supported by the uncured material, restricting the inductance in the range of the nano-Henry scale. Thus, in our design, an inserted shape-compatible magnetic core for the proposed inductors provides extra support for the semi-circular structure, which increases the possibility of fabricating inductors to a large size. It is expected that 3D inductors with magnetic cores result in a higher inductance value.

For 3D printed inductors, the theoretical inductance of solenoidal inductors is calculated using Equation 4.1[152]:

$$L = \eta \frac{\mu {N_L}^2 \pi r^2}{l} \qquad \text{(Eq. 4.1)}$$

where μ is the permeability, N_L is the number of turns, r is the radius, l is the length, and η is the ratio of $l\,/\,r$. Thus, the inductance is proportional to the permeability and the square of the number of turns. Therefore, a well-known method to improve inductance is to insert a magnetic core with high permeability inside a solenoidal inductor. As a common magnetic core material, ferrite is exclusively used for the preparation of printable magnetic paste.[153,154] Ideally, the higher the ferrite concentration in the paste, the better. In this study, Mn-ferrite was adopted as the magnetic core material. The relation between permeability and inductance was simulated, as shown in Figure 4.2b. A linear relation was obtained when the relative permeability was below 20, while saturation was reached when the magnetic permeability was approximately 60. Thus, the effort to improve the magnetic properties of the inductor core should be switched to enhance other parameters of the core materials. In addition to enhancing the magnetic properties of inductors, magnetic cores are also used to support the conductive traces structurally. The direct contact between written coils and the magnetic core eliminates the wall between them, maximizing the enhancement of magnetic properties, which is impractical for 3D printed inductors filled with ferrofluids.[155] To fabricate a 3D magnetic core as a designed structure, we investigated the printability of the magnetic paste with a high concentration of Mn-ferrites. As shown in Figure A4, only a small weight percentage window, specifically a paste with 82.5 wt% Mn-ferrite, shows suitable printability and shape-maintaining ability to print a designed core shape. The fabricated procedure for 3D shaped inductors is illustrated in Figure A5, where the bottom conductive traces are extruded on a substrate, followed by printing a 3D shaped magnetic core above. The top conductive traces are extruded on top of the fabricated magnetic core to connect with the bottom traces. Finally, with the optimized weight percentage of Mn-ferrite, a 3D inductor with a radius of 5 mm and a pitch of 1 mm was successfully obtained.

As shown in Equation 4.1, the inductance increases with the square of the turns of the wire for solenoid inductors. However, with the current 3D printing method, 3D inductors are fabricated on flat substrates by following the order: bottom conductive traces, 3D shaped magnetic core, and top conductive traces. Thus, the cross-section of the fabricated inductors is semi-cylindrical, which is different from that of the solenoid inductors. To verify the circular inductance equation for the proposed semi-circle inductors, a series of inductors with different numbers of coils were tested and simulated. The inductance change depending on the turns of the wire was in accordance with the simulation result, in which the inductance increases with the number of coils, as shown in Figure 4.2c. Both simulation and experiment provide a minimum value at 5 turns, with an inductance of 144 nH and 177 nH, respectively. The inductance increases with the number of turns.

To design 3D printed capacitors, a capacitor with interdigitated electrodes (IDEs) was considered. The total capacitance of the IDEs is calculated by Equation 4.2[156]:

$$C = (N_c - 3)\frac{C_I}{2} + 2\frac{C_I C_E}{C_I + C_E}, \qquad N_c > 3 \qquad \text{(Eq.4.2)}$$

where N_c is the number of IDEs, and C_I and C_E are the capacitance between the internal electrode and outer capacitance relative to the ground, respectively.

For an individual capacitor, the capacitance is calculated by Equation 4.3[157]:

$$C = \varepsilon_r \frac{A}{4\pi d} \qquad \text{(Eq.4.3)}$$

where ε_r is the relative static permittivity, A is the overlap area of the two plates, and d is the separation between the plate. Equation 4.2 indicates that the capacitance increases with the increase in IDEs numbers. Both simulation and experimental results supported this theory, as shown in Figure 4.2d. Both Figure 4.2c and Figure 4.2d indicate a certain divergence between the simulation and experimental results where it may come from the shape difference between numerical models and printed shapes. The printed capacitors were designed with a period of 1 mm and a finger length of 10 mm. Among the three fabricated capacitors with different IDEs numbers, the largest capacitors for the virtual and printed models were obtained when the IDEs numbers were equal to 15, with 2.0 pF and 5.6 pF, respectively. Furthermore, as shown in Equation 4.3, the extra dielectric material, such as $BaTiO_3$, increases the capacitance with the same number of IDEs pairs owing to its larger permittivity than air.[158] The capacitance of 15 electrodes increased to 7.6 pF with $BaTiO_3$. For the design of the 3D printed resistor, the resistance is adjusted by controlling the thickness and length of the prints. A 1 kΩ resistor is obtained when the length is 40 mm with a thickness of 0.2 mm. To verify the printed capacitors and inductors, an inductive-capacitive (LC) resonator was constructed with a 3D inductor and a capacitor, as shown in Figure 4.2e. The resonant frequency of the fabricated resonator is located at 2.36 GHz, which is close to the simulation result of 2.26 GHz by Maxwell-ANSYS, with the simulation model shown in Figure A6. The resonant frequency discrepancy between the simulation and characterization may be a result of the non-ideal shape of the fabricated samples accompanying the environmental noise.

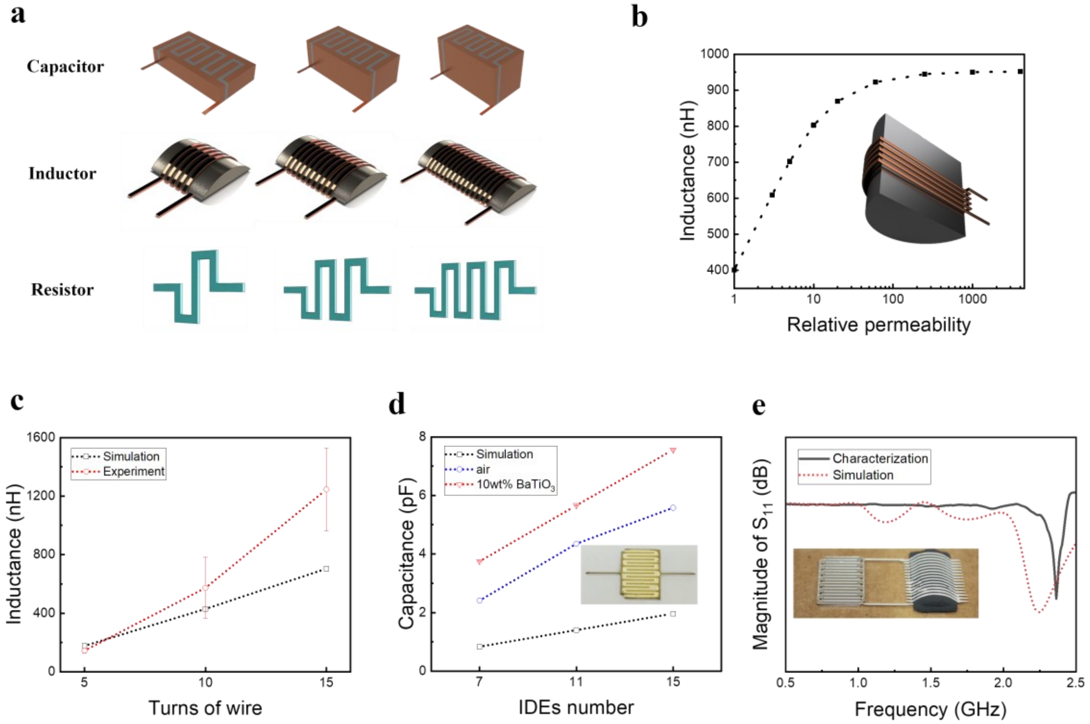

Figure 4.2. **Additively fabricated 3D printed components. (a) Schematics of capacitor, inductor, and resistor. (b) Simulation between inductance and relative permeability of magnetic core material for 3D shaped inductors. (c) Inductance comparison between simulation and experimental results for 3D shaped inductors with different wire turns. (d) Capacitance change with different IDE numbers without $BaTiO_3$ and with 10 wt% $BaTiO_3$ for 3D shaped capacitors (Inset: IDE capacitor with 15 electrodes, the white filling material is $BaTiO_3$). (e) LC circuit's resonance comparison between simulation and experiment (Inset: LC resonator fabricated on glass slides with a 15-electrodes capacitor and a 15-turns inductor).**

To provide self-activating spikes for artificial synapses, an oscillator was created to convert the signal perceived by ISEs. Oscillators are classified into inductor/capacitor (LC), resistor/capacitor (RC), and crystal oscillators.[159] Owing to the character of low phase noise, two basic types of LC oscillators have been derived, including Hartley and Colpitts oscillators.[136,160] The Colpitts oscillator was chosen in this study because it has more frequency stability compared to Hartley oscillators. The equivalent circuit was designed using LTspice software, as shown in Figure 4.3a, where the capacitance, inductance, and resistance were 6 pF, 1.4 μH, and 2.2 kΩ for three 3D printed components, respectively, while the transistor was alternated by a commercial transistor spice model (2N3904). Figure 4.3b depicts a 3D oscillator based on the designed equivalent circuit, where all electronic components are embedded in a 3D cuboid. The nylon cuboid was fabricated as a substrate for the oscillator circuit by the fused filament fabrication (FFF) method. All passive components, including resistors, inductors, and capacitors, were fabricated onto the printed cuboid by the direct-ink-writing (DIW) method. As shown in Figure 4.3c, the bottom pattern constructed with capacitors (i) was firstly fabricated on the printed square substrate, followed by the middle layer of inductors (ii) and top resistors (iii). Finally, by connecting all components with conductive traces through the DIW method, an embedded LC Colpitts oscillator was obtained, as shown in Figure 4.3d. For comparison, a facial oscillator was designed and fabricated by the 3D printing method, with all components located on the surfaces of the nylon cube, as shown in Figure A7. Figure A8 indicates that a larger volumetric efficiency was achieved for the embedded oscillator because the height was decreased from 30 to 20 mm. The theoretical output from the equivalent oscillator was an AC signal with a frequency of 24 MHz, as shown in Figure 4.3e. The measured result was observed from the fabricated 3D shaped oscillator with a frequency of 28 MHz, as shown in Figure 4.3f. With such oscillator, the detected DC signal by the artificial receptor-ISE was successfully converted to an AC signal, used to mimic the nerve impulses transported between neurons to achieve learning and memory functions.

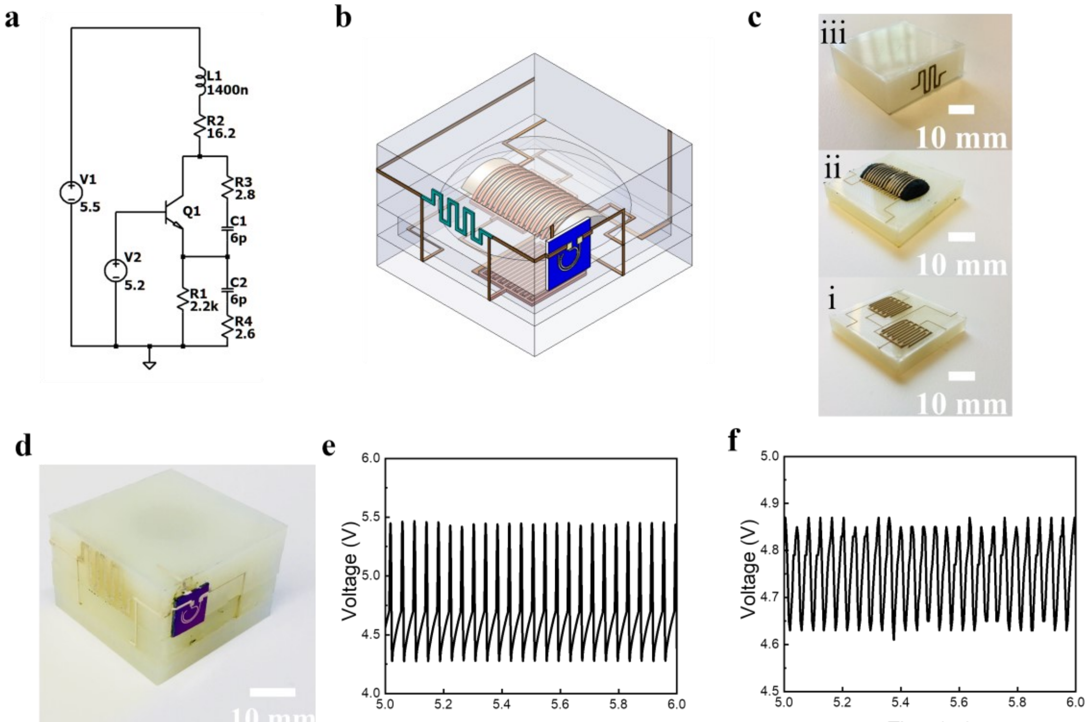

Figure 4.3. **Characterization of a 3D integrated electrical oscillator. (a) Equivalent circuit of Colpitts oscillator. (b) Schematic of the 3D integrated electrical oscillator. (c) Fabrication procedure for the embedded oscillator. (d) Image of the printed 3D oscillator. (e) LTspice simulation of AC signal produced by Colpitts circuits. (f) Experimental output from the 3D shaped oscillator.**

4.4.2. Characterization of Synaptic Transistors

Emulation of sensing and signal conservation has been accomplished so far. The next step is to emulate intelligent behaviors similar to those of the physical system. Thus, artificial synapses have been proposed and studied. In previous studies, two-terminals (2T) memristors and three terminated transistors have been developed as artificial synapses to overcome the constraints of the von Neumann bottleneck and Moor's law.[13,41] 2T memristors with a sandwich structure which is constructed by a function layer placed between a top electrode and a bottom electrode exhibit the advantage of low power and analog computing compared with conventional complementary metal–oxide–semiconductors. Therefore, current neuromorphic processors are mainly formed by scaling up 2T memristors as a crossbar architecture.[24] However, 2T devices also have shortcomings such as separated biological memory and processing functions,[161,162] nonlinear switching properties, write noise, and high device conductance.[140] Therefore, 3T artificial synaptic transistors have recently gained considerable attention owing to their spatiotemporal memory/processing, and linear switching conductance. Additionally, several mechanisms have been proposed, including charge tunneling and trapping, ferroelectricity, ion migration, and electrochemical reactions.[41]

Ion migration induced electrical double-layer (EDL) is formed by ion accumulation at the interface between the semiconductor channel and the electrolyte gate under a bias, while electrochemical doping and de-doping are realized by ion exchange between the ions inside the electrolyte and the semiconductor material. Furthermore, EDL and electrochemical process mechanisms are affected together depending on the frequency[163] or relative bias amplitude.[164] Unlike the field effect transistor in ISFETs, synaptic transistors are designed with an ionic electrolyte gate. Figure 4.4a schematically illustrates the operation mechanism of the proposed synaptic transistor with $LiClO_4$ electrolyte, including four stages. In the original state (stage i) without bias on the transistor gate, Li ions are uniformly distributed inside the electrolyte. When a positive bias is applied to the transistor gate, positive Li-ions accumulate at the interface between the electrolyte and channel to form an EDL (stage ii). With the increase of Li^+ ions due to sufficient bias duration or amplitude, Li^+ ions are doped inside the semiconductor channel, resulting in higher conductivity. When the gate bias is removed, the accumulated ions diffuse back to the electrolyte due to the high Li^+ ion concentration gradient at the EDL (stage iii). However, doped ions cannot be extracted from the channel. Thus, the conductivity is still larger than that of the original state due to the remaining ions even without a gate bias, namely the nonvolatile effect. With the nonvolatile effect, a negative bias should be applied to the gate to extract the doped ion back to the electrolyte to restore the original conductive state (stage iv). Thus, the conductivity of synaptic transistors is regulated by the applied pulses on the electrolyte gate, where Li^+ ions work as neurotransmitters in biological systems.

Based on the proposed processing mechanism, two prototypes of zinc-tin oxide (ZTO) - based synaptic transistors with the $LiClO_4$ electrolyte gate were demonstrated, as shown in Figure 4.4b and 4.4c. In Figure 4.4b, the 3D printed serpentine source and drain electrodes were fabricated on top of the ZTO layer by the DIW with silver paste, followed by covering with a dielectric material for the remaining area except the channel opening with a channel length of 100 μm. After the drop-casting electrolyte on the exposed channel area, a gate electrode was printed on top of the dried electrolyte surface. However, the prototype encountered difficulties in encapsulating the silver electrodes without covering the channel area. Therefore, a second prototype with a straight source and drain electrodes that are easily encapsulated with a thin dielectric layer was proposed. Finally, a printed synaptic transistor was demonstrated, as shown in Figure 4.4c, with a channel dimension of 0.4 × 2 mm. To verify the neuromorphic behavior of the $LiClO_4$ gated ZTO synaptic transistor, the potentiation based on the nonvolatile effect was demonstrated, as shown in Figure 4.4d. It is clearly illustrated that the amplitude of conductivity (A2) triggered by the second pulse is larger than the conductivity (A1) by the first pulse because of the remained ion inside the channel, with a ratio (A2/A1) of 2.5. As a result, the potentiation and depression were described in Figure 4.4e and Figure 4.4f. Figure 4.4e shows the increased amplitude of the current with a consecutive positive bias applied to the electrolyte gate. After 35 consecutive striking pulses, the amplitude of the current increased to 4.60×10^{-11} A. On the contrary, during the depression performance, 28 consecutive negative pulses applied on the electrolyte gate restored the amplitude of current to the original value as a refreshing approach for the synaptic channel after potentiation, as shown in Figure 4.4f. Compared with potentiation, fewer pairs of pulses are needed to restore the current to the original state due to the force formed by the doped and accumulated Li^+ ions at the EDL.

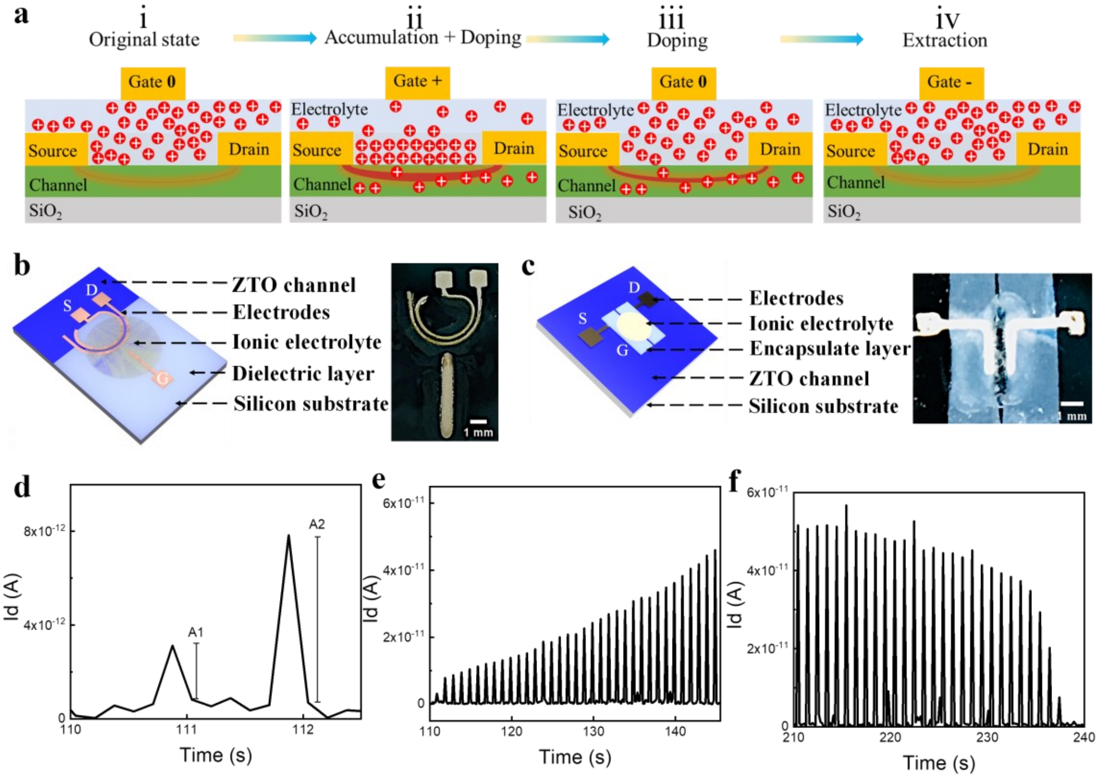

Figure 4.4. **3D Printed Synaptic Transistor. (a) Proposed mechanism of synaptic transistors with four stages. (b) Synaptic transistor prototype #1. (c) Optimized synaptic transistor prototype #2. (d) Nonvolatile effect. (e) and (f) Potentiation and depression performance of the synaptic transistor, respectively.**

4.4.3. Chemical Sensing by Integrated Neuromorphic Systems

Finally, a 3D integrated neuromorphic system was demonstrated, as shown in Figure 4.5a. The neuromorphic system includes a sensor, a 3D electrical oscillator, and a synaptic transistor that act in sensing, signal conversion/transmission, and signal processing, respectively. ISE sensors are used to monitor the ion concentration in the environment, which is represented as OCP. Then, such an ion concentration-related DC signal is converted to an AC signal as artificial spikes by a connected 3D electrical oscillator. Finally, concentration-linked spikes are applied to the electrolyte of the synaptic transistor, and chemical information is reflected as the conductivity fluctuation. Thus, the procedure is gradually confirmed to describe the proposed signal processing in the 3D integrated neuromorphic system. First, K^+-ISE was selected for monitoring the K^+ ion concentration inside the soil sample. Figure 4.5b shows that the OCP increases with the K^+ ion concentration in the range of 10^{-4} to 1 M. A linear relationship between the average

OCP and K^+ ion concentration was also obtained, as shown in Figure A9a. Figure 4.5c shows the performance of the demonstrated oscillator when applied with different ion-concentration-related OCPs. This indicates that the amplitude of the output AC signal and the average baseline is modulated by different K^+ ion concentrations. A linear relationship between the average baseline and the K^+ ion concentration was also achieved as well as amplitude as shown in Figure A9b and Figure A9c, in the range of 10^{-4} to 1 M. Finally, the obtained ion concentration-related spikes were applied to the electrolyte gate as an artificial gate. The conductivity fluctuation with time under different ion concentrations was monitored, as shown in Figure 4.5d. A linear relationship between ion concentration and conductivity was obtained, as shown in Figure 4.5e. The largest conductivity (1.46×10^{-10} A) was obtained under 1 M K^+ solution, while the minimum was 9.18×10^{-11} A for a 10^{-4} M solution. This shows that the conductivity of the synaptic transistor is also modulated by different ion concentrations. Thus, the signal processing procedure through the proposed neuromorphic system has been verified, providing sensing, signal conversion /transmission, and signal processing functions. In the neuromorphic research community, the training method is carried out to modulate the synaptic weight of synaptic transistors for signal processing. The training state can be maintained for later signal processing due to the nonvolatile effect. To realize the biological learning behavior, a further step has been studied by comparing the conductivity before and after training, as shown in Figure 4.5f. Based on the result that a solution with a higher ion concentration resulted in a larger conductivity with a sensitivity of 1.34×10^{-11} A/decade, as shown in Figure 4.5e, a 10^{-4} M solution was chosen as the control sample, while a 1 M solution was used as the training solution to observe the nonvolatile effect. The conductivity of the control solution pre-training was 1.2×10^{-10} A. After training with a 1 M K^+ solution, the conductivity of the control solution increased to 2.8×10^{-10} A owing to the nonvolatile effect. 10 min later, the conductivity decreased to 1.9×10^{-10}, which is still higher than the initial state 1.2×10^{-10} A. Approximately 20 min later, the synaptic transistor returned to the original state, which indicates that the nonvolatile effect lasts for about 20 min. Accordingly, memory behavior has been verified through the observation of the nonvolatile effect.

The 3D neuromorphic system's learning concept was further investigated for ion concentration monitoring in smart agricultural applications. Figure 4.5g schematically shows the procedure for soil sample extraction under plants, which includes extraction, filtering, and dissolving processes.[165] A theoretical 10^{-4} M K^+ solution was prepared using fertilizer for the simplified processes. However, it is anticipated that an actual K^+ ion concentration is considerably lower than 10^{-4} M because of the non-exchangeable K^+ ions in the fertilizer.[166] The learning capability of the proposed neuromorphic system was performed to monitor such a low-concentration solution. Figure 4.5h shows the experimental results obtained by the training method, where the dashed line is the threshold. Before training, the conductivity in the low-concentration solution was smaller than the threshold line. Then, during the training process with a 1 M K^+ ion solution, the conductivity was higher than the threshold value. After training, the conductivity under the same low-concentration solution significantly increased to more than the threshold value because of the memory effect, as mentioned before. Through such a training method, an increased conductivity with a low-concentration solution was obtained based on the nonvolatile effect. Thus, the demonstrated training method was applied to increase the limit of detection (LOD) for ion concentration monitoring inside the soil. The concentration of solution involved here is 10^{-4} M, which is already close to the LOD 10 ppm (10^{-5} M) by most standard soil chloride approaches.[165] Moreover, the conductivity achieved with a low concentration solution is comparable to the conductivity with a high concentration solution. This means that less material consumption is needed to obtain a certain output threshold compared to the situation without training. Thus, the learning function of the integrated 3D system was verified by the training method.

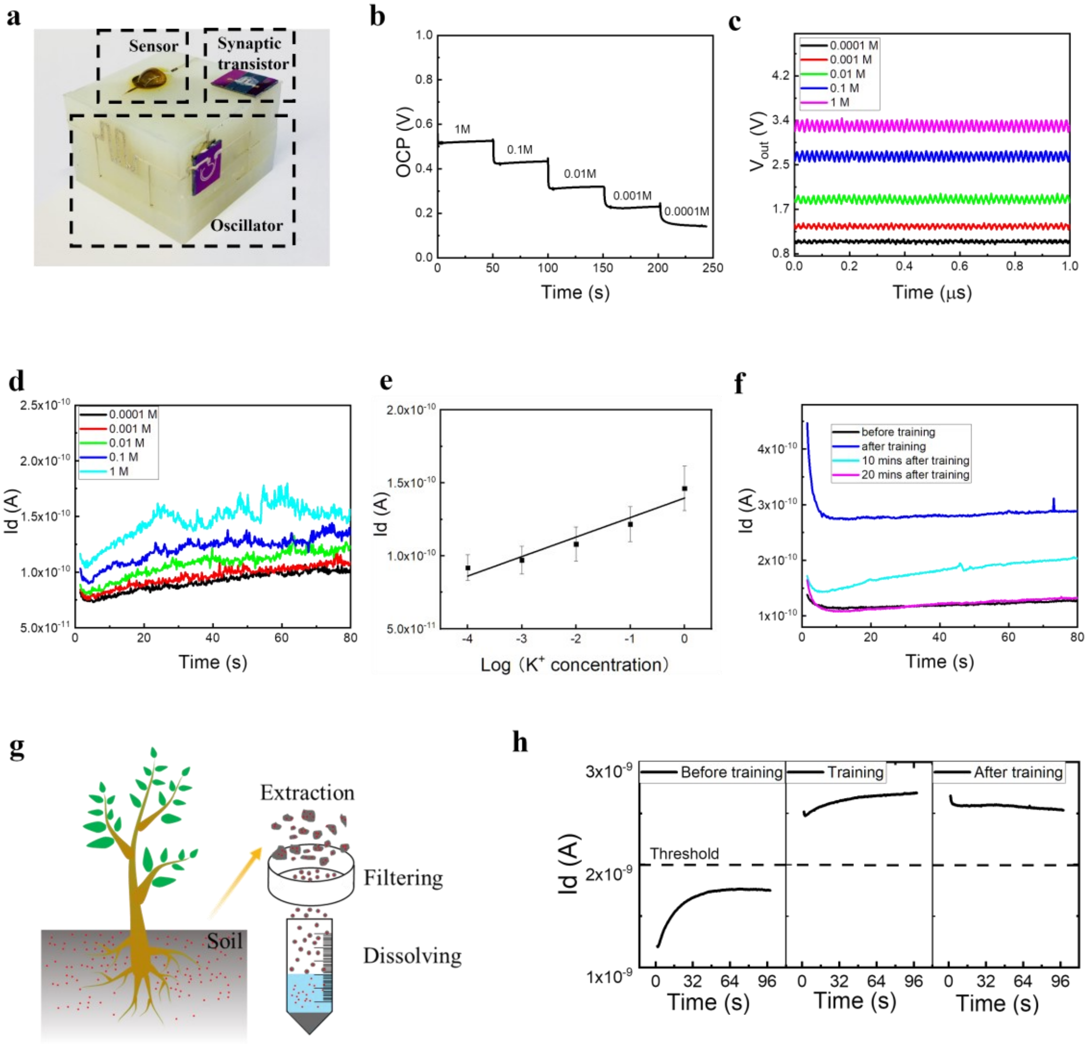

Figure 4.5. **Neuromorphic performance of 3D integrated ion sensing system. (a) Actual image of the 3D integrated neuromorphic system. (b) Performance of ISE. (c) AC signal output from the integrated ISE and electrical oscillator. (d) Performance of the 3D integrated neuromorphic system for sensing various K^+ ion concentrations. (e) Normalization of output from the fabricated 3D integrated neuromorphic system. (f) Conductivity monitoring for the 3D neuromorphic system, including the conductivity of pre-training, 10 min, 15 min, and 20 min after training. (g) Schematics of the soil extraction process. (h) Comparison of the output before and after training by the 3D integrated neuromorphic system.**

4.5. Conclusion

In summary, we have experimentally verified the feasibility of a 3D integrated neuromorphic system by the 3D printing method with 3D inductors, capacitors, and resistors. The proposed neuromorphic system has integrated functions of sensing, signal conversion/transmission, and signal processing. To realize signal conversion, LC Colpitts oscillators with 3D components were designed and embedded inside and on the surface of a 3D printed cuboid using the DIW approach. The frequency of the fabricated electrical oscillator was 28 MHz, similar to the theoretical simulation result of 24 MHz. Reliable signal transmission with the synaptic transistor was achieved based on the Li^+ ion accumulation and doping/de-doping mechanism. Two basic behaviors, potentiation and depression, were observed in the fabricated synaptic transistors. Finally, the ion-selective electrode was introduced as a sensor and integrated with the fabricated oscillator and synaptic transistors to complete an electrochemical neuromorphic system.

The signal from various chemical inputs through the 3D integrated neuromorphic system was gradually confirmed on the 3D integrated system. First, chemical information was detected by a 3D ISE, which showed a linear relationship with the ion concentration in soil. Then, the sensing information was transmitted through the electrical oscillator, resulting in an AC signal that also showed a linear response between ion concentration and its amplitude. Finally, the processed AC spikes autonomously triggered the integrated synaptic transistor. Through signal monitoring and assessment, the memory feature of the integrated 3D neuromorphic system was confirmed as the memory period of approximately 20 min. With such a memory capability, the fabricated neuromorphic system was utilized to detect a solution with low concentration by the training method. Such a method provides the advantage of lowering LOD and saving materials, which expands the application of online nutrient monitoring in smart agriculture applications. Moreover, the developed 3D neuromorphic system is extended for other sensing functions by alternating with diverse sensory receptors. And the spatial and temporal signal transmission feature are fully gained by intensifying artificial transistors.

Chapter 5.

Multi-axis Robot 3D Printed Neuromorphic Humanoid Hand for Grasping Unknown Objects

This chapter presents a novel multi-axis robot printing system that is constructed as an alternative to the current DIW printing method. The described system was utilized to fabricate electronics with vertical walls and tilted surfaces. An infrared (IR) laser was also carried out to sintering the printed conductive traces. A potentiometer-based tactile sensor was designed as the fingertips of a humanoid hand, and the performance was also characterized. A 3D neuromorphic tactile sensing system with reflex arc based on tactile sensing information is also discussed. A portable neuromorphic system was designed with pluggable features and fabricated by various 3D printed approaches. Then, it mounted on the humanoid hand. The touch sense as human beings were replicated through the tactile sensor. A full bio-inspired signal perception function was realized by transmitting the detected signal through the tactile sensor to the neuromorphic system, followed by processing by the artificial synapse. Also, a bio-inspired reflex arc was demonstrated by using the neuromorphic humanoid hand to gripe objects with unconsciously increased force through training.

The chapter includes sections derived from a submitted manuscript: **C. Bao, T. -H. Kim, A. Hassanpoor Kalhori, and W. S. Kim.** ***Multi-axis Robot 3D Printed Neuromorphic Humanoid Hand for Grasping Unknown Objects*****.**

5.1. Abstract

We present a 3D neuromorphic humanoid hand designed for providing an artificial unconscious stimulus response, based on training. The humanoid hand system mimics the reflex arc for a quick and unconscious response by managing complex spatiotemporal information. The 3D structural humanoid hand is integrated with a portable neuromorphic device and 3D printed tactile sensor using a novel multi-axis robot 3D printing technology. The 3D neuromorphic robot hand provides bio-inspired signal perception together with the biomimetic reflex arc function of a neuromorphic humanoid hand, allowing it to hold an

unknown object with an automatically increased gripping force. The proposed system offers a new approach for realizing an unconscious response with an artificially intelligent robot.

5.2. Introduction

Neurons, including those comprising the peripheral nervous system and central nervous system, efficiently and quickly manage complicated environmental situations.[1] The received spatial and temporal information are parallelly operated on at an ultra-high speed of 10^{13} per second, and only one watt is required before decision-making.[7] This is owing to the unique parallel processing and memory functions of the approximately 10^{11} neurons in the brain.[2,3] Therefore, it is beneficial to mimic this fast mechanism using a signal-processing unit. Several studies have reported on such emulations. The first generation of emulations focused on developing brain-inspired algorithms with parallel calculations for simulations.[6] For example, similar to the advances in artificial intelligence, neuromorphic computing has achieved significant progress in recent decades. The second generation of emulation was demonstrated at the hardware level, i.e., by replicating the biological parallel calculation functions of the human brain.[6] Different state-of-the-art devices were developed for emulating parallel calculations, such as central processing units, graphics processing units, and tensor processing units.[10] However, the developed algorithms and hardware were entirely dependent on complementary metal-oxide-semiconductor transistors; accordingly, they still faced the high energy consumption concerns for the traditional von Neumann’s architecture and limitations of Moore’s law.[8,9] The third type of emulation comprised a brain-inspired novel non-volatile device called an artificial synapse for realizing "in-memory computing".[9,10] In these devices, artificial synapses executed computation and memory in the same area utilized for constructing bio-inspired neuromorphic systems.[11] The artificial synapse-constructed neuromorphic systems possessed many advantages, such as high energy efficiency,[12] time-saving,[10] and fewer components.[4] Owing to the aforementioned advantages, neuromorphic devices have been integrated with various sensors for diverse applications, such as a chemical sensing function demonstrated through electrochemical sensing neuromorphic systems.[167] In another example, learning and non-volatile memory functions were utilized to enhance the output signal level for an application for artificial soil detection. An ideal neuromorphic system not only demonstrates signal reception, but also controls artificial effectors (such as humanoid hands), e.g., by refining a control procedure.[6] In one study, an artificial afferent nerve with a pressure sensor was employed for the control of a cockroach leg.[54] Furthermore, a conscious response has been demonstrated using an artificial stimulus-response system, and the response time was reduced through training.[168] However, in biological systems, not all environmental stimuli are processed by the brain.[169] Instead, synapses between the neurons and spinal cord produce a faster unconscious response as a simple reflex arc, thereby reducing the brain's tasks. Therefore, providing a neuromorphic system with a reflex arc function requires further research, so as to simplify the procedure for the control of a robotic hand.

Artificial skin has been highlighted as a type of biomimetic touch sensor. Different force or tactile sensors have been proposed for the sensor parts, including capacitance-based and resistance-based sensors.[170] A force-sensitive resistor (FSR)-based sensor has commonly been used as a tactile sensor, owing to its low cost, small size, and high sensitivity to force.[171] However, the low accuracy of an FSR remains a disadvantage, as its sensing mechanism relies on a pressure/force-induced deformation.[172] For example, the active layer in the FSR is deformed depending on the applied force, and thus the active layer is exposed to potential plastic deformation.[173] Thus, there is a need for a force-sensitive resistor without deformation of the active layer. Utilizing the sensing mechanism of a potentiometer is a possible solution, as it shows a variable resistance change without physical deformation of the active layer by changing the length of the conducting path. However, there remains another challenge for a tactile sensor to be used as a potentiometer for changing the force direction. In particular, an axial force needs to be changed to a torque to calculate the variable resistance. Thus, 3D origami structures are promising candidates for rotational converters.[174,175] In particular, the Kresling origami, formed by a series of tessellated triangles, shows rotating characteristics when compressed.[176] In addition, its rotating behavior can be tuned by modifying the angular design of the tessellated triangle(s), allowing for customization of the force sensing.[176,177] Applying the origami structure to the tactile sensor allows for force conversion without requiring other components, such as gears or axial shifters. Indeed, employing such a structure simplifies the entire tactile sensing system for various applications.[178]

Owing to its advantages in regards to custom and facile fabrication, 3D printing has been widely adopted for prototyping. Thus, various 3D printing technologies have been developed, such as fused filament fabrication (FFF), digital projection lithography, direct ink writing (DIW), and selective laser sintering. Among these, the DIW method for paste printing has attracted significant attention for the preparation of functional materials.[60,61,136,179–181] DIW-printed structures are mainly dependent on the properties of the printed materials, whereas in situ sintering with a laser facilitates the fabrication of 3D structures. For example, freestanding structures have been achieved using laser-assisted methods.[62] Circuits made from copper have been demonstrated on a 3D surface using a laser-assisted DIW method.[182] However, 3D printing on curvilinear surfaces while keeping the nozzle vertical to the surface is difficult in the typical vertical printing by DIW, owing to the limited freedom of current three-axis DIW printers. One novel solution is to add more freedom of motion to the printers by using a multi-axis robot arm. Robot arms are widely used in the industry for more complex applications, such as welding for automobiles. Nonetheless, to the best of our knowledge, this work is the first DIW printing method with a six-axis industrial robot arm.

Here, we present a DIW approach using a multi-axis robot arm, as shown in Figure 5.1a. The six-axis robot arm enables the seamless fabrication of conductive traces on vertical and tilted surfaces in a single printing process. Moreover, the 3D printed conductor can be sintered in situ using an infrared laser (IR) laser with optimized parameters, as shown in Figure 5.1b. Unlike conventional three-axis 3D printing systems, the demonstrated six-axis robot 3D printing can fabricate 3D electronics on curvilinear surfaces. A sensory humanoid hand is integrated with origami fingers and unique origami tactile sensors. A portable neuromorphic system is added for bio-inspired signal transmission and processing. Finally, the 3D structural neuromorphic humanoid hand is trained to demonstrate a reflected arc function by gripping an object with an unconsciously increased force, based on the learning and non-volatile memory functions of the neuromorphic system.

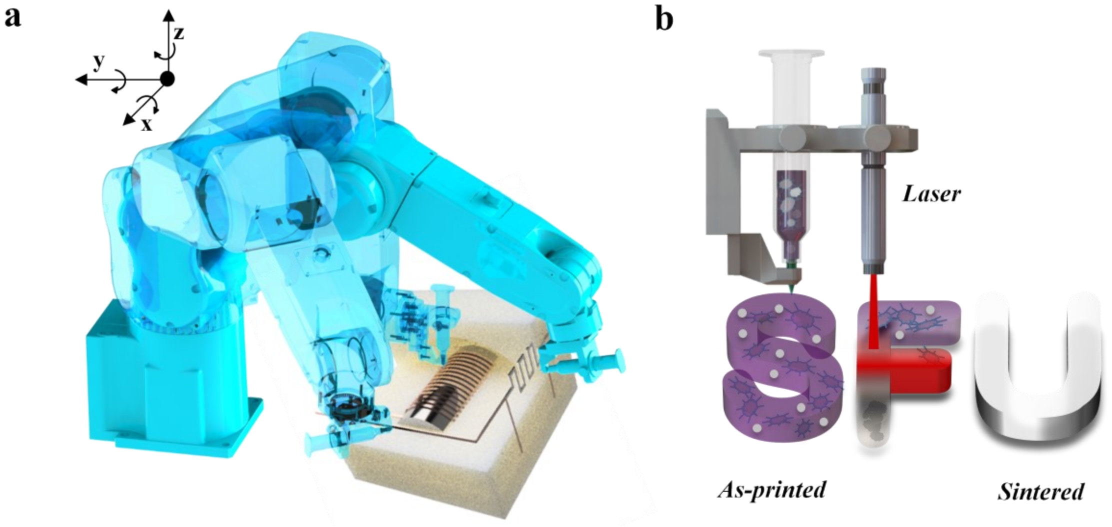

Figure 5.1. **Schematics of the six-axis robot 3D printing method. (a) Motion of robot 3D printing to different types of surfaces by the six-axis robot. (b) Schematics of printing procedure with in-situ laser sintering.**

5.3. Results

5.3.1. Robot 3D printing for structural electronics

Multi-axis robot arms are widely used in industries, as they are designed with several controllable freedoms. Therefore, integrating DIW printers with a six-axis robot arm is a promising solution for solving the shortage of current DIW printers that can vertically print features on planar surfaces. Meanwhile, an IR laser or UV light has been proven to be advantageous for paste-based DIW.[62] Therefore, an innovative laser-assisted six-axis robot printing system is illustrated in Figure 5.2a. The novel system comprises a six-axis robot, IR power control system, and DIW dispenser. A power control system constructed with an IR laser and function generator is used to manage the applied laser for sintering the printed conductive traces. The DIW nozzle and IR lasers are mounted on a printed head together, and are controlled by the robot. The IR laser sinters DIW-printed conductive traces. The bottom-left image Figure 5.2b shows the as-printed conductive traces, whereas the right-side image shows the fully sintered sample. The sintering level depends on the heat generated by the IR laser and is modulated by the function generator, including the pulse width and power. As shown in Figure 5.2c, the maximum temperature of the substrate increases with the pulse width at a fixed frequency and laser power. The temperature is 121.5 °C under a pulse width of 1 ms, whereas it increases to 174.4 °C under a pulse width of 2 ms. This is because a longer pulse width increases the duration of the laser spot on the sample, resulting in a higher temperature. However, the temperature must be lower than the temperature that the substrate materials can withstand. Accordingly, the exposure duration is also modulated by adjusting the speed of the robot motion. A higher robot speed reduces the duration of the laser spot on the printed sample, resulting in a slower sintering speed. Therefore, repeated sintering or rescanning is necessary for the complete sintering of the conductive paste. To examine the sintering effect, the resistance change of the printed line is monitored at a printing speed of 4 mm/s, as shown in Figure 5.2d. The resistance drastically decreases from 40 s onward, owing to the partial sintering. After 80 s, the printed line is fully sintered, because the resistivity has reached a stable value. The efficiency of the sintering is illustrated in Figure 5.2e, where it is expressed as the total duration time per millimeter. It is found that increasing the scanning speed improves the sintering efficiency.

The printing route of the DIW printing head is controlled by the six-axis robot arm. Owing to the six degrees of freedom, the robot system can be used to print on different types of surfaces. The right side of Figure 5.2f is a schematic of a 3D-shaped oscillator fabricated for the portable neuromorphic system. Conductive traces are designed on each vertical wall. In a conventional DIW printer, the vertical walls must be placed upward before further printing, followed by sintering. Repeating these procedures until the completion of printing all of the other walls requires energy. Seamless printing is not possible using a conventional DIW printer. However, the six-axis robot integrated with the same DIW controlling system is feasible for printing seamlessly in a single printing process while keeping the nozzle consistently vertical to the walls. Furthermore, tilted surfaces can also be fabricated by multi-axis robot printing, as shown in Figure 5.2g. The 3D Miura-ori origami finger has serpentine valleys on its surface.[183,184] Thus, a conventional 3D printing process on such architectured surfaces is challenging, even when printing a simple conductive path. However, the multi-axis robot printing process allows for the fabrication of a complex kirigami conductive path on the 3D origami finger. Moreover, kirigami patterns are well-known as stretchable structures against bending behaviors.[183] The robot fingers undergo repeated bending forces. Therefore, both the 3D origami fingers and kirigami conductive path provide strength for the repeated bending conditions. Indeed, the kirigami conductive path shows a synergic relationship with the 3D origami module, owing to the advantages of the multi-axis robot printing. The multi-axis robot printing system successfully fabricates the conductive traces. Through in situ laser sintering, the printed conductive traces on the vertical walls and tilted surfaces are seamlessly fabricated, as shown on the left sides of Figure 5.2f and 2g.

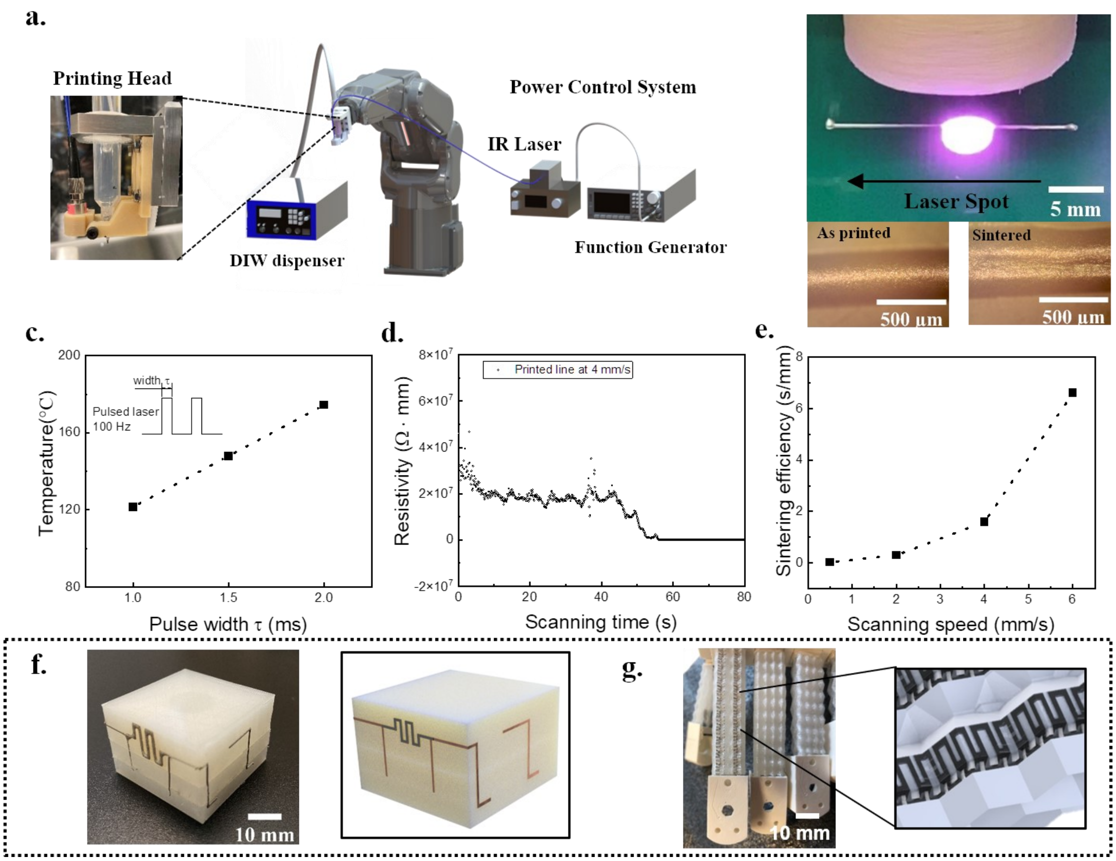

Figure 5.2. **Fabrication of conductive traces on complex surfaces. (a) Setup of the six-axis robot 3D printing. (b) Image of the laser spot and sintering (top: in-situ scanning; bottom left: as-printed conductive trace; bottom right: sintered conductive trace). (c) Relation between pulse width and induced temperature at a frequency of 100 Hz. (d) Resistance changes with scanning at a speed of 4 mm/s. (e) Relation between scanning speed and sintering efficiency. (f) Left: sample printed by six-axis robot on the vertical wall of a 3D shaped oscillator. Right: design of 3D shaped oscillator. (g) Left: the kirigami conductive path on a 3D origami finger using six-axis robot. Right: design of the kirigami conductive path on the tilted surfaces.**

5.3.2. Sensory humanoid hand with origami fingers and tactile sensors

The origami finger comprises an array of 3D Miura-ori structures for the humanoid robot hand. The 3D origami finger was optimized based on two different criteria: 1) maximum bending in one direction, and 2) minimized plasticity after large-cycle bending. A central composite design based on a statistical method was used for the optimization process.[184] The optimized finger frames were assembled as shown in Figure 5.3a. A tactile sensor with variable resistance is integrated on the fingertip. The Kresling origami was used as an active sensor frame, as shown in Figure 5.3b. The resistor length was changed between the 1st and 2nd paths, depending on the rotation degree of the origami structure.[177] The resistance of the conductive path changed linearly. When the 3D origami was compressed, the resistor length between 1st and 2nd paths gradually decreased, owing to the simultaneous rotation of the origami. Therefore, the resistance decreased, as shown in Figure 5.3c. In addition, the rotating feature of the 3D origami was tunable by changing the angular designs (α and β angles) of repeated triangles in the origami.[176,177] At different angles of β = 38–41°, a higher value of β shows a more rotatable behavior under compression, as shown in Figure 5.3d. Among other angular designs, the higher linearity of rotation under compression reflects the optimal design, as a larger rotating degree reflects a larger length change of the conductive path. Thus, the linearity of the rotated angle at different angular designs could be estimated using Equation 5.1.

$$Nonlinearity\ (\%) = D_{in(max)} / IN_{f.s.} \times 100 \qquad \text{(Eq. 5.1)}$$

In the above, $D_{in(max)}$ and $IN_{f.s.}$ are the maximum strain deviation and strain at the full scale, respectively. The nonlinearity values of the 3D origami with β = 38°, 39°, 40°, and 41° are 6.74 %, 6.42 %, 6.20 %, and 7.09 %, respectively. The angle of α is fixed at 30°. Among the range of the angle parameters, the 3D origami with β = 40° shows the lowest nonlinearity; thus, it was selected as the final design for the 3D origami sensor. Then, the conductive path (R: 3.8×10^3 Ω·m) was printed on the top of the inner wall of the 3D origami. The resistance changes at different compressions are shown in Figure 5.3e. When the 3D origami sensor was compressed, a change in the resistance was observed, as shown in Figure A10. The sensitivity of the 3D origami sensor was calculated using Equation 5.2, as follows:

$$Sensitivity = \Delta R_{max} / \Delta S_{max} \qquad \text{(Eq. 5.2)}$$

Here, ΔR_{max} is the resistance difference between the original and compressed states of the 3D origami, and ΔSmax indicates the maximum compressed length of the origami. The calculated sensitivity of the sensor is 53.13 Ω/mm. In addition, the gauge factor (GF), defined as GF = $|\Delta R/R_0|/\ \varepsilon$, was evaluated, where ε and ΔR are the strain of the sensor and changed resistance after compression, respectively. A GF of 2.5 was obtained from the 3D origami at a 35% strain. In some studies, the GF has been reported to be as large as 100.[185] However, the fabricated sensor represents a material-independent case for the active layer; therefore, it is expected that the GF of the sensor can be further improved once the proper materials are employed. After integrating the 3D origami sensor into the humanoid robot hand, we investigated the tactile sensing performance of the hand, as shown in Figure 5.3f. Before gripping, the highest resistance was observed, and once the robot hand started to grip a ball, the compressed 3D origami sensor on the fingertip caused the resistance to decrease drastically. The resistance changes before and after gripping are studied. Thus, we demonstrated a tactile sensing robot with a 3D origami sensor. In addition, the kirigami conductive path[183] on the origami finger was used to integrate the pressure sensing fingertip and multimeter, minimizing the wire integration. Thus, we secured additional space for additional functionalities with the tactile sensing performance of the robot, and potential problems (such as disconnection between the sensors and processor) were prevented during the bending of the finger; this was attributed to the six-axis robot DIW printing on the complex origami surface of the finger. Thus, a sensory humanoid robot hand was prepared using the demonstrated tactile sensing function.

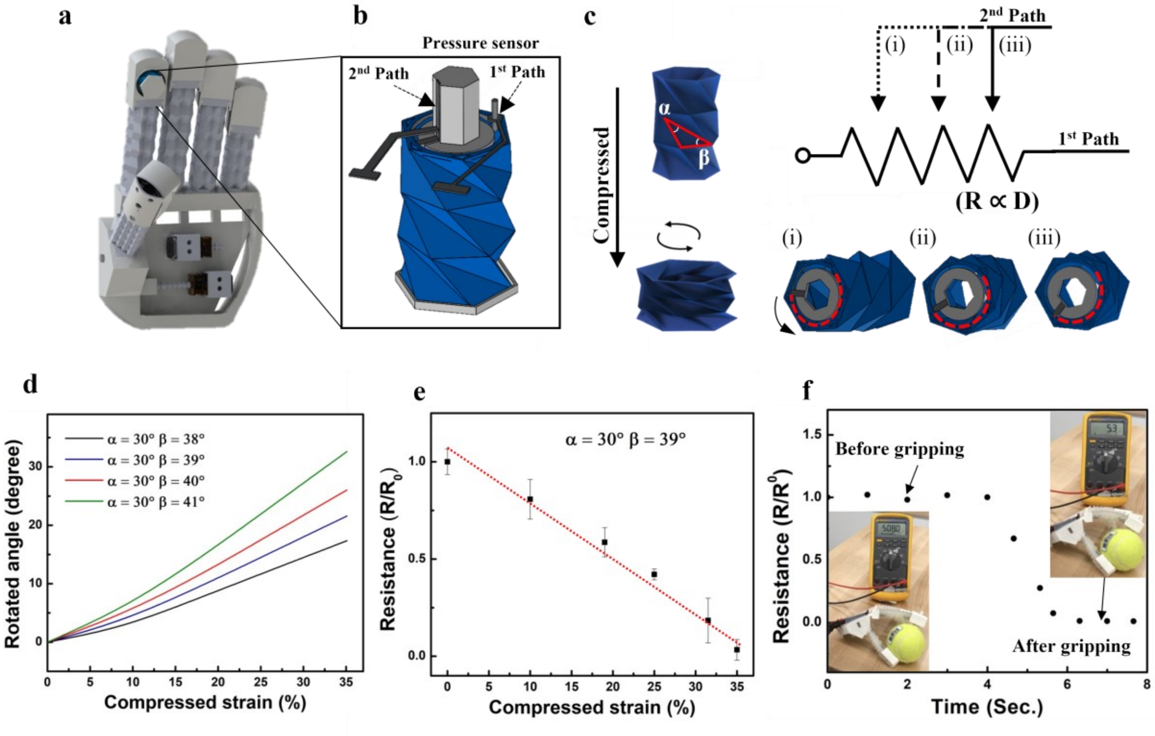

Figure 5.3. **3D printed humanoid hand with 3D origami tactile sensor. (a) Schematics of the humanoid robot hand with 3D origami fingers equipped with the tactile sensor on the fingertip. (b) Variable resistance sensor developed by 3D Kresling origami. (c) The rotating behavior of the origami, and its resistive length changes under compression. (d) The rotating angles of the 3D origami at different angular designs. (e) The resistance changes of 3D origami tactile sensor under compression. (f) Resistance changes before and after the gripping a ball.**

5.3.3. Neuromorphic humanoid hand

For neuromorphic robot systems with complete biological sensory neuron network sequences, three different types of functions are required: sensing, signal transmission, and processing functions. Therefore, a portable neuromorphic system, including signal transmission and processing, was developed and integrated with the fabricated robotic hand as a neuromorphic humanoid hand, as shown in Figure 5.4a. The tactile sensors on the fingertips were connected to the neuromorphic system as the input stimuli. The portable neuromorphic system was built with a 3D-shaped oscillator and zinc-tin-oxide (ZTO)-based synaptic transistor for bio-inspired signal transmission and processing, as explained in a previous study.[167] As shown in Figure A11, the 3D oscillator and synaptic transistor were mounted on a printed circuit board. All of the electronic components of the neuromorphic system were designed to be replaceable and modulated into a single 3D structural board; as such, they were considered as portable neuromorphic devices. Portable designs for electronic devices allow for minimizing the additional integration required for robot applications. In addition, with portable devices, we expect that the devices can be utilized for a universal robot system, i.e., not just for the 3D origami robot hand. Moreover, the maintenance of the entire robot system is easier, as it requires only releasing two screws to disassemble the neuromorphic system from the robot.

In this system, the received signal undergoes a few steps on the demonstrated neuromorphic humanoid hand. First, the force detected by tactile sensors on the fingertips is transmitted to the neuromorphic system, followed by its conversion into spike-form signals (such as those in biological systems) by the oscillator. The influence of the touch signal on the output from the oscillator is simulated. As shown in Figure A12a, the tactile sensor is connected between the power source and gate electrode of the transistor. Thus, the pressure-induced resistance change affects the actual power supplied to the gate, resulting in variations in the output AC signal from the oscillator. The amplitude significantly decreases when the resistance is large. A similar experimental result is obtained as shown in Figure A12b, and as summarized in Figure 5.4b. The amplitude drops from 1.6 V to 0.8 V when the resistance is increased from 25 Ω to 100 Ω. Similar results are obtained when the tactile sensor is connected to the source electrode of the transistor, as shown in Figure A12c and Figure A12d.

Second, the performance of synaptic transistors is confirmed before processing the converted signal. Because synapses accomplish memory and learning functions in biological systems, synaptic transistors work as artificial synapses for replicating these functions. As shown in Figure 5.c, two electrodes are fabricated on a ZTO semiconductive layer, followed by encapsulating the device to avoid electrochemical reactions between the electrodes and gate electrolyte. Moreover, to constrain the hydrophilic electrolyte just above the electrodes, a circular wall is fabricated with the facilitation of a digital camera magnifier for accurate nozzle alignment, as shown in Figure A13. The non-volatile memory and learning behaviors of synaptic transistors are accomplished by ion-accumulation at interfaces and ion-doping to the semiconductive layer.[167] As a result, under a continuous pulse positive bias, the postsynaptic current increases with time, as shown in Figure 5.4c.

Finally, the converted signal is transmitted to the synaptic transistor for processing. As mentioned before, a higher pressure on the tactile sensor results in a lower resistance, leading to a larger output signal from the oscillator. Then, the output spike signal is applied to the gate of the synaptic transistor of the integrated neuromorphic system. In general, a higher positive bias on the synaptic transistor results in a larger current, as more ions accumulate at the interface and are doped inside the semiconductive channel. This phenomenon can be confirmed using the integrated neuromorphic systems, as illustrated in Figure 5.d. An increasing force enlarges the postsynaptic current owing to a smaller resistance under a larger force, and vice versa. Moreover, when applied to a constant force, the postsynaptic current also increases with time owing to the non-volatile effect, as shown in Figure 5.4e. This increase lasts until the force is retrieved.

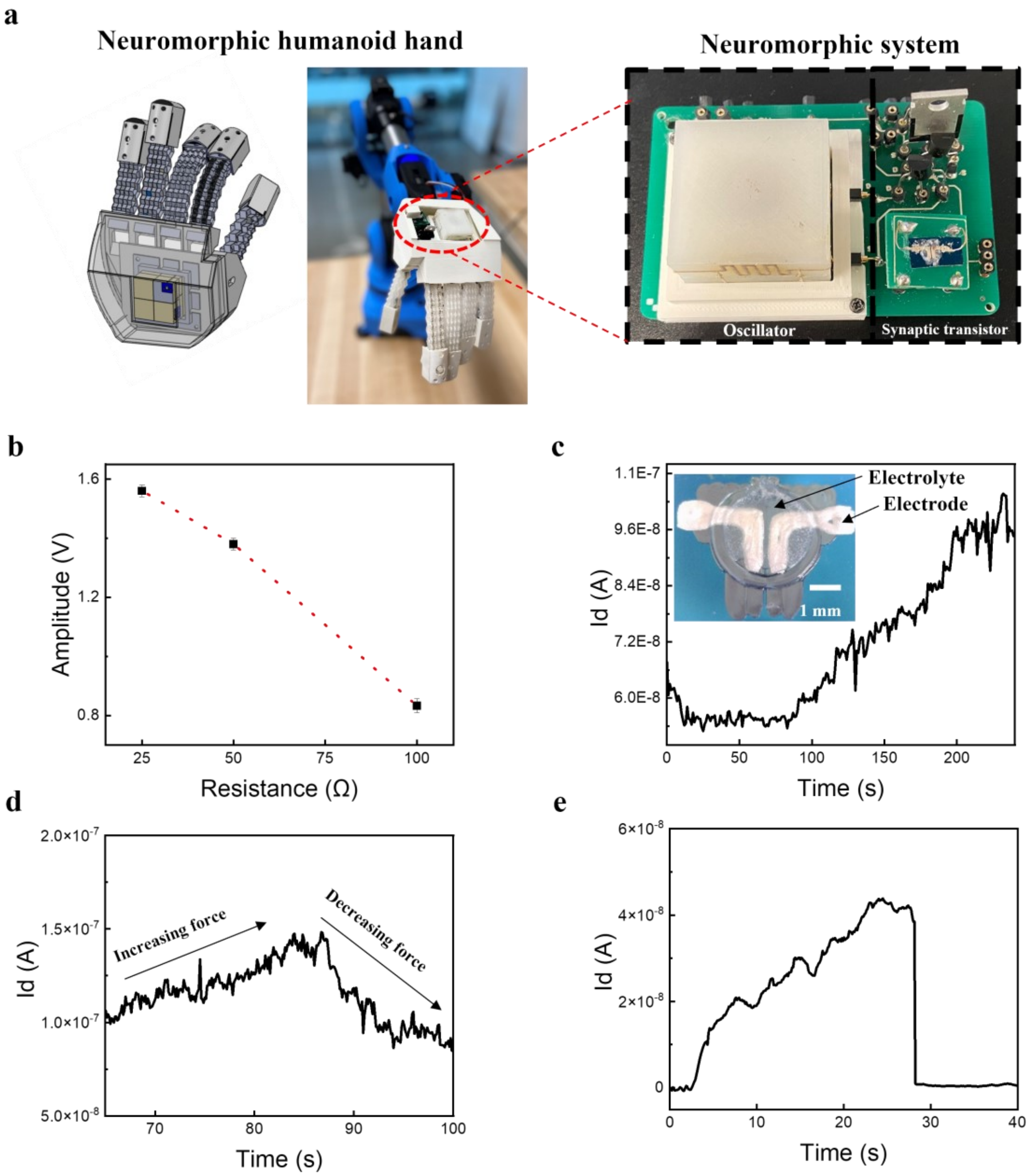

Figure 5.4. Neuromorphic humanoid hand. (a) Left: design and image of the integrated neuromorphic humanoid hand; Right: details of the 3D portable neuromorphic system, constructed by a 3D shaped oscillator and a synaptic transistor. (b) Relation between the amplitude of the output signal from the 3D shaped oscillator and resistance. (c) Non-volatile memory effect of synaptic transistor. d, Synaptic current change with variable force. (e) Synaptic current change with a constant force.

5.3.4. Reflex arc function through artificially intelligent robot hands

In biological systems, after receiving a signal from a sensory neuron network, the brain makes a decision as a response to environmental stimuli to actuate organs. However, another type of response-unconscious response is also performed through reflex arcs in biological systems, without a neural response from the brain.[169] A bio-inspired neuromorphic humanoid hand must be equipped with such functions to act as an artificially intelligent robot.

In general, an environmental stimulus can be captured, transmitted, and processed by integrating the tactile sensor with the demonstrated neuromorphic system. However, to fully replicate a bio-inspired reflex arc, the actuation function needs to be realized as an unconscious response. In general, the degree of an unconscious responses depends on experience. For example, the gripping force for one person to grip an unknown object at the first time is different from the force to grip it a second time. This is because experience is obtained by gripping the unknown object. Thus, a suitable force can be applied for secondary gripping after obtaining the experience. In other words, the experience obtained through training influences the degree of the reflex arc. Therefore, by realizing the bio-inspired reflex arc function for an unconscious response, the fabricated neuromorphic humanoid hand becomes a bio-inspired artificially intelligent robot. Figure 5.5a illustrates a strategy for this artificially intelligent robot to grip objects by training. First, the signal is detected on the fingertips, followed by transmission and processing by the neuromorphic system. Then, the output from the neuromorphic system is applied to the motors, which manipulate the gripping motion of the fingers on the humanoid hand. Before training, the initial gripping force based on previous experience is not strong enough to hold the object. However, after a few training cycles, the neuromorphic system increased the gripping force unconsciously by an amount sufficient to hold the object.

The proposed strategy is verified through the following steps. First, the robot hand is trained three times using the same force. As shown in Figure 5.b, the output from the oscillator is nearly the same in each case, as the force on the tactile sensor is constant as a repeated input for each training. However, the motor driving voltage from the neuromorphic system is gradually increased with the training time owing to the non-volatile effect mentioned above, as shown in Figure 5.c. Figure 5.d illustrates the detailed training procedure for the neuromorphic humanoid hand by grasping an unknown object. Before training, the ball is dropped, owing to the weak gripping force. After the first training, the bending of the finger is larger than the initial state and creates a stronger touch on the ball, thereby representing a stronger gripping force. After two more trainings, the depth of touch is increased to produce a much stronger gripping. Finally, the motor is driven to produce sufficient force to hold the ball. Thus, a bio-inspired artificially intelligent robot with a trainable reflex arc is demonstrated.

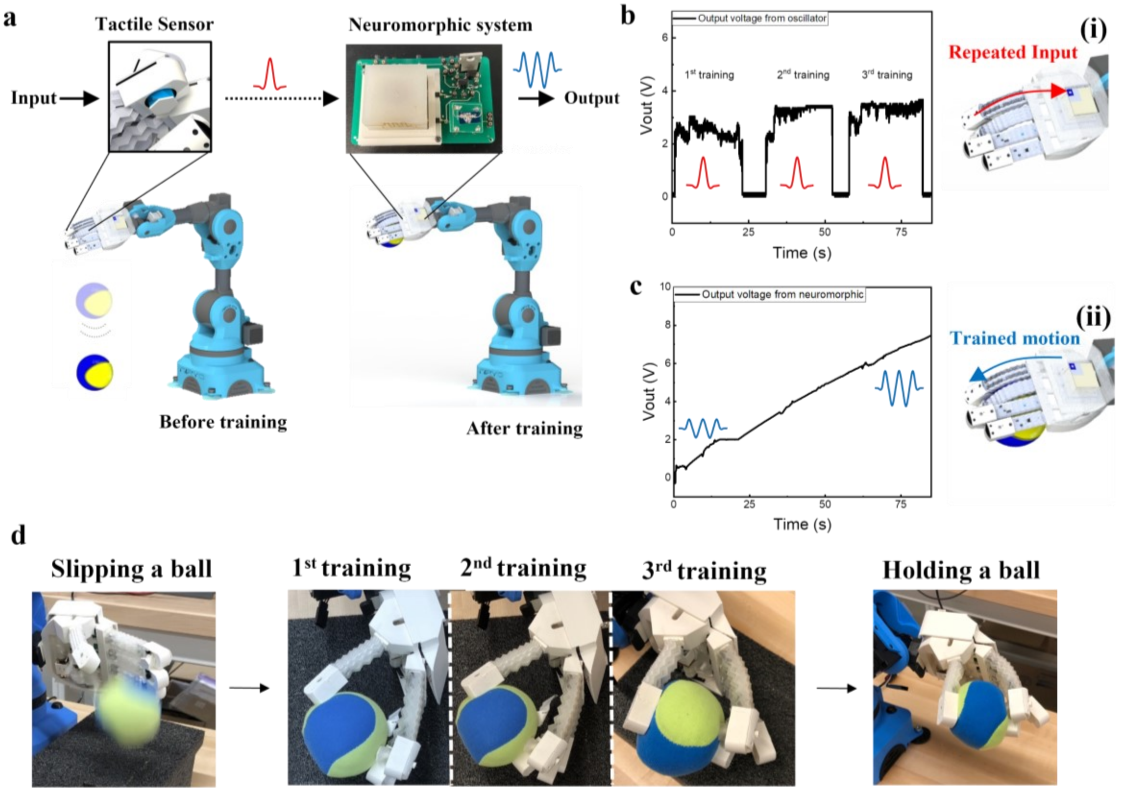

Figure 5.5. **Artificially intelligent robot through unconscious response. (a) Procedure for realizing unconscious response. (b) Relation of the output from the oscillator under repeated trainings. (c) Relation of the output from the neuromorphic system under repeated trainings. (d) Images of gripping motions: Slipping a ball before training, 1st training, 2nd training, 3rd training, and final holding of a ball.**

5.4. Methods

5.4.1. Preparation and characterization of humanoid hand.

An FFF 3D printer with a direct-drive type (TI-D3 pro, Tenlog, ltd) was used to prepare the architectured 3D origami fingers and potentiometric sensors of the humanoid robot hands. The filament for the 3D printer was a commercial Ninjaflex TPU85A (Fenner Drivers, Inc.). The origami structures were designed using Solidworks as a 3D CAD file; then, the file was converted to g-codes using the Cura slicer program (Ultimaker, Ltd.) for the 3D printing process. The nozzle size of the hotend was 0.2 mm. The print speed, infill, layer height, temperature, and width for the printing process were 30 mm/s, 0.1 mm, 223 °C, and 0.2 mm, respectively. A commercial polylactic acid (Ulimaker, Ltd) filament was used for the sensor frames and palm, and the FFF 3D printer (with a bowden tube type (Ultimaker 3)) was utilized for printing. The g-code preparation was the same as described above. After printing, each part was carefully assembled and integrated into a commercial six-axis robot arm (Niryo One, Niryo Inc.). The finger motion was actuated and controlled by strings connected to DC motors.

The active layer of the touch sensor for detecting the external force was fabricated using a DIW printer (SHOT mini 100Sx, Musashi Engineering, Inc.) at a speed of 1 mm/s, followed by curing at 80 °C for 1 h. A highly resistive paste ($3.8 \times 10^3\ \Omega\cdot m$) was prepared for the active layer using the solution process. 2 g Urethane triacrylate (oligomer), 0.08 g 2,2'- azobis (2-methylpropionitrile) (radical initiator), and 0.08 g Luperox A75 benzoyl peroxide (thermal initiator) were dissolved in 0.5 g methacrylic acid (monomer). Then, 40 wt% of silver flakes were added and mixed using a SpeedMixer DAC150.1 FVZ-K (FlackTek, Inc.). The viscosity of the silver paste was controlled by heating to 65 °C.

5.4.2. 3D printing of a portable neuromorphic system.

The 3D oscillator substrate was fabricated using an FFF printer (Ultimaker S3, Ultimaker), whereas the conductive traces were fabricated using a six-axis robot DIW printing system (SHOT mini 100Sx and ML-808GX, Musashi Engineering, Inc.). The IR laser (5 W, 808 nm) (IRM808TA-5000FC + ADR-180A Shanghai Laser & Optics Century Co. Ltd.) was modulated using a function generator (SDG2042X, SIGLENT Technologies North America, Inc.). The printing route was controlled by an industrial six-axis robot (R-30iB, FANUC America Corporation) using simulation software (RoboDK, RoboDK Inc.). The printed circuit board (PCB) of the neuromorphic system was designed using the software Altium Designer, and was printed using a PCB printer (V-One, Voltera). The synaptic transistor was prepared using electrolytes with poly (ethylene oxide) (PEO) (0.16 g), lithium perchloride (LiClO4) (0.02 g), and methanol (1.8 mL), followed by drop-casting on the gate of the synaptic transistors. The output of the oscillator was monitored using an oscilloscope (SDS1052DL, SIGLENT Technologies North America, Inc.). Simultaneously, the synaptic transistor and portable neuromorphic system were characterized using a source meter (Keithley 2400, Keithley Instruments), and were monitored through a self-made program by LabView.

5.4.3. Training for sensory humanoid hand

The neuromorphic humanoid hand was connected to the 3D printed six-axis robot arm (Niryo One, Niryo). The motion of the arm was controlled using the Niryo One Studio software. Meanwhile, the gripping motion of the neuromorphic humanoid hand was controlled by the developed neuromorphic system.

5.5. Conclusion

We demonstrate a multi-axis robot DIW method for structural electronics. The six-axis robot DIW method can print conductive traces on vertical and tilted surfaces seamlessly, while keeping continuously vertical to the curvilinear surfaces. We demonstrate a unique DIW method for the fabrication of conductive traces by optimizing parameters such as the speed of robot motion to improve the efficiency of the 3D printing process.

A sensory humanoid hand with a novel origami touch sensor showing adjustable resistance sensing is 3D printed. It is designed with origami fingers and origami tactile sensors. A portable neuromorphic system is integrated with a 3D printed oscillator and synaptic transistor for the transmission and processing of signals. The 3D structural neuromorphic robot hands are ultimately created by integrating the fabricated sensory humanoid hand with a portable neuromorphic system providing a proception function, including the detection, transmission, and processing of signals.

Finally, the neuromorphic humanoid hand can control its motion unconsciously, as the artificially intelligent robot mimics the reflex arc performance. The robot hand is trained to replicate the learning progress of gripping a ball, similar to the gripping motion of human hands. Different gripping forces are monitored through the compressed depths to the soft ball with different steps, such as before training, during training, and after training. The neuromorphic humanoid hand demonstrates an increased gripping force sufficient to hold an unknown object. Thus, an artificially intelligent robot band is exhibited with the capability of learning an unconscious response through training.

Chapter 6.

Conclusions and Future Works

In this chapter, the major milestones of this thesis are summarized. The contribution from this thesis to the research field of neuromorphic systems is reiterated. Then, the contributed journal and conference publications based on this PhD thesis research are listed. Finally, the potential future works are discussed.

6.1. Conclusions

This thesis focuses on the development of bio-inspired 3D printed neuromorphic systems. Neuromorphic systems are designed with the bio-inspired device for signal perception, where sensors served as artificial organs to detect the environmental stimulus; and 3D oscillators served as artificial neurons to convert and transmit the detected signal; and synaptic transistors served as artificial synapses to process the signals. When the neuromorphic system is integrated with an electrochemical or tactile sensor, the proposed neuromorphic system detects ion concentrations or gripping forces. Then, it provided decision-making based on the learning and memory functions through training to magnify output automatically. Overall, it is concluded that the developed neuromorphic sensing system shows the potential to replicate the signal perception function of human beings. The demonstrated novel multi-axis robot 3D printing provides a new approach for 3D structural printing.

Conclusion is summarized with three aspects of research milestones:

1. **3D Printed Electrochemical Sensor**

- ISEs was designed and fabricated as an artificial receptor for selective ion detection. The performance of three different membranes for NH_4^+, K^+, and Ca^{2+} ions was studied. The device demonstrated sensitivity as 100, 104, and 42 mV/decade for NH_4^+, K^+, and Ca^{2+} membrane, respectively.

- ZTO-based oxide FETs were fabricated with 3D printed silver electrodes. The serpentine design demonstrates the optimal FETs outputs thanks to the uniform channel for stable performance.

- Printed ISEs and FETs were integrated as ISFETs by connecting the extended WE to the backside of FETs. Through interference study, the three ion-selective membranes showed a higher sensitivity for primary ions than interference ions.

2. 3D Neuromorphic Sensory System-Electrochemical Sensing

- 3D shaped inductors were designed with a 3D shaped magnetic core and fabricated by the 3D DIW printing system. Both the simulation result by Maxwell-ANSYS and the experimental result confirmed that inductance increased with the number of wire turns. Capacitors were designed and printed with a 3D IDE structure. The resonant frequency of the LC resonator constructed with the fabricated 3D inductor and IDE capacitor was 2.36 GHz, similar to the simulated frequency of 2.26 GHz by Maxwell-ANSYS.

- 3D LC oscillator, constructed with the printed 3D inductor, IDE capacitor, and resistor, was used to transmit the signals as artificial neurons. The resonant frequency was simulated by the LTspice software, which was similar to the experimental measurement.

- ZTO-based synaptic transistors were fabricated as artificial synapses for signal processing. The potentiation and depression performance were monitored, which were related to the non-volatile memory function. The mechanism of synaptic transistors with the non-volatile effect was further investigated as the ion accumulation and doping for the demonstration of training.

- The fabricated sensor, artificial neuron, and artificial synapse were integrated as a neuromorphic sensory system with bio-inspired perception function, including sensing, signal transmission, and signal processing, respectively. The signal perception process was confirmed step by step. The neuromorphic system exhibited the learning and memory effect through carefully designed experiments, which were eventually utilized to detect small concentrations of K^+ ions in the artificial soil.

3. 3D Structural Neuromorphic Tactile Sensing System

- The 3D origami tactile sensor was integrated with the developed neuromorphic system. By integration of the 3D neuromorphic tactile sensing system with the fingertips, the 3D neuromorphic humanoid hand was demonstrated for intelligent tactile sensing.

- A portable neuromorphic system was developed on a PCB board, which provided convenient replacement and integration advantages. By mounting it on the humanoid hand, a neuromorphic tactile sensing system was achieved with the bio-inspired perception function.

- The unconscious response of the neuromorphic tactile sensing system was demonstrated. By training the neuromorphic system through gripping of the humanoid hand, the output voltage was automatically increased. After training, the motor produced enough force to hold a ball with the increased output voltage from the neuromorphic system. The bio-inspired unconscious response was replicated without any program control units.

6.2. Contributions

This thesis contributes to the area of neuromorphic sensing systems where 3D sensors, 3D LC oscillators, and synaptic transistors are introduced based on 3D printing technologies. The bio-inspired perception function was achieved by the integrated neuromorphic sensing system, including sensing, signal transmission, and signal processing.

This thesis proposes a neuromorphic tactile sensing system. With the learning and memory function, the neuromorphic tactile sensing system was utilized to control the motion of the 3D printed humanoid hand, realizing the bio-inspired unconscious response. The contributions of this thesis are:

- The work on the ISE sensor by 3D printing method provides an alternative design and fabrication method for electrochemical sensors with high sensitivity and selectivity.

- Design and fabrication of 3D structural electronics, including inductors, capacitors, even 3D LC oscillators, provide an alternative procedure in the 3D electronics field by the 3D printing method.

- LC oscillators are used for signal transmission, including converting the signal to spike form signal as neurons. This study presents a novel way to fabricate artificial neurons.

- As artificial synapses, 3D printed ZTO-based synaptic transistors were demonstrated with the non-volatile memory effect, resulting in the neuromorphic system's training function.

- A novel 3D printing system, using a multi-axis robot to control the motion of a DIW printer, provides a new tool for the paste-based DIW printing field.

- The neuromorphic system is designed as a portable system, where the oscillator and synaptic transistor are replaceable conveniently when they are degraded. By integrating with sensors, the neuromorphic sensing system shows the function of bio-inspired signal perception.

- A 3D printed humanoid hand with the portable neuromorphic tactile sensing system was demonstrated for the unconscious response of tactile sensing.

6.3. Publications

The following list of journals and conference papers were published based on my PhD projects in the SFU.

Journal Publications

[1] **C. Bao**, T. H. Kim, A. Hassanpoor Kalhori and W. S. Kim, “Neuromorphic Humanoid Hands Built by 6-axis Robot 3D Printing”. *submitted* (2021).

[2] **C. Bao**, S. K. Seol and W. S. Kim, “A 3D Integrated Neuromorphic Chemical Sensing System”. *Sensors and Actuators B: Chemical* 332 129527 (2021).

[3] **C. Bao**, and W. S. Kim, “Perspective of Printed Solid - State Ion Sensors toward High Sensitivity and Selectivity”. *Advanced Engineering Materials* 2000116 1-14 (2020).

[4] **C. Bao**, M. Kaur, and W. S. Kim, “Toward a Highly Selective Saliva Sensors using Printed Field Effect Transistors”. *Sensors and Actuators B: Chemical* 285 186-192 (2019).

[5] T. H. Kim, **C. Bao** and W. S. Kim, “3D Printed Flexible ECG Sensing Robot”. *submitted* (2021).

[6] D. Baker, **C. Bao**, and W. S. Kim, “Highly Conductive 3D Printable Materials for 3D Structural Electronics”. *ACS Applied Electronic Materials in press* (2021).

[7] X. Min, **C. Bao**, Kim, and W. S. Kim, “Additively Manufactured Digital Microfluidic Platforms for Ion-selective Sensing”. *ACS Sensors* 4(4) 918-923 (2019).

[8] T. Kim, **C. Bao**, M. Hausmann, G. Siqueira, T. Zimmermann, W. S. Kim, “3D Printed Disposable Wireless Ion Sensors with Biocompatible Cellulose Composites”. *Advanced Electronic Materials* 5(2) 1800778 (2018).

[9] Y. Dong, **C. Bao**, and W.S. Kim, “Sustainable Additive Manufacturing of Printed Circuit Boards” *Joule* 2(4) 579-582 (2018).

[10] D. Baker, T. H. Kim, **C. Bao**, and W. S. Kim, “3D Structural Electronics by Coaxial printing” *Submitted* (2021)

Conference Publications

[1] **C. Bao**, and W.S. Kim, “3D Printed Flexible Integrated LC Circuits”. In 2019 *International Flexible Electronics Technology Conference (IFETC)*. (pp. 1-2). IEEE.

[2] **C. Bao**, M. Kaur, and W. S. Kim, “3D Printed Ion Selective Sensors”. MRS spring (2019)

[3] **C. Bao**, and W.S. Kim, “3D Printed Ion-Selective Field Effect Transistors”. In 2018 *International Flexible Electronics Technology Conference (IFETC)* (pp. 1-3). IEEE.

[4] X. Min, **C. Bao**, and W.S. Kim, “New Ion-selective Sensing Platform: Additively Manufactured Flexible Digital Microfluidic System”. In 2019 *International Flexible Electronics Technology Conference (IFETC).* (pp. 7-9). IEEE.

6.4. Opportunities for Future Work

The work of this thesis is intended to develop neuromorphic sensing systems by the 3D printing method. There are some other research directions that can be further studied as the extension of this study:

1. **Other types of sensors**: This thesis has already demonstrated a neuromorphic system adapted to electrochemical senor and tactile sensors. Other types of sensors can be further integrated with the proposed neuromorphic system to replicate the rest of the human senses with a complete bio-signal perception procedure, such as smell, sight, sound, et al.

2. **Multiple input and output signals**: Since the information transfer between actual neurons and synapses is spatial and temporal, much work can be further carried out to create new neuromorphic sensing systems that deal with multiple input signals and multiple output signals.

3. **Artificially intelligent robots**: Using the neuromorphic tactile sensing system to control the humanoid hand by training is the first attempt to obtain an artificially intelligent robot for the demonstration of unconscious response. Other types of neuromorphic sensing systems can be further integrated with humanoid fingers to achieve more intelligent robots.

References

[1] C. Mead, Neuromorphic Electronic Systems, Proc. IEEE. 78 (1990) 1629–1636. doi:10.1109/5.58356.

[2] L.Q. Zhu, C.J. Wan, L.Q. Guo, Y. Shi, Q. Wan, Artificial synapse network on inorganic proton conductor for neuromorphic systems, Nat. Commun. 5 (2014) 1–7. doi:10.1038/ncomms4158.

[3] Y. Fu, L.A. Kong, Y. Chen, J. Wang, C. Qian, Y. Yuan, J. Sun, Y. Gao, Q. Wan, Flexible Neuromorphic Architectures Based on Self-Supported Multiterminal Organic Transistors, ACS Appl. Mater. Interfaces. 10 (2018) 26443–26450. doi:10.1021/acsami.8b07443.

[4] R.A. John, N. Tiwari, M.I. Bin Patdillah, M.R. Kulkarni, N. Tiwari, J. Basu, S.K. Bose, Ankit, C.J. Yu, A. Nirmal, S.K. Vishwanath, C. Bartolozzi, A. Basu, N. Mathews, Self healable neuromorphic memtransistor elements for decentralized sensory signal processing in robotics, Nat. Commun. 11 (2020) 1–12. doi:10.1038/s41467-020-17870-6.

[5] M. Wang, Y. Luo, T. Wang, C. Wan, L. Pan, S. Pan, K. He, A. Neo, X. Chen, Artificial Skin Perception, Adv. Mater. 2003014 (2020) 1–20. doi:10.1002/adma.202003014.

[6] Y. Tuchman, T.N. Mangoma, P. Gkoupidenis, Y. Van De Burgt, R.A. John, N. Mathews, S.E. Shaheen, R. Daly, G.G. Malliaras, A. Salleo, Organic neuromorphic devices: Past, present, and future challenges, MRS Bull. 45 (2020) 619–630. doi:10.1557/mrs.2020.196.

[7] S. Han, H. Mao, W.J. Dally, Deep compression: Compressing deep neural networks with pruning, trained quantization and Huffman coding, ArXiv Prepr. ArXiv. (2015) 1510.00149.

[8] G.E. Moore, Cramming more components onto integrated circuits, Electronics. 38 (1965) 114–117. doi:10.1109/JPROC.1998.658762.

[9] Q. Xia, J.J. Yang, Memristive crossbar arrays for brain-inspired computing, Nat. Mater. 18 (2019) 309–323. doi:10.1038/s41563-019-0291-x.

[10] K. Berggren, Q. Xia, K.K. Likharev, D.B. Strukov, H. Jiang, T. Mikolajick, D. Querlioz, M. Salinga, J.R. Erickson, S. Pi, F. Xiong, P. Lin, C. Li, Y. Chen, Roadmap on emerging hardware and technology for machine learning, Nanotechnology. 32 (2020) 012002.

[11] L.S. Smith, A. Hamilton, Neuromorphic systems: engineering silicon from neurobiology, World Scientific, 1998.

[12] W. Xu, S.-Y. Min, H. Hwang, T.-W. Lee, Organic core-sheath nanowire artificial synapses with femtojoule energy consumption, Sci. Adv. 2 (2016) e1501326. doi:10.1126/sciadv.1501326.

[13] Y. Lee, T.W. Lee, Organic Synapses for Neuromorphic Electronics: From Brain-Inspired Computing to Sensorimotor Nervetronics, Acc. Chem. Res. 52 (2019) 964–974. doi:10.1021/acs.accounts.8b00553.

[14] C. Wan, G. Chen, Y. Fu, M. Wang, N. Matsuhisa, S. Pan, An Artificial Sensory Neuron with Tactile Perceptual Learning, Adv. Mater. 30 (2018) 1801291. doi:10.1002/adma.201801291.

[15] X. Zhu, W.D. Lu, Optogenetics-Inspired Tunable Synaptic Functions in Memristors, ACS Nano. 12 (2018) 1242–1249. doi:10.1021/acsnano.7b07317.

[16] H. Tan, Q. Tao, I. Pande, S. Majumdar, F. Liu, Y. Zhou, P.O.Å. Persson, J. Rosen, S. van Dijken, Tactile sensory coding and learning with bio-inspired optoelectronic spiking afferent nerves, Nat. Commun. 11 (2020) 1–9. doi:10.1038/s41467-020-15105-2.

[17] C. Wan, P. Cai, X. Guo, M. Wang, N. Matsuhisa, L. Yang, Z. Lv, Y. Luo, X.J. Loh, X. Chen, An artificial sensory neuron with visual-haptic fusion, Nat. Commun. 11 (2020) 1–9. doi:10.1038/s41467-020-18375-y.

[18] C. Ge, C. xiang Liu, Q. li Zhou, Q. hua Zhang, J. yu Du, J. kun Li, C. Wang, L. Gu, G. zhen Yang, K. juan Jin, A Ferrite Synaptic Transistor with Topotactic Transformation, Adv. Mater. 31 (2019) 1–9. doi:10.1002/adma.201900379.

[19] B.C. Jang, S. Kim, S.Y. Yang, J. Park, J.H. Cha, J. Oh, J. Choi, S.G. Im, V.P. Dravid, S.Y. Choi, Polymer Analog Memristive Synapse with Atomic-Scale Conductive Filament for Flexible Neuromorphic Computing System, Nano Lett. 19 (2019) 839–849. doi:10.1021/acs.nanolett.8b04023.

[20] W.H. Kautz, Cellular logic-in-memory arrays, IEEE Trans. Comput. 100 (1969) 719–727.

[21] D. V Christensen, R. Dittmann, B. Linares-barranco, A. Sebastian, M. Le Gallo, A. Redaelli, S. Slesazeck, T. Mikolajick, S. Spiga, S. Menzel, I. Valov, G. Milano, C. Ricciardi, S. Liang, F. Miao, M. Lanza, T.J. Quill, T. Scott, A. Salleo, J. Grollier, D. Marković, A. Mizrahi, P. Yao, J.J. Yang, G. Indiveri, J.P. Strachan, S. Datta, E. Vianello, A. Valentian, X. Li, W.H.P. Pernice, H. Bhaskaran, E. Neftci, S. Ramaswamy, J. Tapson, F. Scherr, W. Maass, P. Panda, Y. Kim, S. Thorpe, C. Bartolozzi, T.A. Cleland, C. Posch, S. Liu, N. Mazumder, M. Hosseini, T. Mohsenin, E. Donati, S. Tolu, R. Galeazzi, 2021 Roadmap on Neuromorphic Computing and Engineering, ArXiv Prepr. ArXiv. (2021) 2105.05956.

[22] L. Chua, Memristor-The Missing Circuit Element, Solid State Commun. 9 (1971) 705–707.

[23] L. Chua, Resistance switching memories are memristors, Appl. Phys. A Mater. Sci. Process. 102 (2011) 765–783. doi:10.1007/s00339-011-6264-9.

[24] A.P. James, Deep Learning Classifiers with Memristive Networks, Springer, 2020. doi:10.1007/978-3-030-14524-8.

[25] T.M. Taha, R. Hasan, C. Yakopcic, Memristor crossbar based multicore neuromorphic processors, 2014 27th IEEE Int. Syst. Conf. (2014) 383–389.

[26] Q. Liu, Y. Liu, J. Li, C. Lau, F. Wu, A. Zhang, Z. Li, M. Chen, H. Fu, J. Draper, X. Cao, C. Zhou, Fully Printed All-Solid-State Organic Flexible Artificial Synapse for Neuromorphic Computing, ACS Appl. Mater. Interfaces. 11 (2019) 16749–16757. doi:10.1021/acsami.9b00226.

[27] S. Park, M. Chu, J. Kim, J. Noh, M. Jeon, B.H. Lee, H. Hwang, B. Lee, B. Lee, Electronic system with memristive synapses for pattern recognition, Sci. Rep. 5 (2015) 1–9. doi:10.1038/srep10123.

[28] P. Yao, H. Wu, B. Gao, S.B. Eryilmaz, X. Huang, W. Zhang, Q. Zhang, N. Deng, L. Shi, H.S.P. Wong, H. Qian, Face classification using electronic synapses, Nat. Commun. 8 (2017) 1–8. doi:10.1038/ncomms15199.

[29] Y. Van De Burgt, A. Melianas, S.T. Keene, G. Malliaras, A. Salleo, Organic electronics for neuromorphic computing, Nat. Electron. 1 (2018) 386–397. doi:10.1038/s41928-018-0103-3.

[30] M. Le Gallo, A. Sebastian, An overview of phase-change memory device physics, J. Phys. D. Appl. Phys. 53 (2020) 213002.

[31] D. Kuzum, R.G.D. Jeyasingh, B. Lee, H.P. Wong, Nanoelectronic programmable synapses based on phase change materials for brain-inspired computing, Nano Lett. 12 (2012) 2179–2186.

[32] Q. Wan, F. Zeng, J. Yin, Y. Sun, Y. Hu, J. Liu, Y. Wang, G. Li, D. Guo, F. Pan, Phase-change nanoclusters embedded in a memristor for simulating synaptic learning, Nanoscale. 11 (2019) 5684–5692. doi:10.1039/c8nr09765h.

[33] G.W. Burr, R.M. Shelby, A. Sebastian, S. Kim, S. Sidler, K. Virwani, M. Ishii, P. Narayanan, A. Fumarola, L.L. Sanches, I. Boybat, M. Le Gallo, K. Moon, J. Woo, H. Hwang, Y. Leblebici, G.W. Burr, R.M. Shelby, A. Sebastian, S. Kim, S. Sidler, K. Virwani, M. Ishii, P. Narayanan, A. Fumarola, L.L. Sanches, I. Boybat, M. Le Gallo, K. Moon, J. Woo, H. Hwang, Neuromorphic computing using non-volatile memory, Adv. Phys. X. 2 (2017) 89–124. doi:10.1080/23746149.2016.1259585.

[34] J.H. Yoon, Z. Wang, K.M. Kim, H. Wu, V. Ravichandran, Q. Xia, C.S. Hwang, J.J. Yang, An artificial nociceptor based on a diffusive memristor, Nat. Commun. 9 (2018) 1–9. doi:10.1038/s41467-017-02572-3.

[35] B.H.P. Wong, F. Ieee, H. Lee, S. Yu, S.M. Ieee, Y. Chen, Y. Wu, P. Chen, B. Lee, F.T. Chen, M. Tsai, Metal-Oxide RRAM, Proc. IEEE. 100 (2012) 1951–1970.

[36] N.R. Hosseini, J. Lee, I. Pet, Biocompatible and Flexible Chitosan-Based Resistive Switching Memory with Magnesium Electrodes, Adv. Funct. Mater. 25 (2015) 5586–5592. doi:10.1002/adfm.201502592.

[37] S. Lee, H. Park, C. Keum, I. Lee, M. Kim, S. Lee, Organic Flexible Memristor with Reduced Operating Voltage and High Stability by Interfacial Control of Conductive Filament Growth, RAPID Res. Lett. 13 (2019) 1900044. doi:10.1002/pssr.201900044.

[38] S. Lee, H. Park, M. Kim, S. Kang, S. Lee, Interfacial Triggering of Conductive Filament Growth in Organic Flexible Memristor for High Reliability and Uniformity, ACS Appl. Mater. Interfaces. 11 (2019) 30108–30115. doi:10.1021/acsami.9b10491.

[39] S.J. Ge, S. Pan, Flexible artificial nociceptor using a biopolymer-based forming-free memristor, Nanoscale. 11 (2019) 6591–6601. doi:10.1039/c8nr08721k.

[40] M. Kim, J. Lee, Ultralow Power Consumption Flexible Biomemristors, ACS Appl. Mater. Interfaces. 10 (2018) 10280–10286. doi:10.1021/acsami.8b01781.

[41] H. Park, Y. Lee, N. Kim, D. Seo, G. Go, T. Lee, Flexible Neuromorphic Electronics for Computing, Soft Robotics, and Neuroprosthetics, Adv. Mater. 32 (2020) 1903558. doi:10.1002/adma.201903558.

[42] E.Y. Tsymbal, H. Kohlstedt, Tunneling Across a Ferroelectric, Science. 313 (2006) 181–184.

[43] A. Chanthbouala, V. Garcia, R.O. Cherifi, K. Bouzehouane, S. Fusil, X. Moya, S. Xavier, H. Yamada, C. Deranlot, N.D. Mathur, M. Bibes, A. Barthélémy, J. Grollier, A ferroelectric memristor, Nat. Mater. 11 (2012) 860–864. doi:10.1038/nmat3415.

[44] Y. Van De Burgt, E. Lubberman, E.J. Fuller, S.T. Keene, C. Grégorio, A non-volatile organic electrochemical device as a low-voltage artificial synapse for neuromorphic computing : Nature Materials : Nature Research, Nature.Com. (n.d.). https://www.nature.com/nmat/journal/v16/n4/full/nmat4856.html%0Apapers3://publication/uuid/7CB7FB68-EA25-4CF6-AAD4-E174F38A33DB.

[45] Y. Ren, J. Yang, L. Zhou, J. Mao, S. Zhang, Y. Zhou, S. Han, Gate-tunable synaptic plasticity through controlled polarity of charge trapping in fullerene composites, Adv. Funct. Mater. 28 (2018) 1805599.

[46] C. Kim, S. Sung, M. Yoon, Synaptic organic transistors with a vacuum-deposited charge-trapping nanosheet, Sci. Rep. 6 (2016) 1–8. doi:10.1038/srep33355.

[47] S. Wang, M. Ha, M. Manno, C.D. Frisbie, C. Leighton, Hopping transport and the Hall effect near the insulator-metal transition in electrochemically gated poly(3-hexylthiophene) transistors, Nat. Commun. 3 (2012) 0–6. doi:10.1038/ncomms2213.

[48] X. Wan, Y. Yang, P. Feng, Y. Shi, Q. Wan, Short-Term Plasticity and Synaptic Filtering Emulated in Electrolyte-Gated IGZO Transistors, IEEE ELECTRON DEVICE Lett. 37 (2016) 299–302.

[49] C.J. Wan, Y.H. Liu, L.Q. Zhu, P. Feng, Y. Shi, Q. Wan, Short-Term Synaptic Plasticity Regulation in Solution-Gated Indium− Gallium−Zinc-Oxide Electric-Double-Layer Transistors, ACS Appl. Mater. Interfaces. 8 (2016) 9762–9768.

[50] B. Tian, L. Liu, M. Yan, J. Wang, Q. Zhao, N. Zhong, P. Xiang, L. Sun, H. Peng, H. Shen, T. Lin, B. Dkhil, X. Meng, J. Chu, X. Tang, C. Duan, A Robust Artificial Synapse Based on Organic Ferroelectric Polymer, Adv. Electron. Mater. 5 (2019) 1800600.

[51] M. Kim, J. Lee, Ferroelectric Analog Synaptic Transistors, Nano Lett. 19 (2019) 2044–2050. doi:10.1021/acs.nanolett.9b00180.

[52] M.J. Berridge, P. Lipp, M.D. Bootman, The versatility and universality of calcium signalling, Nat. Rev. Mol. Cell Biol. 1 (2000) 11–21.

[53] T. Kyung, S. Lee, J.E. Kim, T. Cho, H. Park, Y. Jeong, D. Kim, A. Shin, S. Kim, J. Baek, J. Kim, N.Y. Kim, D. Woo, S. Chae, C. Kim, H. Shin, Y. Han, D. Kim, W. Do Heo, Optogenetic control of endogenous Ca2+ channels in vivo, Nat. Biotechnol. 33 (2015) 1092–1096. doi:10.1038/nbt.3350.

[54] Y. Kim, A. Chortos, W. Xu, Y. Liu, J.Y. Oh, D. Son, J. Kang, A.M. Foudeh, C. Zhu, Y. Lee, S. Niu, J. Liu, R. Pfattner, Z. Bao, T.-W. Lee, A bioinspired flexible organic artificial afferent nerve, Science. 360 (2018) 998–1003. doi:10.1126/science.aao0098.

[55] Y. Lee, J.Y. Oh, W. Xu, O. Kim, T.R. Kim, J. Kang, Y. Kim, D. Son, J.B.-H. Tok, M.J. Park, Z. Bao, T.-W. Lee, Stretchable organic optoelectronic sensorimotor synapse, Sci. Adv. 4 (2018) eaat7387. doi:10.1126/sciadv.aat7387.

[56] K. V Wong, A. Hernandez, A Review of Additive Manufacturing, Int. Sch. Res. Not. (2012). doi:10.5402/2012/208760.

[57] W.E. Frazier, Metal Additive Manufacturing: A Review, J. Mater. Eng. Perform. 23 (2014) 1917–1928. doi:10.1007/s11665-014-0958-z.

[58] F.P.W. Melchels, J. Feijen, D.W. Grijpma, Biomaterials A review on stereolithography and its applications in biomedical engineering, Biomaterials. 31 (2010) 6121–6130. doi:10.1016/j.biomaterials.2010.04.050.

[59] X. Zheng, H. Lee, T.H. Weisgraber, M. Shusteff, J. DeOtte, E.B. Duoss, J.D. Kuntz, M.M. Biener, Q. Ge, J.A. Jackson, S.O. Kucheyev, N.X. Fang, C.M. Spadaccini, Ultralight, ultrastiff mechanical metamaterials, Science. 344 (2014) 1373–1377. doi:10.1126/science.1252291.

[60] T. Kim, C. Bao, M. Hausmann, G. Siqueira, T. Zimmermann, W.S. Kim, 3D Printed Disposable Wireless Ion Sensors with Biocompatible Cellulose Composites, Adv. Electron. Mater. 5 (2019) 1800778. doi:10.1002/aelm.201800778.

[61] Y. Dong, C. Bao, W.S. Kim, Sustainable Additive Manufacturing of Printed Circuit Boards, Joule. 2 (2018) 579–582. doi:10.1016/j.joule.2018.03.015.

[62] M.A. Skylar-Scott, S. Gunasekaran, J.A. Lewis, Laser-assisted direct ink writing of planar and 3D metal architectures, Proc. Natl. Acad. Sci. U. S. A. 113 (2016) 6137–6142. doi:10.1073/pnas.1525131113.

[63] Y. Guo, J. Xu, C. Yan, Y. Chen, X. Zhang, X. Jia, Direct Ink Writing of High Performance Architectured Polyimides with Low Dimensional Shrinkage, Adv. Eng. Mater. 1801314 (2019) 1–8. doi:10.1002/adem.201801314.

[64] P. Bergveld, Development, operation, and application of the ion-sensitive field-effect transistor as a tool for electrophysiology, IEEE Trans. Biomed. Eng. BME-19 (1972) 342–351. doi:10.1109/TBME.1972.324137.

[65] S. Nakata, T. Arie, S. Akita, K. Takei, Wearable, flexible, and multifunctional healthcare device with an ISFET chemical sensor for simultaneous sweat pH and skin temperature monitoring, ACS Sensors. 2 (2017) 443–448. doi:10.1021/acssensors.7b00047.

[66] H. Wong, M.H. White, A self contained CMOS integrated pH sensor, Electron Devices Meet. 1988. IEDM '88. Tech. Dig. Int. IEEE. (1988) 658–661. doi:10.1109/IEDM.1988.32899.

[67] L. Wang, L. Li, T. Zhang, X. Liu, J.P. Ao, Enhanced pH sensitivity of AlGaN/GaN ion-sensitive field effect transistor with Al2O3synthesized by atomic layer deposition, Appl. Surf. Sci. 427 (2018) 1199–1202. doi:10.1016/j.apsusc.2017.09.072.

[68] A. Das, D. Hsu, C. Chen, L. Chang, C. Lai, F. Chu, L. Chow, R. Lin, Sensors and Actuators B : Chemical Highly sensitive palladium oxide thin film extended gate FETs as pH sensor, Sensors Actuators B. Chem. 205 (2014) 199–205. doi:10.1016/j.snb.2014.08.057.

[69] Y.-T. Chen, I. Sarangadharan, R. Sukesan, C.-Y. Hseih, G.-Y. Lee, J.-I. Chyi, Y.-L. Wang, High-field modulated ion-selective field-effect-Transistor (FET) sensors with sensitivity higher than the ideal Nernst sensitivity, Sci. Rep. 8 (2018) 1–11. doi:10.1038/s41598-018-26792-9.

[70] S. Ma, Y.K. Lee, A. Zhang, X. Li, Label-free detection of Cordyceps sinensis using dual-gate nanoribbon-based ion-sensitive field-effect transistor biosensor, Sensors Actuators, B Chem. 264 (2018) 344–352. doi:10.1016/j.snb.2018.02.148.

[71] R. Ahmad, N. Tripathy, J.H. Park, Y.B. Hahn, A comprehensive biosensor integrated with a ZnO nanorod FET array for selective detection of glucose, cholesterol and urea, Chem. Commun. 51 (2015) 11968–11971. doi:10.1039/c5cc03656a.

[72] N. Ruecha, J. Lee, H. Chae, H. Cheong, V. Soum, P. Preechakasedkit, O. Chailapakul, G. Tanev, J. Madsen, N. Rodthongkum, O.S. Kwon, K. Shin, Paper-based digital microfluidic chip for multiple electrochemical assay operated by a wireless portable control system, Adv. Mater. Technol. 2 (2017) 1–8. doi:10.1002/admt.201600267.

[73] S. Machida, S. Hideto, Y. Motoyama., Multiple-channel detection of cellular activities by ion-sensitive transistors, Jpn. J. Appl. Phys. 47 (2018) 04FM03.

[74] N. Formisano, N. Bhalla, M. Heeran, J. Reyes Martinez, A. Sarkar, M. Laabei, P. Jolly, C.R. Bowen, J.T. Taylor, S. Flitsch, P. Estrela, Inexpensive and fast pathogenic bacteria screening using field-effect transistors, Biosens. Bioelectron. 85 (2016) 103–109. doi:10.1016/j.bios.2016.04.063.

[75] P. Firek, M. Cichomski, M. Waskiewicz, I. Piwonski, A. Kisielewska, ISFET structures with chemically modified membrane for bovine serum albumin detection, Circuit World. 44 (2018) 45–50. doi:10.1108/CW-10-2017-0061.

[76] M. Waleed Shinwari, M. Jamal Deen, D. Landheer, Study of the electrolyte-insulator-semiconductor field-effect transistor (EISFET) with applications in biosensor design, Microelectron. Reliab. 47 (2007) 2025–2057. doi:10.1016/j.microrel.2006.10.003.

[77] C. Jimenez-Jorquera, J. Orozco, A. Baldi, ISFET based microsensors for environmental monitoring, Sensors. 10 (2010) 61–83. doi:10.3390/s100100061.

[78] G. Taillades, O. Valls, A. Bratov, C. Dominguez, A. Pradel, M. Ribes, ISE and ISFET microsensors based on a sensitive chalcogenide glass for copper ion detection in solution, Sensors Actuators, B Chem. 59 (1999) 123–127. doi:10.1016/S0925-4005(99)00208-7.

[79] D.L. Harame, L.J. Bousse, J.D. Shott, J.D. Meindl, Ion-Sensing Devices with Silicon Nitride and Borosilicate Grlass Insulators, IEEE Trans. Electron Devices. 34 (1987) 1700–1707. doi:10.1109/T-ED.1987.23140.

[80] K. Melzer, V.D. Bhatt, T. Schuster, E. Jaworska, K. Maksymiuk, A. Michalska, P. Lugli, G. Scarpa, Flexible electrolyte-gated ion-selective sensors based on carbon nanotube networks, IEEE Sens. J. 15 (2015) 3127–3134. doi:10.1109/JSEN.2014.2362679.

[81] K. Melzer, V.D. Bhatt, E. Jaworska, R. Mittermeier, K. Maksymiuk, A. Michalska, P. Lugli, Enzyme assays using sensor arrays based on ion-selective carbon nanotube field-effect transistors, Biosens. Bioelectron. 84 (2016) 7–14. doi:10.1016/j.bios.2016.04.077.

[82] B.H. van der Schoot, P. Bergveld, ISFET based enzyme sensors, Biosensors. 3 (1987) 161–186. doi:10.1016/0265-928X(87)80025-1.

[83] F. Buth, A. Donner, M. Sachsenhauser, M. Stutzmann, J.A. Garrido, Biofunctional electrolyte-gated organic field-effect transistors, Adv. Mater. 24 (2012) 4511–4517. doi:10.1002/adma.201201841.

[84] K. Melzer, A.M. Münzer, E. Jaworska, K. Maksymiuk, A. Michalska, G. Scarpa, Polymeric ion-selective membrane functionalized gate-electrodes: Ion-selective response of electrolyte-gated poly (3-hexylthiophene) field-effect transistors, Org. Electron. 15 (2014) 595–601. doi:10.1016/j.orgel.2013.12.016.

[85] K. Schmoltner, J. Kofler, A. Klug, E.J.W. List-Kratochvil, Electrolyte-gated organic field-effect transistor for selective reversible ion detection, Adv. Mater. 25 (2013) 6895–6899. doi:10.1002/adma.201303281.

[86] F.A. Sabah, N.M. Ahmed, Z. Hassan, M. Abdullah Almessiere, Influences of substrate type on the pH sensitivity of CuS thin films EGFET prepared by spray pyrolysis deposition, Mater. Sci. Semicond. Process. 63 (2017) 269–278. doi:10.1016/j.mssp.2017.02.032.

[87] W.J. Cho, C.M. Lim, Sensing properties of separative paper-based extended-gate ion-sensitive field-effect transistor for cost effective pH sensor applications, Solid. State. Electron. 140 (2018) 96–99. doi:10.1016/j.sse.2017.10.025.

[88] H.H. Li, C.E. Yang, C.C. Kei, C.Y. Su, W.S. Dai, J.K. Tseng, P.Y. Yang, J.C. Chou, H.C. Cheng, Coaxial-structured ZnO/silicon nanowires extended-gate field-effect transistor as pH sensor, Thin Solid Films. 529 (2013) 173–176. doi:10.1016/j.tsf.2012.05.045.

[89] D.S. Kim, J.E. Park, J.K. Shin, P.K. Kim, G. Lim, S. Shoji, An extended gate FET-based biosensor integrated with a Si microfluidic channel for detection of protein complexes, Sensors Actuators, B Chem. 117 (2006) 488–494. doi:10.1016/j.snb.2006.01.018.

[90] E.M. Guerra, G.R. Silva, M. Mulato, Extended gate field effect transistor using V2O5 xerogel sensing membrane by sol-gel method, Solid State Sci. 11 (2009) 456–460. doi:10.1016/j.solidstatesciences.2008.07.014.

[91] S. Sasipongpana, Y. Rayanasukha, S. Prichanont, C. Thanachayanont, S. Porntheeraphat, N. Houngkamhang, Extended-gate field effect transistor (EGFET) for carbaryl pesticide detection based on enzyme inhibition assay, Mater. Today Proc. 4 (2017) 6458–6465. doi:10.1016/j.matpr.2017.06.153.

[92] J. Chiang, S. Jhan, S. Hsieh, A. Huang, Hydrogen ion sensors based on indium tin oxide thin film using radio frequency sputtering system, Thin Solid Films. 517 (2009) 4805–4809. doi:10.1016/j.tsf.2009.03.050.

[93] C.H. Lu, T.H. Hou, T.M. Pan, High-performance double-gate α-InGaZnO ISFET pH sensor using a HfO2 gate dielectric, IEEE Trans. Electron Devices. 65 (2018) 237–242. doi:10.1109/TED.2017.2776144.

[94] G.W. Holloway, Y. Song, C.M. Haapamaki, R.R. Lapierre, J. Baugh, Electron transport in InAs-InAlAs core-shell nanowires, Appl. Phys. Lett. 102 (2013). doi:10.1063/1.4788742.

[95] R. Basori, A.K. Raychaudhuri, Floating back-gate field effect transistor fabricated using a single nanowire of charge transfer complex as a channel, J. Phys. Chem. C. 122 (2018) 1054–1060. doi:10.1021/acs.jpcc.7b09960.

[96] J. Tang, C.Y. Wang, F. Xiu, Y. Zhou, L.J. Chen, K.L. Wang, Formation and device application of Ge nanowire heterostructures via rapid thermal annealing, Adv. Mater. Sci. Eng. 2011 (2011). doi:10.1155/2011/316513.

[97] S. Nakata, T. Arie, S. Akita, K. Takei, Flexible integrated chemical and physical sensors toward a wearable healthcare patch, 19th Int. Conf. Solid-State Sensors, Actuators Microsystems. (2017) 1688–1691.

[98] J.J. Schneider, R.C. Hoffmann, J. Engstler, O. Soffke, W. Jaegermann, A. Issanin, A. Klyszcz, A printed and flexible field-effect transistor device with nanoscale zinc oxide as active semiconductor material, Adv. Mater. 20 (2008) 3383–3387. doi:10.1002/adma.200800819.

[99] G.-H. Lee, Y.-J. Yu, X. Cui, N. Petrone, C.-H. Lee, M.S. Choi, D.-Y. Lee, C. Lee, W.J. Yoo, K. Watanabe, T. Taniguchi, C. Nuckolls, P. Kim, J. Hone, Flexible and transparent MoS2 field-effect transistors on hexagonal boron nitride-graphene heterostructures, ACS Nano. 7 (2013) 7931–7936. doi:10.1021/nn402954e.

[100] J.T. Smith, S.S. Shah, M. Goryll, J.R. Stowell, D.R. Allee, Flexible ISFET biosensor using IGZO metal oxide TFTs and an ITO sensing layer, IEEE Sens. J. 14 (2014) 937–938. doi:10.1109/JSEN.2013.2295057.

[101] T.N.T. Nguyen, Y.G. Seol, N. Lee, Organic field-effect transistor with extended indium tin oxide gate structure for selective pH sensing, Org. Electron. 12 (2011) 1815–1821. doi:10.1016/j.orgel.2011.07.009.

[102] R.E. Gyurcsányi, N. Rangisetty, S. Clifton, B.D. Pendley, E. Lindner, Microfabricated ISEs: Critical comparison of inherently conducting polymer and hydrogel based inner contacts, Talanta. 63 (2004) 89–99. doi:10.1016/j.talanta.2003.12.002.

[103] A. Radu, S. Anastasova-Ivanova, B. Paczosa-Bator, M. Danielewski, J. Bobacka, A. Lewenstam, D. Diamond, Diagnostic of functionality of polymer membrane – based ion selective electrodes by impedance spectroscopy, Anal. Methods. 2 (2010) 1490. doi:10.1039/c0ay00249f.

[104] L. Manjakkal, K. Cvejin, J. Kulawik, K. Zaraska, D. Szwagierczak, R.P. Socha, Fabrication of thick film sensitive RuO2-TiO2 and Ag/AgCl/KCl reference electrodes and their application for pH measurements, Sensors Actuators, B Chem. 204 (2014) 57–67. doi:10.1016/j.snb.2014.07.067.

[105] G.L. Goh, S. Agarwala, Y.J. Tan, W.Y. Yeong, A low cost and flexible carbon nanotube pH sensor fabricated using aerosol jet technology for live cell applications, Sensors Actuators, B Chem. 260 (2018) 227–235. doi:10.1016/j.snb.2017.12.127.

[106] G. Gaál, T.A. da Silva, V. Gaál, R.C. Hensel, L.R. Amaral, V. Rodrigues, A. Riul, 3D Printed e-Tongue, Front. Chem. 6 (2018) 1–8. doi:10.3389/fchem.2018.00151.

[107] L.A. Garçon, M. Genua, Y. Hou, A. Buhot, R. Calemczuk, T. Livache, M. Billon, C. Le Narvor, D. Bonnaffé, H. Lortat-Jacob, Y. Hou, A versatile electronic tongue based on surface plasmon resonance imaging and cross-reactive sensor arrays—a mini-review, Sensors. 17 (2017) 1–12. doi:10.3390/s17051046.

[108] H. Jiang, M. Zhang, B. Bhandari, B. Adhikari, Application of electronic tongue for fresh foods quality evaluation: A review, Food Rev. Int. (2018) 1–24. doi:10.1080/87559129.2018.1424184.

[109] C. Krantz-Rülcker, M. Stenberg, F. Winquist, I. Lundström, Electronic tongues for environmental monitoring based on sensor arrays and pattern recognition: A review, Anal. Chim. Acta. 426 (2001) 217–226. doi:10.1016/S0003-2670(00)00873-4.

[110] M. Wesoły, K. Cal, P. Ciosek, W. Wróblewski, Influence of dissolution-modifying excipients in various pharmaceutical formulations on electronic tongue results, Talanta. 162 (2017) 203–209. doi:10.1016/j.talanta.2016.10.018.

[111] L. Shabala, T. Ross, I. Newman, T. Mcmeekin, S. Shabala, Measurements of net fluxes and extracellular changes of H+, Ca2+, K+, and NH4+ in Escherichia coli using ion-selective microelectrodes microelectrodes, J. Microbiol. Methods. 46 (2001) 119–129.

[112] P. Rai, S. Jung, T. Ji, V.K. Varadan, Ion-sensitive field effect transistors for pH and potassium ion concentration sensing: towards detection of myocardial ischemia, Int. Soc. Opt. Photonics. 6931 (2008) 69310I. doi:10.1117/12.776205.

[113] J. Kim, S. Imani, W.R. de Araujo, J. Warchall, G. Valdés-Ramírez, T.R.L.C. Paixão, P.P. Mercier, J. Wang, Wearable salivary uric acid mouthguard biosensor with integrated wireless electronics, Biosens. Bioelectron. 74 (2015) 1061–1068. doi:10.1016/j.bios.2015.07.039.

[114] G. Sanna, M.I. Pilo, P.C. Piu, N. Spano, A. Tapparo, R. Seeber, Microelectrodes for the determination of heavy metal traces in physiological conditions. Hg, Cu and Zn ions in synthetic saliva, Electroanalysis. 14 (2002) 1512–1520. doi:10.1002/1521-4109(200211)14:21<1512::AID-ELAN1512>3.0.CO;2-3.

[115] J.Q. Ang, B.T.T. Nguyen, C.S. Toh, A dual K+-Na+ selective Prussian blue nanotubes sensor, Sensors Actuators, B Chem. 157 (2011) 417–423. doi:10.1016/j.snb.2011.04.076.

[116] G.T. Dang, T. Kawaharamura, M. Furuta, M.W. Allen, Zinc tin oxide metal semiconductor field effect transistors and their improvement under negative bias (illumination) temperature stress, Appl. Phys. Lett. 110 (2017) 073502. doi:10.1063/1.4976196.

[117] J. Kim, K. Wubs, B.-S. Bae, W. Soo Kim, Direct stamping of silver nanoparticles toward residue-free thick electrode, Sci. Technol. Adv. Mater. 13 (2012) 035004. doi:10.1088/1468-6996/13/3/035004.

[118] H.J. Kim, J.W. Hummel, S.J. Birrell, Evaluation of Nitrate and Potassium Ion-Selective Membranes for Soil Macronutrient Sensing, Trans. Asabe. 49 (2006) 597–606. doi:10.13031/2013.20476.

[119] M.A. Abrar, Y. Dong, P.K. Lee, W.S. Kim, Bendable Electro-chemical Lactate Sensor Printed with Silver Nano-particles, Sci. Rep. 6 (2016) 30565. doi:10.1038/srep30565.

[120] J.Y. Gal, Y. Fovet, M. Adib-Yadzi, About a synthetic saliva for in vitro studies, Talanta. 53 (2001) 1103–1115. doi:10.1016/S0039-9140(00)00618-4.

[121] J. Staginus, I.M. Aerts, Z.Y. Chang, G.C.M. Meijer, L.C.P.M. De Smet, E.J.R. Sudhölter, Capacitive response of PDMS-coated IDE platforms directly exposed to aqueous solutions containing volatile organic compounds, Sensors Actuators, B Chem. 184 (2013) 130–142. doi:10.1016/j.snb.2013.04.041.

[122] L. Wang, M. Veselinovic, L. Yang, B.J. Geiss, D.S. Dandy, T. Chen, A sensitive DNA capacitive biosensor using interdigitated electrodes, Biosens. Bioelectron. 87 (2017) 646–653. doi:10.1016/j.bios.2016.09.006.

[123] A. Rivadeneyra, J. Fernández-Salmerón, J. Banqueri, J.A. López-Villanueva, L.F. Capitan-Vallvey, A.J. Palma, A novel electrode structure compared with interdigitated electrodes as capacitive sensor, Sensors Actuators, B Chem. 204 (2014) 552–560. doi:10.1016/j.snb.2014.08.010.

[124] K.N. Mikhelson, Ion-Selective Electrodes, Springer, Berlin, 2013. doi:10.1007/978-3-319-10410-2.

[125] K. Liang, M.D. Weir, M.A. Reynolds, X. Zhou, J. Li, H.H.K. Xu, Poly (amido amine) and nano-calcium phosphate bonding agent to remineralize tooth dentin in cyclic artificial saliva/lactic acid, Mater. Sci. Eng. C. 72 (2017) 7–17. doi:10.1016/j.msec.2016.11.020.

[126] M. Dilea, A. Mazare, D. Ionita, I. Demetrescu, Comparison between corrosion behaviour of implant alloys Ti6Al7Nb and Ti6Al4Zr in artificial saliva, Mater. Corros. 64 (2013) 493–499. doi:10.1002/maco.201206526.

[127] C.J. Collins, D.W.M. Arrigan, Ion-transfer voltammetric determination of the β-blocker propranolol in a physiological matrix at silicon membrane-based liquid|liquid microinterface arrays, Anal. Chem. 81 (2009) 2344–2349. doi:10.1021/ac802644g.

[128] V.W.H. Leung, B.W. Darvell, Artificial salivas for in vitro studies of dental materials, J. Dent. 25 (1997) 475–484. doi:10.1016/S0300-5712(96)00068-1.

[129] S. Imani, A.J. Bandodkar, A.M.V. Mohan, R. Kumar, S. Yu, J. Wang, P.P. Mercier, A wearable chemical–electrophysiological hybrid biosensing system for real-time health and fitness monitoring, Nat. Commun. 7 (2016) 11650. doi:10.1038/ncomms11650.

[130] S. Xu, Y. Zhang, L. Jia, K.E. Mathewson, K. Jang, J. Kim, H. Fu, X. Huang, P. Chava, R. Wang, S. Bhole, L. Wang, Y.J. Na, Y. Guan, M. Flavin, Z. Han, Y. Huang, J.A. Rogers, Soft Microfluidic Assemblies of Sensors, Circuits, and Radios for the Skin, Science. 344 (2014) 70–75.

[131] W.S. Wong, A. Salleo, Flexible Electronics: Materials and Applications, Springer Science & Business Media, 2009. doi:10.1007/978-0-387-74363-9_6.

[132] H.H. Chou, A. Nguyen, A. Chortos, J.W.F. To, C. Lu, J. Mei, T. Kurosawa, W.G. Bae, J.B.H. Tok, Z. Bao, A chameleon-inspired stretchable electronic skin with interactive colour changing controlled by tactile sensing, Nat. Commun. 6 (2015) 1–10. doi:10.1038/ncomms9011.

[133] D. Ponnamma, K.K. Sadasivuni, C. Wan, S. Thomas, M. Al-Ali AlMa'adeed, Flexible and Stretchable Electronic Composites, Springer, Cham, 2015. doi:10.1007/978-3-319-23663-6_3.

[134] D. Muse, E. Macdonald, D. Espalin, E. Aguilera, M. Perez, R.B. Wicker, R. Salas, 3D Printing for the Rapid Prototyping of Structural Electronics, IEEE Access. 2 (2014) 234–242. doi:10.1109/access.2014.2311810.

[135] D. Espalin, D.W. Muse, E. MacDonald, R.B. Wicker, 3D Printing multifunctionality: Structures with electronics, Int. J. Adv. Manuf. Technol. Austin, TX. 72 (2014) 963–978. doi:10.1007/s00170-014-5717-7.

[136] N. Zhou, C. Liu, J.A. Lewis, D. Ham, Gigahertz Electromagnetic Structures via Direct Ink Writing for Radio-Frequency Oscillator and Transmitter Applications, Adv. Mater. 29 (2017). doi:10.1002/adma.201605198.

[137] S.Y. Wu, C. Yang, W. Hsu, L. Lin, 3D-printed microelectronics for integrated circuitry and passive wireless sensors, Microsystems Nanoeng. 1 (2015) 1–9. doi:10.1038/micronano.2015.13.

[138] E. MacDonald, R. Wicker, Multiprocess 3D printing for increasing component functionality, Science. 353 (2016) aaf2093. doi:10.1126/science.aaf2093.

[139] A.J. Lopes, E. MacDonald, R.B. Wicker, Integrating stereolithography and direct print technologies for 3D structural electronics fabrication, Rapid Prototyp. J. 18 (2012) 129–143. doi:10.1108/13552541211212113.

[140] C. Sen Yang, D.S. Shang, N. Liu, E.J. Fuller, S. Agrawal, A.A. Talin, Y.Q. Li, B.G. Shen, Y. Sun, All-Solid-State Synaptic Transistor with Ultralow Conductance for Neuromorphic Computing, Adv. Funct. Mater. 28 (2018) 1–10. doi:10.1002/adfm.201804170.

[141] M. Hu, C.E. Graves, C. Li, Y. Li, N. Ge, E. Montgomery, N. Davila, H. Jiang, R.S. Williams, J.J. Yang, Q. Xia, J.P. Strachan, Memristor-Based Analog Computation and Neural Network Classification with a Dot Product Engine, Adv. Mater. 30 (2018) 1–10. doi:10.1002/adma.201705914.

[142] F. Zhou, Z. Zhou, J. Chen, T.H. Choy, J. Wang, N. Zhang, Z. Lin, S. Yu, J. Kang, H.-S.P. Wong, Y. Chai, Optoelectronic resistive random access memory for neuromorphic vision sensors, Nat. Nanotechnol. 14 (2019) 776–782. doi:10.1038/s41565-019-0501-3.

[143] H. Huang, C. Ge, Q. Zhang, C. Liu, J. Du, J. Li, C. Wang, L. Gu, G. Yang, K. Jin, Electrolyte-Gated Synaptic Transistor with Oxygen Ions, Adv. Funct. Mater. 1902702 (2019) 1–8. doi:10.1002/adfm.201902702.

[144] C. Wang, Z. Yang, S. Wang, P. Wang, C.-Y. Wang, C. Pan, B. Cheng, S.-J. Liang, F. Miao, A Braitenberg Vehicle Based on Memristive Neuromorphic Circuits, Adv. Intell. Syst. 2 (2019) 1900103. doi:10.1002/aisy.201900103.

[145] S. Chen, Z. Lou, D. Chen, G. Shen, An Artificial Flexible Visual Memory System Based on an UV-Motivated Memristor, Adv. Mater. 30 (2018) 1705400.

[146] H. Wang, Q. Zhao, Z. Ni, Q. Li, H. Liu, Y. Yang, L. Wang, Y. Ran, Y. Guo, W. Hu, Y. Liu, A Ferroelectric/Electrochemical Modulated Organic Synapse for Ultraflexible, Artificial Visual-Perception System, Adv. Mater. 30 (2018) 1803961. doi:10.1002/adma.201803961.

[147] Y. Zang, H. Shen, D. Huang, C.-A. Di, D. Zhu, A Dual-Organic-Transistor-Based Tactile-Perception System with Signal-Processing Functionality.pdf, Adv. Mater. 29 (2017) 1606088.

[148] C. Bao, W. Soo Kim, Perspective of Printed Solid-State Ion Sensors toward High Sensitivity and Selectivity, Adv. Eng. Mater. 2000116 (2020) 1–14. doi:10.1002/adem.202000116.

[149] C. Bao, M. Kaur, W.S. Kim, Toward A Highly Selective Artificial Saliva Sensor using Printed Hybrid Field Effect Transistors, Sensors Actuators B Chem. 285 (2019) 186–192. doi:10.1016/j.snb.2019.01.062.

[150] J.T. Yang, C. Ge, J.Y. Du, H.Y. Huang, M. He, C. Wang, H. Bin Lu, G.Z. Yang, K.J. Jin, Artificial synapses emulated by an electrolyte-gated tungsten-oxide transistor, Adv. Mater. 30 (2018) 1–10. doi:10.1002/adma.201801548.

[151] R.A. John, J. Ko, M.R. Kulkarni, N. Tiwari, N.A. Chien, N.G. Ing, W.L. Leong, N. Mathews, Flexible Ionic-Electronic Hybrid Oxide Synaptic TFTs with Programmable Dynamic Plasticity for Brain-Inspired Neuromorphic Computing, Small. 13 (2017) 15–23. doi:10.1002/smll.201701193.

[152] Q.A. Huang, L. Dong, L.F. Wang, LC Passive Wireless Sensors Toward a Wireless Sensing Platform: Status, Prospects, and Challenges, J. Microelectromechanical Syst. 25 (2016) 822–841. doi:10.1109/JMEMS.2016.2602298.

[153] L. Liu, C. Ding, S. Lu, T. Ge, Y. Yan, Y. Mei, K.D.T. Ngo, G.Q. Lu, Design and Additive Manufacturing of Multipermeability Magnetic Cores, IEEE Trans. Ind. Appl. 54 (2018) 3541–3547. doi:10.1109/TIA.2018.2819963.

[154] Y. Yan, J. Moss, K.D.T. Ngo, Y. Mei, G.Q. Lu, Additive Manufacturing of Toroid Inductor for Power Electronics Applications, IEEE Trans. Ind. Appl. 53 (2017) 5709–5714. doi:10.1109/TIA.2017.2729504.

[155] N. Lazarus, S.S. Bedair, G.L. Smith, Creating 3D printed magnetic devices with ferrofluids and liquid metals, Addit. Manuf. 26 (2019) 15–21. doi:10.1016/j.addma.2018.12.012.

[156] R. Igreja, C.J. Dias, Analytical evaluation of the interdigital electrodes capacitance for a multi-layered structure, Sensors Actuators, A Phys. 112 (2004) 291–301. doi:10.1016/j.sna.2004.01.040.

[157] A. Yao, T. Hikihara, Reading and writing operations of memory device in micro-electromechanical resonator, IEICE Electron. Express. 9 (2012) 1230–1236. doi:10.1587/elex.9.1230.

[158] B.J. Kang, C.K. Lee, J.H. Oh, All-inkjet-printed electrical components and circuit fabrication on a plastic substrate, Microelectron. Eng. 97 (2012) 251–254. doi:10.1016/j.mee.2012.03.032.

[159] M.G.B.A. Amsa, A. Amsa, A.M. Aibinu, M.J.E. Salami, A novel hybrid artificial intelligence technique for Colpitts oscillator design, J. Control. Autom. Electr. Syst. 25 (2014) 10–21. doi:10.1007/s40313-013-0084-4.

[160] M.K. Kazimierczuk, D. Murthy-Bellur, Synthesis of LC sinusoidal oscillators, Int. J. Electr. Eng. Educ. 49 (2012) 26–41. doi:10.7227/IJEEE.49.1.3.

[161] J. Zhu, Y. Yang, R. Jia, Z. Liang, W. Zhu, Z.U. Rehman, L. Bao, X. Zhang, Y. Cai, L. Song, R. Huang, Ion Gated Synaptic Transistors Based on 2D van der Waals Crystals with Tunable Diffusive Dynamics, Adv. Mater. 30 (2018) 1–11. doi:10.1002/adma.201800195.

[162] H. Han, H. Yu, H. Wei, J. Gong, W. Xu, Recent Progress in Three-Terminal Artificial Synapses: From Device to System, Small. 15 (2019) 1–17. doi:10.1002/smll.201900695.

[163] J. Shi, S.D. Ha, Y. Zhou, F. Schoofs, S. Ramanathan, A correlated nickelate synaptic transistor, Nat. Commun. 4 (2013) 1–9. doi:10.1038/ncomms3676.

[164] F. Yu, L.Q. Zhu, H. Xiao, W.T. Gao, Y.B. Guo., Restickable Oxide Neuromorphic Transistors with Spike-Timing-Dependent Plasticity and Pavlovian Associative Learning Activities, Adv. Funct. Mater. 28 (2018) 1804025.

[165] J.R. Brown, Chemical Soil Test Procedures for the North Central Region, 2011.

[166] X. Li, Y. Zhang, W. Wang, M.R. Khan, R. Cong, Establishing grading indices of available soil potassium on paddy soils in Hubei province, China, Sci. Rep. 8 (2018) 1–8. doi:10.1038/s41598-018-33802-3.

[167] C. Bao, S.K. Seol, W.S. Kim, A 3D Integrated Neuromorphic Chemical Sensing System, Sensors Actuators B Chem. 332 (2021) 129527. doi:10.1016/j.snb.2021.129527.

[168] S. Kim, D.G. Roe, Y.Y. Choi, H. Woo, J. Park, J.I. Lee, Y. Choi, S.B. Jo, M.S. Kang, Y.J. Song, S. Jeong, J.H. Cho, Artificial stimulus-response system capable of conscious response, Sci. Adv. 7 (2021) 1–9. doi:10.1126/SCIADV.ABE3996.

[169] K. He, Y. Liu, M. Wang, G. Chen, Y. Jiang, J. Yu, C. Wan, D. Qi, M. Xiao, W.R. Leow, H. Yang, M. Antonietti, X. Chen, An Artificial Somatic Reflex Arc, Adv. Mater. 32 (2020) 1905399.

[170] A. Chortos, J. Liu, Z. Bao, Pursuing prosthetic electronic skin, Nat. Mater. 15 (2016) 937–950. doi:10.1038/nmat4671.

[171] G. Sen Gupta, P. Barlow, S. David, Review of sensors and sensor integration for the control of a humanoid robot, Conf. Rec. - IEEE Instrum. Meas. Technol. Conf. (2011) 1–5. doi:10.1109/IMTC.2011.5944336.

[172] A.H. Abdul Razak, A. Zayegh, R.K. Begg, Y. Wahab, Foot plantar pressure measurement system: A review, Sensors (Switzerland). 12 (2012) 9884–9912. doi:10.3390/s120709884.

[173] E.I.G. Velásquez, V. Gómez, L. Paredes-Madrid, H.A. Colorado, Error compensation in force sensing resistors, Sens. Bio-Sensing Res. 26 (2019) 100300. doi:10.1016/j.sbsr.2019.100300.

[174] S. Li, H. Fang, S. Sadeghi, P. Bhovad, K.W. Wang, Architected Origami Materials: How Folding Creates Sophisticated Mechanical Properties, Adv. Mater. 31 (2019) 1805282. doi:10.1002/adma.201805282.

[175] Z. Li, N. Kidambi, L. Wang, K.W. Wang, Uncovering rotational multifunctionalities of coupled Kresling modular structures, Extrem. Mech. Lett. 39 (2020) 100795. doi:10.1016/j.eml.2020.100795.

[176] Z. Zhai, Y. Wang, H. Jiang, Origami-inspired, on-demand deployable and collapsible mechanical metamaterials with tunable stiffness, Proc. Natl. Acad. Sci. U. S. A. 115 (2018) 2032–2037. doi:10.1073/pnas.1720171115.

[177] L.S. Novelino, Q. Ze, S. Wu, G.H. Paulino, R. Zhao, Untethered control of functional origami microrobots with distributed actuation, Proc. Natl. Acad. Sci. U. S. A. 117 (2020) 24096–24101. doi:10.1073/pnas.2013292117.

[178] M. Kaur, T.H. Kim, W.S. Kim, New Frontiers in 3D Structural Sensing Robots, Adv. Mater. 33 (2021) 2170148. doi:10.1002/adma.202002534.

[179] A.D. Valentine, T.A. Busbee, J.W. Boley, J.R. Raney, A. Chortos, A. Kotikian, J.D. Berrigan, M.F. Durstock, J.A. Lewis, Hybrid 3D Printing of Soft Electronics, Adv. Mater. 1703817 (2017) 1–8. doi:10.1002/adma.201703817.

[180] J.A. Lewis, Direct ink writing of 3D functional materials, Adv. Funct. Mater. 16 (2006) 2193–2204. doi:10.1002/adfm.200600434.

[181] Y. Zhang, G. Shi, J. Qin, S.E. Lowe, S. Zhang, H. Zhao, Y.L. Zhong, Recent Progress of Direct Ink Writing of Electronic Components for Advanced Wearable Devices, ACS Appl. Electron. Mater. 1 (2019) 1718–1734. doi:10.1021/acsaelm.9b00428.

[182] Y. Jo, H.J. Park, Y. Bin Kim, S.S. Lee, S.Y. Lee, S.K. Kim, Y. Choi, S. Jeong, Form-Factor Free 3D Copper Circuits by Surface-Conformal Direct Printing and Laser Writing, Adv. Funct. Mater. 30 (2020) 2004659. doi:10.1002/adfm.202004659.

[183] L. Xu, T.C. Shyu, N.A. Kotov, Origami and Kirigami Nanocomposites, ACS Nano. 11 (2017) 7587–7599. doi:10.1021/acsnano.7b03287.

[184] T.H. Kim, J. Vanloo, W.S. Kim, 3D Origami Sensing Robots for Cooperative Healthcare Monitoring, Adv. Mater. Technol. 6 (2021) 2000938. doi:10.1002/admt.202000938.

[185] J.R. Garcia, D. O'Suilleabhain, H. Kaur, J.N. Coleman, A Simple Model Relating Gauge Factor to Filler Loading in Nanocomposite Strain Sensors, ACS Appl. Nano Mater. 4 (2021) 2876–2886. doi:10.1021/acsanm.1c00040.

Appendix.

Supplementary Figures

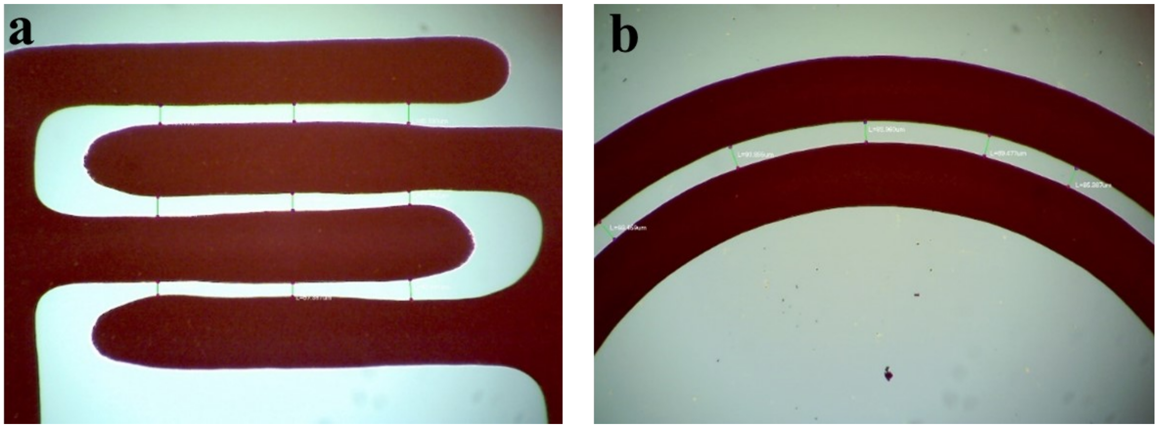

Figure A1. Comparison of two electrode designs. (a) It shows IDE structure. (b) it shows the serpentine shaped electrodes. Although the channel length is nearly similar to 72 µm for IDE and 89 µm for serpentine channel structure, respectively, the uniformity of channel length is different. For IDE, the channel length varies from 57 µm to 85 µm. However, the channel length of serpentine design is between 84 µm and 94 µm. This shows the advantage of serpentine design over IDE in order to obtain a uniform FET channel by the 3D printing method.

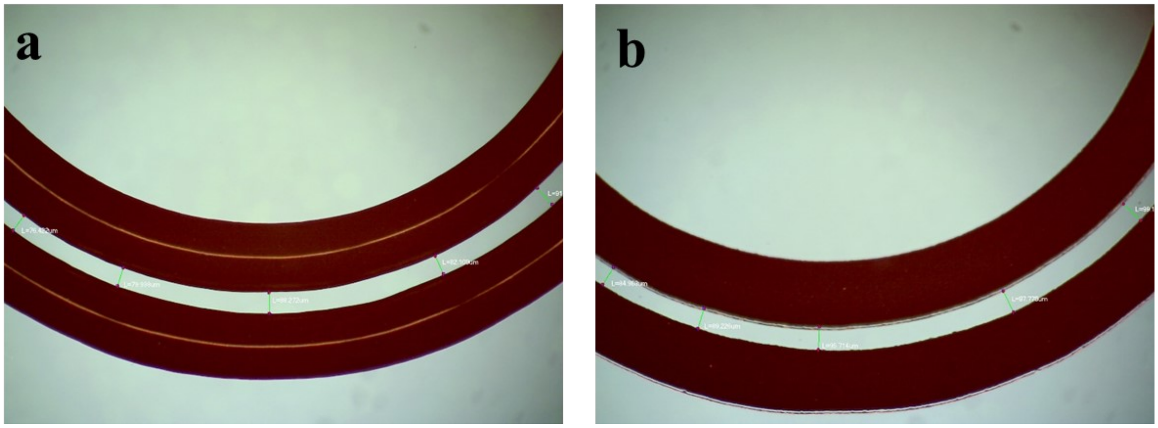

Figure A2. Change of channel length after thermal curing. It shows channel length variation before and after curing. Before baking, the average channel length is 84 µm. However, the channel length enlarged to 93 µm, which shows an around 10 µm increment because of the electrode's volume shrinkage by curing procedure.

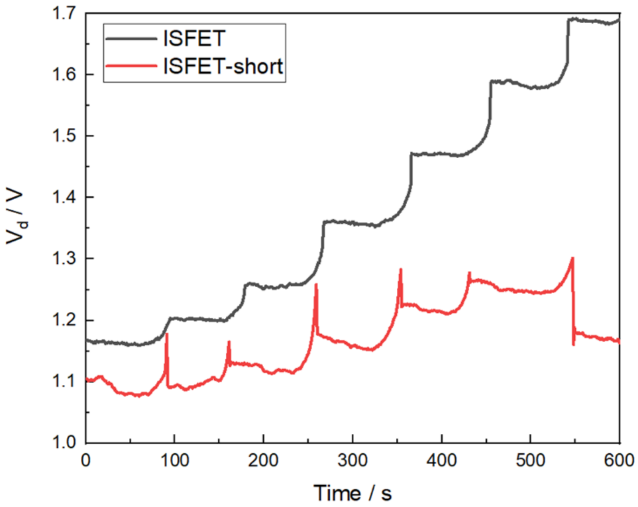

Figure A3. Comparison of ISFETs and the short circuit of ISFETs. It shows the performance of short circuit ISFETs by connecting the working electrode and the reference electrode directly. The voltage of short circuit ISFETs merely increases with the ion concentration compared with the ISFETs.

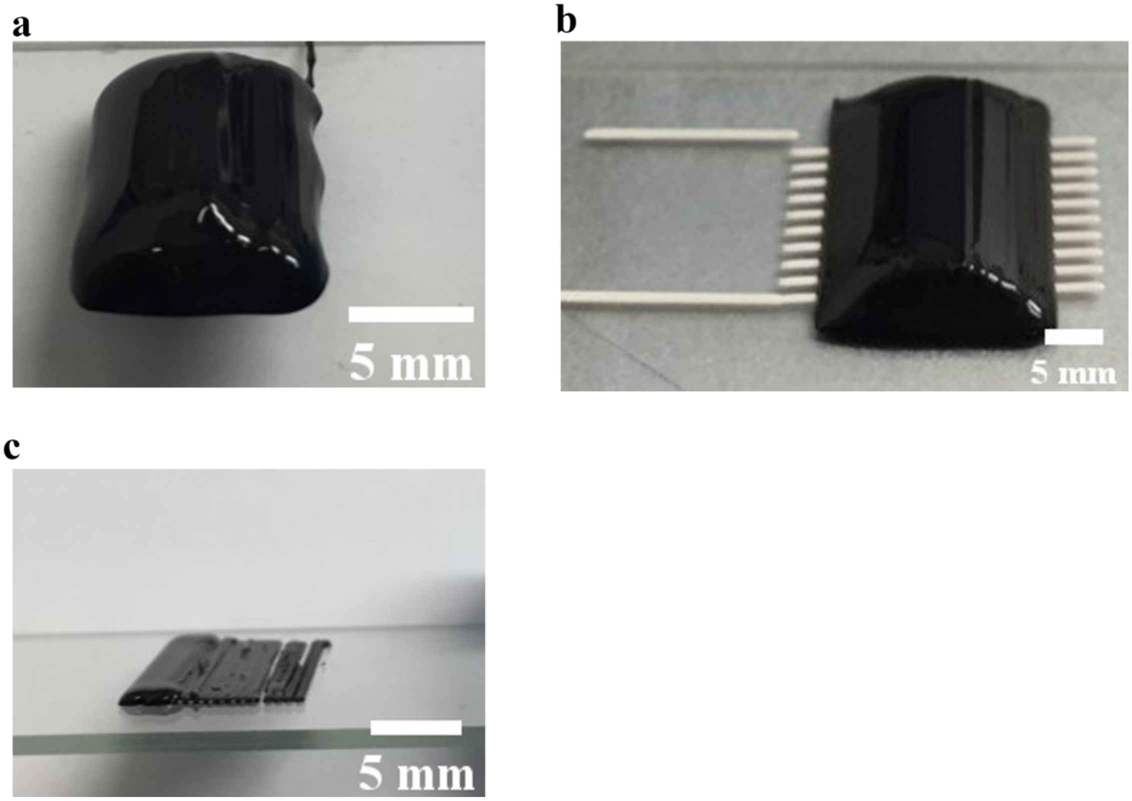

Figure A4. Printability study of Mn-ferrite with different concentrations. (a) 80 wt%, (b) 82.5 wt%, and (c) 85 wt%, respectively.

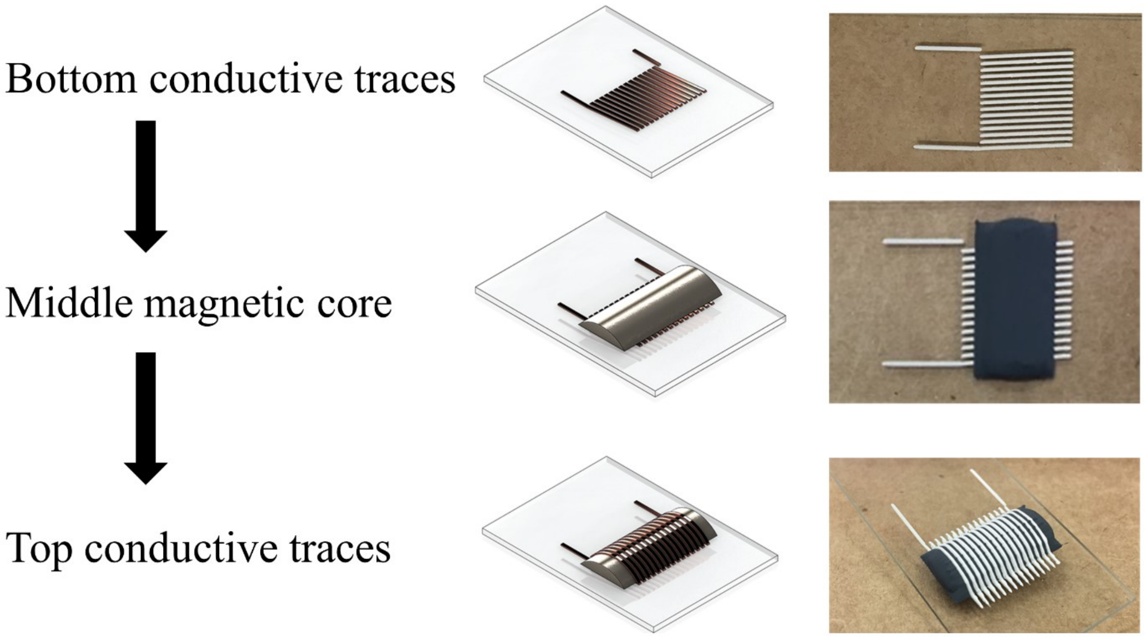

Figure A5. The fabricated procedure for 3D shaped inductors.

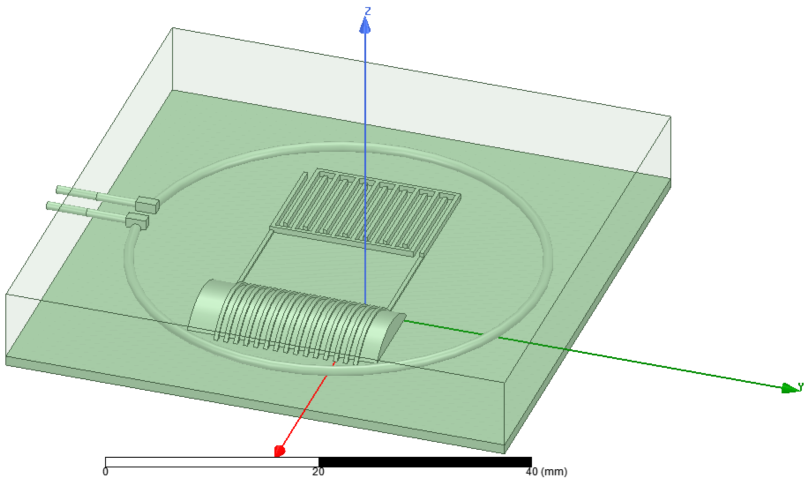

Figure A6. The computational model established in Maxwell-ANSYS for the simulation of the resonant frequency.

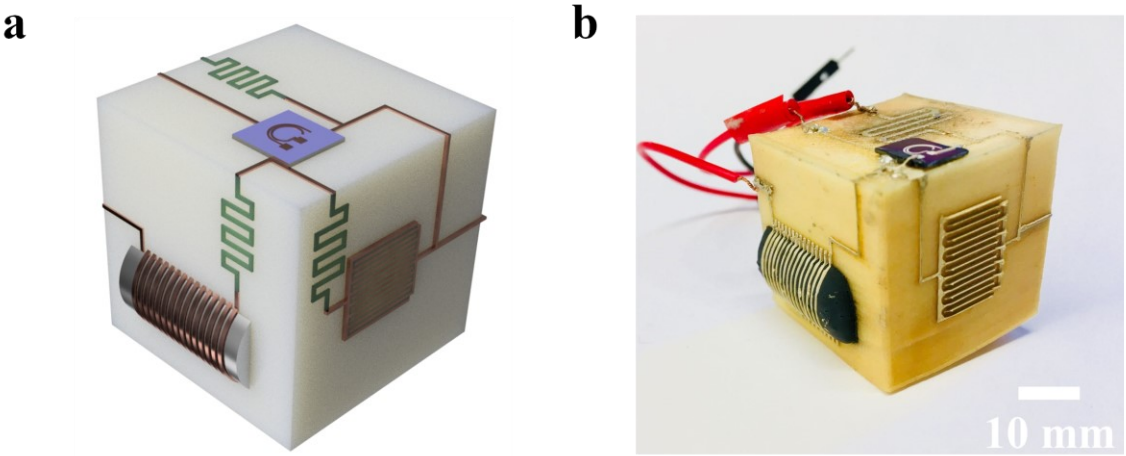

Figure A7. **3D Electrical oscillators. (a) Design of the 3D electrical oscillator. (b) Sample image of the fabricated oscillator.**

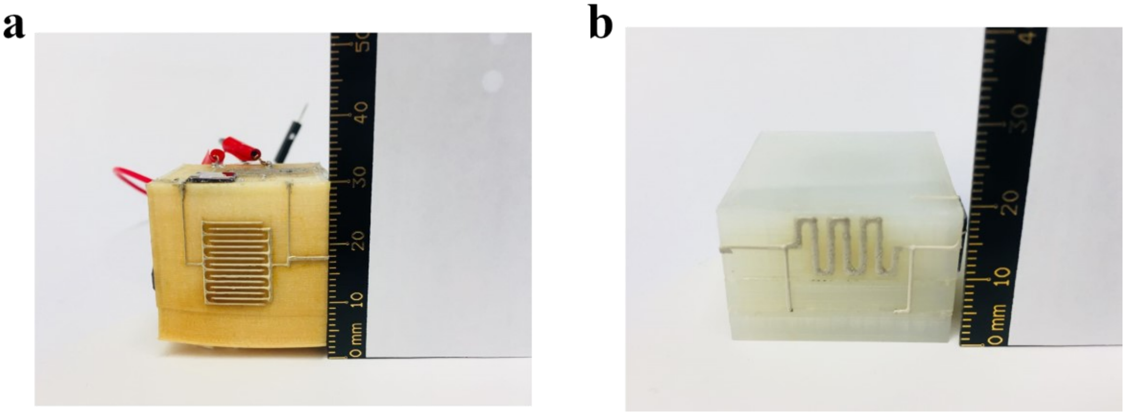

Figure A8. **Comparison of volume difference. (a) Facial oscillator, and (b) embedded oscillator, respectively.**

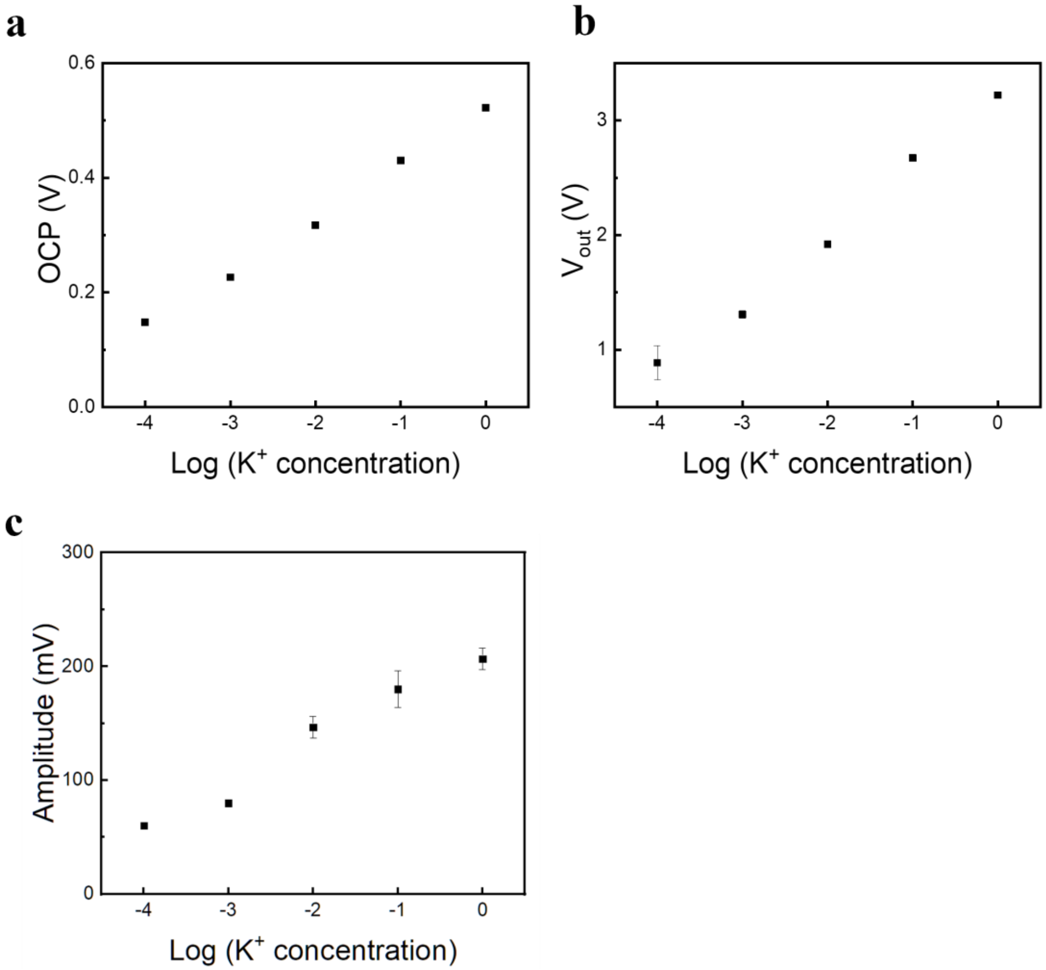

Figure A9. Characterization of ISE and the integrated ISE with the electrical oscillator. (a) Relation between OCP and K$^+$ ion concentration. (b) Relation between oscillator output and K$^+$ ion concentration. (c) Relation between amplitude and K$^+$ ion concentration.

Figure A10. Resistance change of the potentiometric pressure sensor at the compression. Photos present that the resistance is gradually reduced once the sensor is compressed.

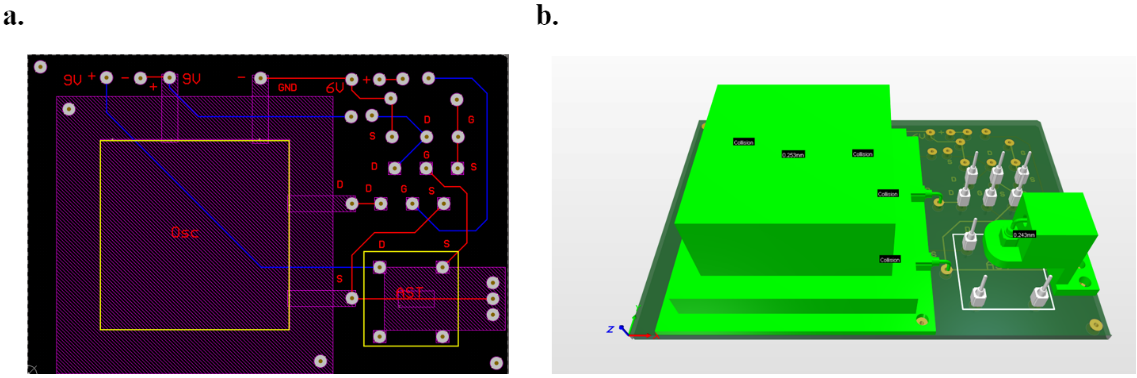

Figure A11. Design of the integrated neuromorphic system. (a) PCB layout for the neuromorphic system. (b) 3D structure of the mounted neuromorphic system.

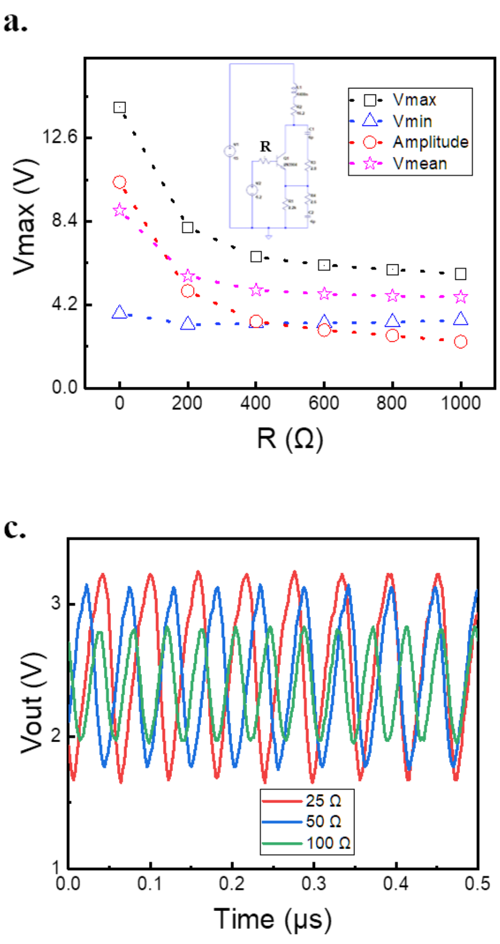

Figure A12. Simulation and experiments for integration of pressure sensor and oscillator. (a), (c) Simulation and experimental results for the relation between the output signal and resistance when tactile sensor connected at the gate electrode of the transistor. (b), (d) Simulation and experimental results for the relation between the output signal and resistance when tactile sensor connected at source electrode of the transistor.

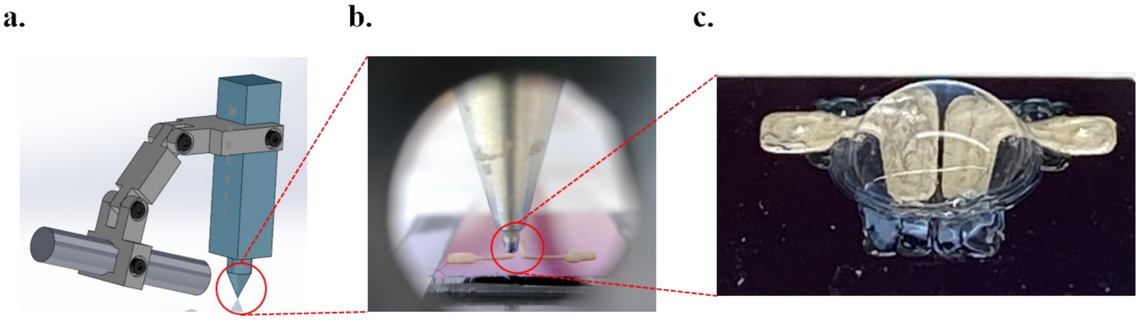

Figure A13. **The facilitation from a digital camera magnifier for the fabrication of synaptic transistors. (a) Set up for the digital camera magnifier. (b) Alignment of the nozzle. (c) fabricated synaptic transistor for constraining liquid electrolyte.**